UC Merced
UC Merced Electronic Theses and Dissertations

Title
Non-diffusive Heat Conduction in Nano-/Micro-scale Structures

Permalink
https://escholarship.org/uc/item/36g4v7pk

Author
Wang, Dadong

Publication Date
2015

Peer reviewed|Thesis/dissertation

eScholarship.org Powered by the California Digital Library
University of California

UNIVERSITY OF CALIFORNIA, MERCED

Non-diffusive Heat Conduction in Nano-/Micro-scale Structures

By

Dadong Wang

A dissertation submitted in partial satisfaction of the requirements
for the degree of Doctor of Philosophy

In

Biological Engineering and Small-scale Technology
School of Engineering

Committee in charge:

Professor Yanbao Ma, Advisor
Professor Ashlie Martini
Professor Lilian Davila
Professor Min Hwan Lee

2015

© Dadong Wang, 2015
All rights reserved

The Dissertation of Dadong Wang is approved:

_____

Yanbao Ma, Chair Date

_____

Ashlie Martini Date

_____

Lilian Davila Date

_____

Min Hwan Lee Date

University of California, Merced
2015

Abstract

Rapid progress has been made in the manufacture of microelectronic and thermoelectric devices. With continuous decrease in the size of devices and structures, the manipulation and control of phonon-mediated heat transfer on the nano-/micro-scale is becoming a bottleneck for the development of many nano-/micro-technologies. To advance these technologies, it is necessary to understand the fundamental mechanisms of thermal transport at nano-/micro-scale. The new feature of heat transfer in nano-/micro-scale systems is non-diffusive thermal transport which cannot be described by Fourier's law. However, current nano-thermometry of non-diffusive heat transfer still focuses on studying the effective thermal conductivity within the framework of Fourier's law due to a lack of a well-accepted non-diffusive model. The molecular dynamics (MD) and full spectral Boltzmann transport equation (BTE) are unpractical to be applied for experimental data analysis due to their prohibited computational cost. For Gray BTE and other macroscopic models such as Cattaneo-Vernotte (CV) equation, Guyer-Krumhansl (GK) equation, Dual-phase-lag (DPL) equation and et al., they cannot capture the non-diffusive heat transport accurately.

In this thesis we will develop a high-fidelity model that can accurately describe phonon transport at nano-/micro-scale regime and can replace Fourier's law for experimental data analysis. The new model named enhanced gray (EG) model is derived from the phonon Boltzmann transport equation (BTE) by considering the second-order terms in Taylor expansion of phonon density distribution. In the proposed enhanced gray BTE (EG-BTE), two parameters associated with inherent material properties, i.e., the ballistic mean free time and the diffusive relaxation time, are used to characterize the non-diffusive nature of heat conduction. Theoretical solutions of EG-BTE

based on Fourier transform are presented in three-dimensional domain for transient thermal grating (TTG) experiments and time domain thermo-reflectance (TDTR) experiments. The reconstructed thermal decays by EG-BTE are in excellent match with the measured signal traces in TTG and TDTR experiments, which demonstrates the validity of our new model. For problems where analytical solutions are not available, an implicit lattice Boltzmann method (LBM) is developed to solve the EG-BTE, which is unconditionally stable and computationally efficient. As an illustrative application, the phonon transport in cryogenic crystals is studied by implicit LBM simulation based on EG-BTE. The heat-pulse experiment conducted in cryogenic crystals observed the only direct evidence of ballistic heat transport. The successive interpretation of this benchmark case by EG-BTE provides a better understanding of the physical nature of non-diffusive heat transfer.

The proposed EG-BTE opens a new avenue to study the unique features of non-diffusive heat transfer. The current interpretations of TDTR experiments is limited by Fourier's law. For example, the measurements of effective thermal conductivity within the framework of Fourier's law will provide little insight for non-diffusive heat transfer. By deriving the analytical solution of EG-BTE for TDTR experiments, a new theoretical framework based on EG-BTE that can remove the limit of Fourier law for experimental data analysis is developed and proved. Some unique material thermal properties of non-diffusive heat conduction can be characterized, such as the ballistic mean free time and the diffusive relaxation time. But further development and improvement of the theoretical tool are required to understand other features of non-diffusive heat transfer, such as the interfacial thermal conductance, which can be our future work.

To the Beauty of Nature

Acknowledgments

The beauty of nature is full of unknowns and surprise. To understand nature and uncover the mystery is always a wonderful and difficult expedition for researchers. Fortunately, I am not alone in this journey. In these years, many people have guided, supported, and stimulated me to keep going and achieve success. Here I would like to gratefully acknowledge their help.

I would definitely first thank my advisor, Professor Yanbao Ma. In these more than five years, Dr. Ma routinely goes beyond what is expected as an advisor, from supervising students to form good habits, to teaching students how to give an excellent presentation, to giving insightful suggestions for my drafts of papers. I am particularly grateful to Yanbao for supporting me to develop as an independent researcher by giving me almost complete freedom to choose research topics especially in the last year. I will always be thankful for the patience, kindness, and concern from Dr. Ma.

Second, I would like to thank my thesis committee members, Professor Ashlie Martini, Professor Lilian Davila, and Professor Min Hwan Lee. They gave me valuable comments on my qualify exam and constructive advice on this thesis.

I am also thankful for several former and current members in W&E Lab group. Dr. Laibing Jia, Dr. Ramu Ashok, and Dr. Hao Peng offered me useful suggestions on my research. I am very happy to work with my current labmates: Chuanjin Lan, Zhengxian Qu, Hanfei Guo, and et al. My labmates are a great resource and I greatly benefitted from the communication and collaboration with them. In particular, I have really enjoyed discussing the research work with Zhengxian, and the quality of my work is enhanced because of my interaction with him.

I am really lucky to have had a great group of friends during my life at UC Merced. Their presence made my time here much more joyful and enjoyable. Dr. Dan Hu, my senior fellow in USTC and UC Merced, provided me great help in my life, research and career paths from the beginning to the end of my journey here. I would also like to thank other good friends Chengjie Qin, Tao Ren, Hongyu Gao, Zhijiang Ye, Wen Pan, Chun Tang, Cheng Yu, Ye Zhu, Jia Jia, Siyu Wu, Wei Liang, Youhong Zeng, Shuo Liu, Wenjing Hu, and et al. I will surely miss them as we all will leave or have already left Merced.

I would like to express a special debt to my master of Shifu Yang Zhou and lifetime friend Xu Han. My Shifu, Yang Zhou, encouraged me to enter one of the top universities in China and changed the trajectory of my life. There were many times during my PhD when I faced hardship, felt frustrated, and was distracted. It was them who encouraged and inspired me to keep moving forward and never compromise. Their enterprise and strong motivation ignited my courage to follow my heart and intuition.

Finally, I want to afford my whole heart and deepest gratitude to my parents for their unconditional love, trust, and sacrifice. The care, kindness, and education from my family are really enabled me to be a responsible man. Without the continuous support from them, I could not achieve this goal.

Contents

List of Figures

Chapter 1

Introduction

1.1 Background

In the past several decades, the drive for faster computing and progressive device miniaturization has resulted in the characteristic dimensions of electronic devices shrinking from the microscale to the nanoscale. Packing more and more transistors onto a single chip and doing high speed computing increases power consumption and generates large quantity of heat. The localized nature of the heat generation process can result in intense hot spots. The inability to remove heat efficiently is currently one of the major obstacles toward further miniaturization and advancement of electronic and micro-electro-mechanical system (MEMS) devices. Overheating can drastically reduce the performance and reliability of these devices and cause failures in applications with life-threatening consequences [1-5].

In order to figure out better heat removal strategies and designs, it is necessary to understand the fundamental mechanisms of thermal transport in semiconductor nanostructures. In fact, there has been an increasing interest in modeling thermal transport in nano-/micro scale semiconductor devices [6-10]. Nano-/micro-scale heat transfer is energy transports over length scales comparable to the heat carrier wavelengths and mean free paths (MFPs). Transport at these

scales deviates significantly from the predictions of diffusion theory which is valid in bulk materials [11, 12].

1.2 Microscopic picture of heat carrier

There are three modes of heat transfer: conduction, convection, and radiation. Heat conduction is the transfer of internal energy by microscopic diffusion and collisions of particles or quasi-particles within the substance. The heat carriers of conduction include electrons and phonons. The individual contributions of these carriers can vary widely depending on the materials. In metals, the main carrier is electrons. However, in insulator and semiconductor materials, phonons are the main carrier.

Heat conduction in crystalline dielectric solids occurs by lattice vibrations. The lattice vibrations result in traveling waves of various frequencies and speeds ultimately causing energy to propagate within the solid. From a quantum mechanical perspective, each lattice vibration mode is quantized and can be treated as a quantum oscillator [13, 14]. This discrete energy packet of lattice vibration mode is referred as "phonon", analogous to the term "photon" as a quantum unit of the electromagnetic radiation waves.

According to quantum theory, the energy of a harmonic oscillator is given by

$$E_n = (n+1/2)\hbar\omega \tag{1.1}$$

where $\hbar = h/2\pi$, h is Planck constant, ω is the characteristic frequency of the quantum oscillator, and $n = 1/[\exp(\hbar\omega/k_B T)-1]$ is the average phonon occupation number, which can be derived using Bose-Einstein statistics.

We should emphasize that although photons and phonons can be thought of as particles with energy, these particles are fundamentally different from electrons [15]. Unlike electrons, phonons and photons at rest do not have mass; and are fictitious particles since they are the quantization of the normal mode of a field. Electrons obey the Pauli Exclusion Principle, which says that each quantum state can have only one electron at most. Photons and phonons are not limited by the Pauli Exclusion Principle. Each quantum state, which corresponds to one set of wave vectors, can have many phonons and photons. Due to the differences in their statistical behaviour, electrons are called fermions, while phonons and photons are called bosons.

In one dimensional lattice, the phonon waves are longitudinal waves. In a three dimensional crystal, the atoms can vibrate in three dimensions. As a result, we will have three vibrational branches for the acoustic modes: one longitudinal and two transverse branches. Furthermore, if there are m atoms per lattice point, then 3(m-1) optical branches exist, of which 2(m-1) are transverse optical phonons and the (m-1) are longitudinal optical phonons. In a transverse wave, the atomic displacement direction is perpendicular to the wave propagation direction. The two transverse branches will coincide with each other if the two vibrational directions are symmetric. Phonon dispersions along different crystallographic directions are different. Figure 1.1 shows the phonon dispersion for Si, which has a face-centered cubic (fcc) structure but two atoms as the basis. Therefore, Si has three acoustic branches and three optical branches in each direction. In some high symmetric directions, such as the [100] direction, the two transverse phonon branches collapse into one.

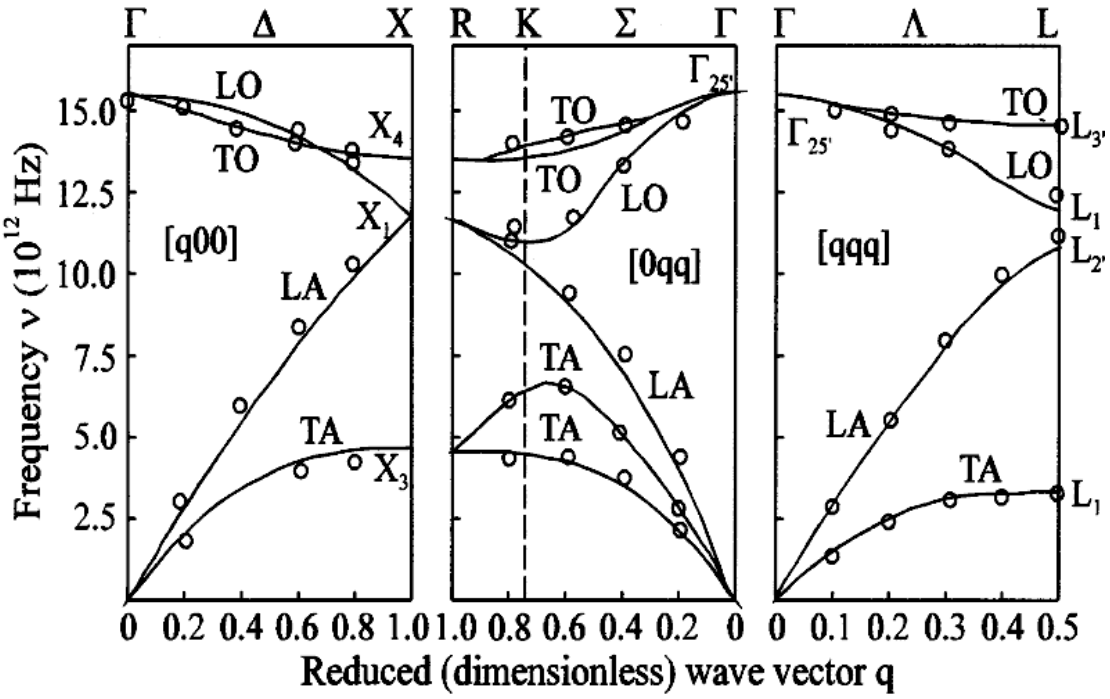

Figure 1.1. Silicon dispersion curves for acoustic and optical phonons [16].

1.3 Challenges of Nano-/Micro-scale Simulation

Different physical laws may be required to describe the problem at different length and/or time scales. At the macroscale level, the Fourier law and energy conservation equation are the governing equations to accurately predict the temperature and heat flux. At the nano-/micro-scale level, the well-known Boltzmann transport equation gives the description of heat conduction in terms of the phonon distribution function, which is based on the statistic theory. At the atomic-level, Molecular Dynamics can be applied to predict the heat transport, which integrates the Newton's law with a suitable potential function. These three modeling tools are discussed in detail in this section.

1.3.1 Limitation of the Fourier's Law

Heat conduction processes are usually modeled on the basis of the Fourier's Law that relates the heat flux to the local temperature gradient

$$\boldsymbol{q} = -\kappa \nabla T \tag{1.2}$$

The thermal conductivity, κ, of a substance indicates the ease with which thermal energy can be transferred through it by conduction. This law applies to most engineering situations and is the foundation of classical heat transfer analysis.

By combining the Fourier law and the energy equation, and assuming no mass transfer and constant properties, one obtains the partial differential equation

$$C_v \frac{\partial T}{\partial t} = \kappa \nabla^2 T \tag{1.3}$$

where C_v the volumetric specific heat, and t the time. The Fourier law is the classical heat conduction law which works well at macroscale. However, past studies have shown that Fourier law is inadequate for the prediction of heat conduction in nano-/micro-scale. The validity and applicability is based on these assumptions [17]:

a. The system behaves classically and can be modeled as a continuum.

b. The energy carrier transport is diffuse. Cases where interface and/or boundary effects dominate correspond to ballistic transport cannot be considered in this formulation.

c. The material properties are known.

For a characteristic length L, a dimensionless parameter Knudsen number (Kn = Λ/L) is frequently used to describe the regime of phonon transport, where Λ is the phonon mean free path (MFP). When the phonon MFP is larger than L (Kn > 1), the phonon transport with little scattering is termed as "ballistic". When the phonon MFP is much less than L (Kn << 1), the transport of

phonons is described as “diffusion” with sufficient number of scattering. In the regime between this two is called “quasi-ballistic”.

The Fourier law is only valid for diffusive regime (Kn << 1). At small length scales (Kn ~ 1) the suitability of the first two criteria may be questionable, and experimental property data may not always be available. One example is Fourier’s Law fails to predict the thermal conductivity of nanostructures [18, 19]. Because the boundary/interface imposes additional resistance to the heat flow compared to bulk materials, the effective thermal conductivity of nanostructures is smaller than those of their corresponding bulk materials.

In addition, if we deal with transport process shorter than the phonon relaxation time, the classical Fourier diffusion law will no longer hold true, since the diffusion process is established by considering the multiple collisions of the heat carriers such that their motion is almost random.

1.3.2 Limitation of Molecular Dynamics simulation

Molecular Dynamics (MD) is a numerical simulation of physical movements of atoms and molecules. In the most common version, the trajectories of molecules and atoms are determined by numerically solving the Newton's equations of motion for a system of interacting particles. The fidelity of MD depends on the accuracy of the interatomic potentials which are usually determined by either first principles calculations or obtained by curve-fitting parameters of empirical potential function based on comparison between calculations and experiments [18].

Because the formalism of the MD approach does not require any a priori understanding of heat transport, it is ideal for investigating the fundamental heat-transfer mechanisms. However, MD does have the significant limitation of being entirely classical, with each vibrational mode equally excited; thus it is only rigorously applicable to solids above the Debye temperature. In

addition, since electrons are not included in an atomistic model, it is not possible to simulate electrical conductors or the electron–phonon interactions exist in many semiconductors. Moreover, the force calculation for many-body potentials is so computationally expensive that it limits the application of MD approach to microscale structures [7].

1.3.3 Complexity of Boltzmann transport equation

The Boltzmann transport equation (BTE), devised by Ludwig Boltzmann, describes the behavior of particles by a statistical distribution. It is one of the most important equations of non-equilibrium statistical mechanics, the area of statistical mechanics that deals with systems far from thermodynamic equilibrium.

The Boltzmann equation is an equation for the temporal evolution of the distribution function (properly a density) function $f(t, r, p)$ in one-particle phase space, where **r** and **p** are position and momentum, respectively. The distribution is defined so that $f(t, r, p)drdp$ is the number of molecules which, at time t, have positions lying within a volume element d^3r around **r** and momentum lying within a momentum-space element d^3p around **p**. Consider those particles described by *f* experiencing an external force $\boldsymbol{F}$, then *f* must satisfy [20]

$$\frac{\partial f}{\partial t} + \boldsymbol{v} \cdot \nabla_r f + \frac{\boldsymbol{F}}{m} \cdot \nabla_v f = \left(\frac{\partial f}{\partial t}\right)_{scatt} \tag{1.4}$$

$\boldsymbol{F}$ is the force field acting on the particles in the system, and m is the mass of the particles. The term on the right hand side is scatterings/collisions between particles. The Boltzmann equation gives the distribution function at **r** and **p** in the phase space. Typically, we are interested in the quantities averaged over p, for example, the average velocity and energy. If the solution of the

Boltzmann equation is known, we can calculate the volume average of any microscopic property X of the particle from

$$< X(r) >= \frac{1}{V}\int X(r,p) f d^3 p \tag{1.5}$$

The challenge of the Boltzmann equation is from the complexity of the scattering term. The Fermi golden rule gives the transition rate from one set of quantum states of the two particles into another set due to the scattering. The scattering term in the Boltzmann equation is the net gain of particles in one quantum state. This net gain consists of two components: one is the increase in the number of particles due to scattering from other quantum stats into the quantum state under consideration ('in-scattering'); the other is the decrease of the number of particles due to scattering from the current quantum state to other quantum states ('out-scattering'). We take the two-particle scattering process as an example. This initial wave vector of one particle is **k** and it collides with another particle with a wave vector $\mathbf{k}_1$. The corresponding distribution functions for the two particles are $f(t,r,k)$ and $f(t,r_1,k_1)$. After scattering, the distribution functions are $f(t,r',k')$ and $f(t,r_1',k_1')$, respectively. The scattering term for the two particles at state k can be expressed as

$$\left(\frac{\partial f}{\partial t}\right)_c = \sum_{k',k_1,k_1'} -f(t,r,k')f(t,r,k_1')W(k,k') + f(t,r,k)f(t,r,k_1)W(k',k) \tag{1.6}$$

The reciprocity relation $W(k,k') = W(k',k)$ arising from the principle of detailed balance is valid. Now the Boltzmann transport equation is a complicated integral-differential equation as follows [20]

$$\frac{\partial f}{\partial t} + \boldsymbol{v}\cdot\nabla_r f + \frac{\boldsymbol{F}}{\hbar}\cdot\nabla_k f = \frac{V^3}{(2\pi)^9}\int W[f(k')f(k_1') - f(k)f(k_1)]d^3k d^3k' d^3k_1' \tag{1.7}$$

The problem of existence and uniqueness of solutions to the Boltzmann equation is still not fully resolved. In fact, the BTE in its most general form, is difficult to solve analytically or even numerically using deterministic approaches. Past research has enabled its solution by neglecting important effects such as dispersion and interactions between the longitudinal and transverse polarizations of phonon propagation. In next section, we summarize the state of art of simplified BTE models.

1.4 The State of Art of Simplified BTE Models

The BTE is valid at nanoscale if the length scale is larger than phonon wavelength so that the phonons can be treated as particles. Furthermore, macroscopic constitutive equations such as Fourier's law, Fick's law can be derived from the BTE in the macroscale limit. This section summarizes the state of art of different models based on BTE for heat conduction.

1.4.1 Gray model and Cattaneo equation

Since the BTE in the most general form is difficult to solve using deterministic approaches. The most common approximation used to simplify the scattering integral is the relaxation time approximation

$$\left(\frac{\partial f}{\partial t}\right)_c = -\frac{f - f_0}{\tau} \tag{1.8}$$

where τ is the relaxation time, and f_0 represents the equilibrium distribution of the carriers, i.e., the Bose-Einstein distributions. The relaxation time approximation is also called the BGK approximation in gas dynamics in honour of the joint work of Bhatnagar, Gross, and Krook [21]. This approximation essentially linearizes the scattering term. In reality, the Boltzmann equation

containing anharmonic interactions is nonlinear. We can understand the meaning of τ easily by neglecting the spatial non-uniformity of the distribution function. The relaxation time is a measure of how long it takes for nonequilibrium system to relax back to an equilibrium distribution $f - f_0 = C\exp(-t/\tau)$.

Gray model

The scattering may be caused by the coexistence of different processes and a relaxation time can be defined for each process. The total relaxation time can be calculated from individual relaxation time according to the Matthiessen rule $\frac{1}{\tau} = \sum_j \frac{1}{\tau_j}$. The Matthiessen rule assumes that the scattering mechanisms are independent of each other. Under the relaxation time approximation, the Boltzmann equation becomes

$$\frac{\partial f}{\partial t} + \boldsymbol{v} \cdot \nabla_r f = -\frac{f - f_0}{\tau} \tag{1.9}$$

If τ is the average relaxation time and independent of frequency, Eq. (1.9) is called gray model.

Cattaneo equation

In Fourier's law, the speed of propagation of heat is infinite. Such a property was considered by many authors to be paradoxical. In order to remove the paradox, in 1948 Cattaneo proposed his celebrated evolution equation for the heat flux

$$\tau \frac{\partial \boldsymbol{q}}{\partial t} + \boldsymbol{q} = -\kappa \nabla T \tag{1.10}$$

Where τ represents the relaxation time or build up period for the commencement of heat flow after a temperature gradient has been imposed on the medium.

Here we will derive Cattaneo equation from Gray BTE model under the assumption $\nabla_r f \approx \nabla_r f_0 = \frac{df_0}{dT}\frac{dT}{dr}$. Multiplying Eq. (1.9) by $v_x \hbar\omega D(\omega)$ and integrated over all frequency ranges to yield

$$\int_0^{\omega_D} v_x \hbar\omega D(\omega)\left(\frac{\partial f}{\partial t} + v_x \frac{df_0}{dT}\frac{dT}{dr} = -\frac{f - f_0}{\tau}\right) d\omega \tag{1.11}$$

where the second term in the right hand side is zero (v_x is an odd function and f_0 is an even function of v_x), thus the net particle flux vanishes for the equilibrium function f_0. Note that a cut-off frequency is used as the Debye frequency ω_D, where it is assumed that no particles exist above this frequency. Since

$$q_x = \int_0^{\omega_D} v_x \hbar\omega f D(\omega) d\omega \tag{1.12}$$

$$\frac{\partial q_x}{\partial t} = \int_0^{\omega_D} v_x \hbar\omega \frac{\partial f}{\partial t} D(\omega) d\omega \tag{1.13}$$

$$\int_0^{\omega_D} v_x \hbar\omega D(\omega) \tau v_x \frac{df_0}{dT}\frac{dT}{dx} d\omega = \frac{dT}{dx}\int_0^{\omega_D} \tau v_x^2 \hbar\omega D(\omega)\frac{df_0}{dT} d\omega \tag{1.14}$$

Recall that specific heat and thermal conductivity is given as

$$C_\omega = \hbar\omega D(\omega)\frac{df_0}{dT} \tag{1.15}$$

$$\kappa = \int_0^{\omega_D} \tau v_x^2 C_\omega d\omega \tag{1.16}$$

Therefore, substituting Eq. (1.12), (1.13), (1.14), (1.15) and (1.16) into Eq. (1.11), the Cattaneo equation is then derived as

$$\tau\frac{\partial q_x}{\partial t} + q_x = -\kappa\frac{dT}{dx} \tag{1.17}$$

Substituting Eq. (1.17) into the energy equation,

$$C_v \frac{\partial T}{\partial t} + \nabla \cdot \boldsymbol{q} = 0 \tag{1.18}$$

We obtain the hyperbolic heat conduction equation (HHCE)

$$\tau \frac{\partial^2 T}{\partial t^2} + \frac{\partial T}{\partial t} = \frac{\kappa}{C_v} \frac{\partial^2 T}{\partial x^2} \tag{1.19}$$

which describes the heat propagation through the material with a finite speed given by $c = \sqrt{\kappa / \tau C_v}$.

1.4.2 The equation of phonon radiative transfer (EPRT)

The equation of phonon radiative transfer (EPRT) was originally described by Majumdar which made the connection between radiation theory and transport theory in dielectric materials [19]. The intensity of photons, i.e., the radiation emitted in any direction by a wave packet is given by

$$I(\theta, \varphi, \omega, x, t) = \sum_p v(\theta, \varphi) f(x,t) \hbar \omega D(\omega) \tag{1.20}$$

where the summation is over the photon polarizations, is the velocity vector in the direction of θ and φ within a unit solid angle. Multiplying Eq. (1.9) by $v_x \hbar \omega D(\omega)$ and integrated over all frequency ranges, the EPRT is obtained as

$$\frac{\partial I}{\partial t} + v_x \frac{\partial I}{\partial x} = -\frac{I - I^0}{\tau} \tag{1.21}$$

where $v_x = v\mu = v\cos\theta$ is the projection of phonon propagation velocity in the x-direction, and I^0 is the equilibrium intensity. Once the intensity is found by solving the EPRT, the heat flux can be determined as

$$q(x) = \int_{4\pi} \int_0^{\omega_D} \mu I(x, \omega, \Omega) d\omega d\Omega \tag{1.22}$$

The limitations of the analogy between photons and phonons appear in the phonon-phonon interactions, which are absent for photons. These phonon interactions are due to anharmonic forces between atoms and are vital in redistributing energy between different frequencies to restore thermodynamic equilibrium. Another limitation in the EPRT is that the phase of the lattice waves is not considered. Therefore interference effects are neglected.

1.4.3 The ballistic diffusive equation (BDE)

The essence of the ballistic diffusive approximation is to divide the intensity into two components

$$I = I_b + I_d \tag{1.23}$$

Where I_b and I_d are the ballistic and diffusive components respectively. The ballistic component represents phonons emitted from the boundaries and scattered, while the diffuse component represents phonons are emitted from within the medium and scattered. Substitution of Eq. (1.23) into Eq. (1.21), followed by separation of the ballistic and diffusive components, yields

$$\frac{\partial I_b}{\partial t} + \boldsymbol{v} \cdot \nabla_r I_b = -\frac{I_b}{\tau} \tag{1.24}$$

$$\frac{\partial I_d}{\partial t} + \boldsymbol{v} \cdot \nabla_r I_d = -\frac{I_d - I_0}{\tau} \tag{1.25}$$

Following a similar derivation to that in the previous section, we obtain the constitutive relation for the diffusive and ballistic components [22]

$$\frac{\partial \boldsymbol{q}_d}{\partial t} + \boldsymbol{q}_d = -\frac{\kappa}{C_v} \nabla U_d \tag{1.26}$$

$$\tau \frac{\partial U_b}{\partial t} + \nabla \cdot \boldsymbol{q}_b = -U_b \tag{1.27}$$

Combining with energy equation, we end up with

$$\tau \frac{\partial^2 U_d}{\partial t^2} + \frac{\partial U_d}{\partial t} = \nabla \cdot (\frac{k}{C_v} \nabla U_d) - \nabla \cdot \boldsymbol{q}_b \tag{1.28}$$

Eq. (1.28) together with the expressions for the ballistic component is the ballistic diffusive heat conduction equations (BDE). Compared to the original BTE, the BDE is much simpler to solve which averages over the momentum space and thus involves only three spatial coordinates plus one temporal coordinate.

1.4.4 The full dispersion model

The bulk phonon dispersion curves for silicon at 300 K are shown in Fig. 1.1 for three directions. In this model, only one frequency band is used for the optical phonon branch, while there are NLA and NTA bands in the longitudinal acoustic (LA) and transverse acoustic (TA) branches, respectively. The experimental dispersion curves for the LA and TA branches are fit by cubic spines, and all relevant dispersion curve information (e.g., phonon group velocity and density of states) is extracted from these fits. The optical mode for silicon has negligible group velocity and therefore, in this model, as an approximation the ballistic term is absent. The BTE for the optical mode can be written as

$$\frac{\partial e_0}{\partial t} = \sum_{j=1}^{N-1} (\int_{T_{ref}}^{T_{oj}} C_o dT - e_0) \gamma_{oj} + q_{vol} \tag{1.29}$$

Where $e_0 = \int_{T_{ref}}^{T_{oj}} C_o dT$, $\gamma_{oj} = 1/\Delta\omega \int_{\Delta\omega} 1/\tau_{oj} d\omega$ is the band-averaged inverse relaxation time for the interaction between the optical phonons and the j_{th} band of an acoustic branch, and C_o is the optical

mode specific heat. The interaction temperature T_{oj} is defined below and the term q_{vol} is the volumetric heat generation. In microelectronics applications, it would represent the transfer of energy from the energetic electrons to the optical phonons. It is argued by Sverdrup et al. that the electron-phonon interaction can be represented as a heat source term for the phonon BTE since the relaxation time for electron-phonon interaction is about two orders of magnitude smaller than the relaxation time for phonon-phonon scattering. The same approach is adopted in the present study. The BTE for the i_{th} frequency band of the acoustic branches (valid for both LA and TA) in the direction s is written as [23]

$$\partial e_i + \boldsymbol{v}_i \cdot \nabla e_i = (e_i^o - e_i)\gamma_{ii} + \sum_{j=1, j\neq i}^{N} (\int_{T_{ref}}^{T_{ij}} C_i dT - e_i)\gamma_{ij} \tag{1.30}$$

where $\boldsymbol{v}_i = 1/\Delta\omega \int_{\Delta\omega} \boldsymbol{v}_\omega d\omega$ is the band-averaged group velocity, $C_{\omega i}$ the specific heat per unit frequency in band i, $C_i = \int_{\Delta\omega} C_{\omega i} d\omega$ the band integrated specific heat, $e_i = \int_{\Delta\omega} \hbar\omega f D(\omega) d\omega$ the band-integrated energy density per unit solid angle, $\gamma_{ii} = 1/\Delta\omega \int_{\Delta\omega} 1/\tau_{ij} d\omega$ the band-averaged inverse relaxation time for interaction of band i with itself, and γ_{ij} is the band-averaged inverse relaxation time for interaction of band i with band j. The first term on the right hand side (RHS) of Eq. (1.30) depicts scattering within a given frequency band, but across directions (elastic scattering). Physically, processes such as impurity scattering may be described by such a term. The second term on the RHS depicts the scattering from the ith band of the acoustic branch to all other bands in all branches except to itself. T_{ij} is an interaction temperature between the two bands, i and j. In order to satisfy energy conservation, the following two conditions are also satisfied.

$$\int_{T_{ref}}^{T_{ij}} (\frac{C_i}{\Delta\omega_i} + \frac{C_j}{\Delta\omega_j}) dT = \int_{T_{ref}}^{T_i} \frac{C_i}{\Delta\omega_i} dT + \int_{T_{ref}}^{T_j} \frac{C_j}{\Delta\omega_j} dT \tag{1.31}$$

$$e_{total} = \int_{T_{ref}}^{T_L} C dT = \int_{T_{ref}}^{T_o} C_o dT + \sum_{i=1}^{N-1} \int_{T_{ref}}^{T_i} C_i dT \tag{1.32}$$

Eq. (1.31) serves as the definition of the interaction temperature T_{ij}, and is satisfied for all i and j band combinations including the optical phonon band. Eq. (1.32) defines the overall lattice temperature T_L, where *C* is the total specific heat and e_{total} is the total energy density.

The full dispersion model incorporates the interactions between longitudinal acoustic (LA), transverse acoustic (TA) and optical (TO) phonons via frequency dependent relaxation times. The limitation of this model is that one must know the accurate phonon dispersion relationship and relaxation times of the structures which are usually unavailable for nano-/micro-structures.

1.5 Objectives and research tasks

The goals of the current research are to explore the fundamental physics of nano-/micro-scale thermal transport which may help for heat removal strategies and microelectronics cooling designs. In summary, the followings are the objectives and research tasks:

- Develop a high-fidelity enhanced gray BTE (EG-BTE) model that can accurately describe phonon transport at nano-/micro-scale regime.
- Create a theoretical framework based on EG-BTE to replace Fourier's law for experimental data analysis.
- Develop an efficient numerical method to solve EG-BTE which has low computational cost and can deal with complex boundary conditions easily.
- Validate EG-BTE by two benchmark experiments: transient thermal grating (TTG) experiment and time domain thermo-reflectance (TDTR) experiment.

- Apply EG-BTE to systematically study two typical phonon transport problems: phonon transport in thin films and phonon transport in cryogenic crystals.

1.6 Outline of the thesis

In chapter 2, a new version of BTE named enhanced gray model (EG-BTE) has been developed to capture the phonon nonlocal effect in nano-/micro-structures. A constitutive equation of heat flux and temperature is also derived which is compatible with Guyer-Krumhansl equation or two-parameter heat conduction model. The analytical solution of EG-BTE is also obtained based on Fourier transform in frequency domain. Chapter 3 describes the development of the implicit lattice Boltzmann method (LBM) to solve EG-BTE, which is unconditionally stable and computationally efficient. To our best knowledge, the implicit LBM is the first time to be developed and implemented to solve BTE.

In chapter 4, EG-BTE is validated with the transient thermal grating (TTG) and time domain thermo-reflectance (TDTR) experiments. We show that integrating gray-medium solutions can reasonably reproduce the thermal conductivity for different grating periods. For validation, theoretical solution of EG-BTE for TTG in three dimensional domain is developed, and perfect match is obtained between the numerical results and theoretical results. The effective thermal conductivity profiles are obtained, and we conclude that the deduction of effective thermal conductivity is due to nonlocal transport of phonons with long mean free path (MFP). We also present a theoretical framework to interpret time domain thermos-reflectance (TDTR) experiments based on EG-BTE. The TDTR measurements reveal the failure of Fourier's law. Besides, Fourier's law overpredicts the interfacial thermal conductance compared to the result by EG-BTE.

Chapter 5 presents our theoretical and numerical study of non-diffusive heat transport in thin films and cryogenic crystals based on EG-BTE. The predictions of present model with absorption boundary give better interpretations of experimental results than the Majumdar's model and Sondheimer's model, which overpredict the thermal conductivity using diffusive reflection boundary condition. The validity of EG-BTE is confirmed by reproducing the ballistic heat transport in heat-pulse experiments conducted in cryogenic crystals. The physical nature of non-diffusive phonon transport is investigated in detail.

In Chapter 6, we have studied the thermal dynamics of nonequilibrium electrons and phonons in metals. We present a refined model to describe the relationship between reflectance and temperature which would provide a much more reliable results to extract the thermal properties of metal films and other samples in pump-probe methodology.

The final summary and future work are presented in Chapter 7.

Chapter 2

Theory for Enhanced Gray Boltzmann Transport Equation

2.1 Derivation of Enhanced Gray BTE

A phonon is a quasiparticle representing a quantum mechanical description of lattice vibration modes of elastic solid crystals. The state of a phonon particle in the phase space is characterized by a distribution function *f(t,**r**,**v**)* at the time *t* in a physical space described by a coordinate vector **r** and a phase space described by a velocity vector ***v***. At the time $t+\Delta t$, the distribution function changes to be $f(t+\Delta t, \boldsymbol{r}+\Delta \boldsymbol{r}, \boldsymbol{v}+\Delta \boldsymbol{v})$. In the Liouville system [24], the particles do not collide during the time interval Δt, so the distribution function is conserved, i.e.,

$$f(t+\Delta t, \boldsymbol{r}+\Delta \boldsymbol{r}, \boldsymbol{v}+\Delta \boldsymbol{v}) - f(t, \boldsymbol{r}, \boldsymbol{v}) = 0 \tag{2.1}$$

However, if the time intervals are large, the distribution function is no longer conserved due to collisions between particles. Assuming the net rate of gaining particles is $\left(\frac{\partial f}{\partial t}\right)_c$, the change of distribution function is given by [24-26]

$$f(t+\Delta t, \boldsymbol{r}+\Delta \boldsymbol{r}, \boldsymbol{v}+\Delta \boldsymbol{v}) - f(t, \boldsymbol{r}, \boldsymbol{v}) = \left(\frac{\partial f}{\partial t}\right)_c \Delta t \tag{2.2}$$

By default, symbols in bold fonts denote the vectors, while the same symbols in normal fonts denote their magnitudes. If we truncate the Taylor expansion of $f(t+\Delta t, \boldsymbol{r}+\Delta \boldsymbol{r}, \boldsymbol{v}+\Delta \boldsymbol{v})$ around $(t, \boldsymbol{r}, \boldsymbol{v})$ at first order and assume there are no external forces, the Eq. (2.2) under a simple relaxation time approximation [27] is

$$\frac{\partial f}{\partial t} + \boldsymbol{v} \cdot \nabla f = -\frac{f - f^0}{\tau_R} \tag{2.3}$$

where f^0 is the equilibrium distribution function, and τ_R is the relaxation time. For the sake of brevity, we omit (t,$\boldsymbol{r}$,$\boldsymbol{v}$) without causing any ambiguity. The physical meaning of the relaxation time (τ_R) is a measurement of how long it takes for a local nonequilibrium state to reach an equilibrium state. The diffusive relaxation time τ_R can be determined from the simple kinetic theory, $\tau_R = 3\kappa / C_v v^2$. The equilibrium distribution function for phonons is given by the Bose-Einstein distribution

$$f^0 = \frac{1}{\exp(\hbar\omega / k_B T) - 1} \tag{2.4}$$

where $\hbar$ is the Planck constant divided by 2π, ω is the phonon frequency, k_B is the Boltzmann constant, and T is the absolute temperature.

The Gray model expressed in Eq. (2.3) is derived from Eq. (2.2) based on the truncation to the first-order Taylor expansion of the distribution function under the assumption that both Δt and $\Delta \boldsymbol{r}$ are much smaller than the time scale and the length scale of heat transfer. However, for heat transfer in micro-/nano-systems, the length scale of interests is comparable with a phonon mean free path (MFP), so there is nonlocal effect resulting from ballistic phonon transport [28-30]. To

account for the nonlocal effect, we need to truncate the Taylor series to the second order for the spatial derivative and the cross derivative of $f(t+\Delta t, \boldsymbol{r}+\Delta \boldsymbol{r}, \boldsymbol{v}+\Delta \boldsymbol{v})$, i.e., [5]

$$\frac{\partial f}{\partial t}+\boldsymbol{v}\cdot\nabla f+\frac{1}{2}\left[2\tau_c \boldsymbol{v}\cdot\nabla\frac{\partial f}{\partial t}+\tau_c(\boldsymbol{v}\cdot\nabla)^2 f\right]=-\frac{f-f^0}{\tau_R} \tag{2.5}$$

where τ_c is a characteristic time to account for nonlocal effects from ballistic phonon transport. In Eq. (2.5), the second order temporal derivative is negligible under the assumption that the time scale for heat transfer is much larger than the characteristic time τ_c. The physical meaning of τ_c is same as that of τ_B in a two-parameter non-diffusive heat conduction model reported by Ma [31], i.e., ballistic average mean free time mainly contributed by long mean free path (MFP) phonons. Similarly, the physical meaning of τ_R can be interpreted as diffusive average mean free time mainly contributed by short MFP phonons. Here is an example to show the difference between τ_R and τ_c in Si at room temperature (κ = 148 W/mK, C_v = 1.66×106 J/m3K, v = 6400 m/s). Based on the simple kinetic theory, the diffusive relaxation time is determined as $\tau_R = 3\kappa / C_v v^2 = 6.53$ ps and diffusive phonon MFP $\Lambda_D = v\tau_R = 42$ nm. From the TTG experiment [12] to be discussed in chapter 4, we obtain τ_c = 0.45 ns and ballistic MFP $\Lambda_B = v\tau_c$ = 2.88 μm by curve fitting the experimental data.

It should be noted that the last term on the left hand side of Eq. (2.5) does not contribute to heat transfer. Multiplying $\tau_c(\boldsymbol{v}\cdot\nabla)^2 f$ by $\boldsymbol{v}\hbar\omega D(\omega)/4\pi$ and integrating over all frequency range and solid angle, the x-component of the integral is

$$\int_{4\pi}\int_0^{\omega_D} v_x \hbar\omega\tau_c(\boldsymbol{v}\cdot\nabla)^2 f\frac{D(\omega)}{4\pi}d\omega d\Omega=\int_0^{\omega_D}\hbar\omega\tau_c\frac{D(\omega)}{4\pi}d\omega\int_{4\pi}v_x\Big(\sum_{i=x,y,z}v_i\partial_i\Big)^2 f d\Omega \tag{2.6}$$

The integral over solid angle in Eq. (2.6) can be approximated as

$$\int_{4\pi} v_x \Big(\sum_{i=x,y,z} v_i \partial_i \Big)^2 f d\Omega = \int_{4\pi} v_x \sum_{j=x,y,z} \sum_{i=x,y,z} v_i v_j \partial_i \Big(\frac{df^0}{dT} \partial_j T \Big) d\Omega \tag{2.7}$$

It is straightforward to obtain the following integrals

$$\begin{aligned}
\int_{4\pi} v_x^3 d\Omega &= \int_0^{2\pi} \int_0^{\pi} v^3 (\sin\theta\cos\varphi)^3 \sin\theta d\theta d\varphi = 0 \\
\int_{4\pi} v_x^2 v_y d\Omega &= \int_0^{2\pi} \int_0^{\pi} v^3 (\sin\theta\cos\varphi)^2 \sin\theta\sin\varphi \sin\theta d\theta d\varphi = 0 \\
\int_{4\pi} v_x^2 v_z d\Omega &= \int_0^{2\pi} \int_0^{\pi} v^3 (\sin\theta\cos\varphi)^2 \cos\theta \sin\theta d\theta d\varphi = 0 \\
\int_{4\pi} v_x v_y^2 d\Omega &= \int_0^{2\pi} \int_0^{\pi} v^3 \sin\theta\cos\varphi (\sin\theta\sin\varphi)^2 \sin\theta d\theta d\varphi = 0 \\
\int_{4\pi} v_x v_z^2 d\Omega &= \int_0^{2\pi} \int_0^{\pi} v^3 \sin\theta\cos\varphi \cos^2\theta \sin\theta d\theta d\varphi = 0 \\
\int_{4\pi} v_x v_y v_z d\Omega &= \int_0^{2\pi} \int_0^{\pi} v^3 \sin\theta\cos\varphi \sin\theta\sin\varphi \cos\theta \sin\theta d\theta d\varphi = 0
\end{aligned} \tag{2.8}$$

Substituting Eq. (2.8) into Eq. (2.7), we obtain $\int_{4\pi} v_x \Big(\sum_{i=x,y,z} v_i \partial_i \Big)^2 f d\Omega = 0$. Plugging it into Eq. (2.6), we have

$$\int_{4\pi} \int_0^{\omega_D} v_x \hbar\omega \tau_c (\boldsymbol{v} \cdot \nabla)^2 f \frac{D(\omega)}{4\pi} d\omega d\Omega = 0 \tag{2.9}$$

Similarly, the y and z-component of the integral can be obtained to be 0. Finally we reach our conclusion that is

$$\int_{4\pi} \int_0^{\omega_D} \boldsymbol{v} \hbar\omega \tau_c (\boldsymbol{v} \cdot \nabla)^2 f \frac{D(\omega)}{4\pi} d\omega d\Omega = 0 \tag{2.10}$$

Accordingly we obtain the enhanced Gray (EG) model (called EG-BTE),

$$\frac{\partial f}{\partial t} + \boldsymbol{v} \cdot \nabla f = -\frac{f - f^0}{\tau_R} - \tau_c \boldsymbol{v} \cdot \nabla \frac{\partial f}{\partial t} \tag{2.11}$$

Similar to the Gray model described in Eq. (2.3), we assume that v, τ_R, and τ_c are isotropic and independent of phonon frequency, and polarization. Compared with Eq. (2.3), τ_c is the only extra parameter in the EG-BTE model that is used to account for the nonlocal effect resulting from ballistic phonon transport.

To derive the internal energy equation, we define the following quantities [23, 32]

$$\dot{e} = \frac{1}{4\pi}\hbar\omega f D(\omega); \quad e = \int_0^{\omega_D} \dot{e} d\omega; \quad E = \int_{4\pi} e d\Omega \tag{2.12}$$

where $\dot{e}$ is the volumetric energy density per unit frequency per unit solid angle, e is the volumetric energy density per unit solid angle, E is the volumetric energy density, ω is phonon frequency, Ω is the solid angle, ω_D is Debye cutoff frequency, and $D(\omega)$ is the phonon density of states (or the number of states per unit volume and per unit interval of the frequency). Multiplying Eq. (2.11) with $\hbar\omega D(\omega)/4\pi$ and integrating over all frequency range, we obtain energy density formulation

$$\frac{\partial e}{\partial t} + \boldsymbol{v}\cdot\nabla e = -\frac{e - e^0}{\tau_R} - \tau_c \boldsymbol{v}\cdot\nabla\frac{\partial e}{\partial t} \tag{2.13}$$

in which e^0 is the equilibrium energy density per unit solid angle. The heat flux can be calculated as [20, 23]

$$\boldsymbol{q} = \int_{4\pi} \boldsymbol{v} e d\Omega \tag{2.14}$$

2.2 Contribution of long MFP phonons

The phonon mean free path (MFP) Λ is a function of phonon frequency ω, i.e., $\Lambda(\omega) = \tau(\omega)v(\omega)$, where τ is phonon relaxation time and v is phonon group velocity. In previous section, we have obtained two length scales: Λ_D characterizing the short MFP scale of phonons, and Λ_B characterizing the long MFP scale of phonons. From the statistical point of view, the two length scales (Λ_D and Λ_B) are interpreted as average MFPs of two different phonon groups in full

spectrum. The short MFP (Λ_D) is the average MFP of high-frequency phonon group, while the long MFP (Λ_B) is the average MFP of low-frequency phonon group.

The contribution of long MFP phonons to thermal conductivity can be qualitatively analyzed. The thermal conductivity is calculated as

$$\kappa = \frac{1}{3}\int_0^{\omega_{\max}} C_\omega v(\omega)\Lambda(\omega)d\omega \tag{2.15}$$

where $C_\omega = \hbar\omega D(\omega)\frac{df^0}{dT}$ is the specific heat at frequency ω and temperature T. The definition of $D(\omega)$ and f^0 are described in section 2.1. From Eq. (2.15), we know that thermal conductivity will decrease if the long MFP phonons are suppressed. Here we provide two typical examples where long MFP phonons will be suppressed. The first example is phonon transport in the thin films which is discussed in Chapter 5. The effective thermal conductivity of thin films reduces with decreasing film thickness. This is explained as the transport of long MFP phonons are suppressed by the film thickness. With smaller film thickness, more phonons with MFP above the thickness are suppressed. The second example is phonon transport in transient thermal grating (TTG) experiment which is discussed in Chapter 4. In the TTG experiment, a periodic sinusoidal heating source with period L is applied on the surface of Si membrane. The measured thermal conductivity of Si membrane decreases as L decreases. According to Minnich et al. [33, 34], phonons with long MFP comparable to or above L are not excited, therefore the long MFP phonons will not contribute to thermal transport.

2.3 Derivation of Macroscopic Constitutive Equation

The constitutive equation of heat flux and temperature can be derived under the assumption that $\nabla f = \frac{df^0}{dT}\nabla T$ [19, 20]. Multiplying $\boldsymbol{v}\cdot\nabla f$ by $\boldsymbol{v}\hbar\omega D(\omega)/4\pi$ and integrating over all frequency range and solid angle yields

$$\int_{4\pi}\int_0^{\omega_D} \boldsymbol{v}\hbar\omega\boldsymbol{v}\cdot\nabla f \frac{D(\omega)}{4\pi}d\omega d\Omega = \int_{4\pi}\int_0^{\omega_D} \boldsymbol{v}\hbar\omega\boldsymbol{v}\cdot(\frac{df^0}{dT}\nabla T)\frac{D(\omega)}{4\pi}d\omega d\Omega \tag{2.16}$$

The x-component of the integral is calculated as

$$\int_{4\pi}\int_0^{\omega_D} v_x\hbar\omega\boldsymbol{v}\cdot(\frac{df^0}{dT}\nabla T)\frac{D(\omega)}{4\pi}d\omega d\Omega = \int_0^{\omega_D}\hbar\omega\frac{df^0}{dT}\frac{D(\omega)}{4\pi}d\omega\int_{4\pi} v_x\sum_{i=x,y,z} v_i\partial_i T d\Omega \tag{2.17}$$

where $\sum_{i=x,y,z} v_i\partial_i T = v_x\frac{\partial T}{\partial x}+v_y\frac{\partial T}{\partial y}+v_z\frac{\partial T}{\partial z}$. Since $\boldsymbol{v}$ is the velocity vector in **k**-space, we have $\boldsymbol{v} = v\sin\theta\cos\varphi\hat{x}+v\sin\theta\sin\varphi\hat{y}+v\cos\theta\hat{z}$. It is straightforward to obtain the following integrals

$$\begin{aligned}
&\int_{4\pi} v_x v_x d\Omega = \int_0^{2\pi}\int_0^{\pi} v^2(\sin\theta\cos\varphi)^2\sin\theta d\theta d\varphi = \frac{4\pi}{3}v^2\\
&\int_{4\pi} v_x v_y d\Omega = \int_0^{2\pi}\int_0^{\pi} v^2\sin\theta\cos\varphi\sin\theta\sin\varphi\sin\theta d\theta d\varphi = 0\\
&\int_{4\pi} v_x v_z d\Omega = \int_0^{2\pi}\int_0^{\pi} v^2\sin\theta\cos\varphi\cos\theta\sin\theta d\theta d\varphi = 0
\end{aligned} \tag{2.18}$$

Based on Eq. (2.18), the integral over solid angle in Eq. (2.17) is calculated as

$$\int_{4\pi} v_x\sum v_x\frac{\partial T}{\partial x}d\Omega = \frac{4\pi}{3}v^2\frac{\partial T}{\partial x} \tag{2.19}$$

Substituting Eq. (2.19) into Eq. (2.17), we have

$$\int_{4\pi}\int_0^{\omega_D} v_x\hbar\omega\boldsymbol{v}\cdot(\frac{df^0}{dT}\nabla T)\frac{D(\omega)}{4\pi}d\omega d\Omega = \frac{\partial T}{\partial x}\int_0^{\omega_D}\frac{v^2}{3}\hbar\omega\frac{df^0}{dT}D(\omega)d\omega = \frac{\kappa}{\tau_R}\frac{\partial T}{\partial x} \tag{2.20}$$

where the conductivity is $\kappa = \int_0^{\omega_D}\frac{\tau_R v^2}{3}\hbar\omega\frac{df^0}{dT}D(\omega)d\omega$. Follow the same procedure, we can get the y and z-component of the integral in Eq. (2.16). Finally we have

$$\int_{4\pi}\int_0^{\omega_D}\boldsymbol{v}\hbar\omega\boldsymbol{v}\cdot\nabla f\frac{D(\omega)}{4\pi}d\omega d\Omega = \frac{\kappa}{\tau_R}\nabla T \tag{2.21}$$

Similarly, we can obtain

$$\int_{4\pi}\int_{0}^{\omega_D} \boldsymbol{v}\hbar\omega\tau_c\boldsymbol{v}\cdot\nabla\frac{\partial f}{\partial t}\frac{D(\omega)}{4\pi}d\omega d\Omega = \frac{\tau_c\kappa}{\tau_R}\nabla\frac{\partial T}{\partial t} \tag{2.22}$$

Therefore, multiplying Eq. (2.11) with $\boldsymbol{v}\hbar\omega D(\omega)/4\pi$ and integrating over all frequency range and solid angle gives

$$\frac{\partial \boldsymbol{q}}{\partial t}+\frac{\kappa}{\tau_R}\nabla T = -\frac{\boldsymbol{q}}{\tau_R}-\frac{\kappa\tau_c}{\tau_R}\nabla\frac{\partial T}{\partial t} \tag{2.23}$$

where $\kappa = \frac{1}{3}C_v v^2\tau_R$ is the thermal conductivity, and C_v is specific heat per unit volume. The first law of thermodynamics states that

$$C_v\frac{\partial T}{\partial t}+\nabla\cdot\boldsymbol{q}=0 \tag{2.24}$$

Substituting Eq. (2.24) into Eq. (2.23) to eliminate $\frac{\partial T}{\partial t}$ gives

$$\frac{\partial \boldsymbol{q}}{\partial t}+\frac{\kappa}{\tau_R}\nabla T = -\frac{\boldsymbol{q}}{\tau_R}+\frac{\kappa\tau_c}{C_v\tau_R}\nabla(\nabla\cdot\boldsymbol{q}) \tag{2.25}$$

Eq. (2.25) can be rearranged as

$$\tau_R\frac{\partial \boldsymbol{q}}{\partial t}+\boldsymbol{q} = -\kappa\nabla T+\frac{\Lambda_D\Lambda_B}{3}\nabla(\nabla\cdot\boldsymbol{q}) \tag{2.26}$$

where $\frac{\kappa\tau_c}{C_v}=\frac{C_v v^2\tau_R\tau_c}{3C_v}=\frac{\Lambda_D\Lambda_B}{3}$, $\Lambda_D = v\tau_R$ the diffusive mean free path, and $\Lambda_B = v\tau_c$ the ballistic mean free path. If the time scale of interests is much larger than τ_R, $\tau_R\frac{\partial \boldsymbol{q}}{\partial t}$ is negligible, and the Eq. (2.26) is consistent with the equation derived in the previous work reported by Ma [31].

Combining Eq. (2.25) and energy conservation equation to eliminate $\boldsymbol{q}$, we arrive at the temperature equation

$$\tau_R \frac{\partial^2 T}{\partial t^2} + \frac{\partial T}{\partial t} = \frac{\kappa}{C_v}\nabla^2 T + \frac{\kappa \tau_c}{C_v}\frac{\partial}{\partial t}(\nabla^2 T) \tag{2.27}$$

Assuming the magnitude of τ_c is on the same order as the normal collision time τ_N, i.e., $\tau_c = \alpha\tau_N$, and setting $\alpha = 9/5$, we obtain the same temperature equation as that of Guyer-Krumhansl equation [35, 36]. Therefore, the constitutive equation Eq. (2.26) is also compatible with Guyer-Krumhansl equation [37].

2.4 Analytical Solution of EG-BTE

In this section, we provide a theoretical framework for analysing multidimensional heat conduction based on the Fourier transform. The EG-BTE with a volumetric heat generation $Q(t,\boldsymbol{r}) = \delta(t)Q(\boldsymbol{r})$ is given by

$$\frac{\partial e}{\partial t} + \boldsymbol{v}\cdot\nabla e = -\frac{e - e^0}{\tau_R} - \tau_c \boldsymbol{v}\cdot\nabla\frac{\partial e}{\partial t} + Q(\boldsymbol{r})\delta(t) \tag{2.28}$$

where the equilibrium energy density $e^0 = \int_0^{\omega_D} \frac{1}{4\pi}\hbar\omega f^0(T)D(\omega)d\omega \approx \frac{1}{4\pi}C_v T$ [9]. From the energy conservation law and assuming a gray medium, we obtain

$$e^0 = \frac{1}{4\pi}\int_{4\pi} e\, d\Omega \tag{2.29}$$

For the brevity, we consider the one-dimensional (1D) case first. The phonon group velocity in x-direction is $\boldsymbol{v} = v\sin\theta\cos\varphi\hat{x}$, and the gradient of energy density is $\nabla e = \frac{\partial e}{\partial x}\hat{x}$, so the Eq. (2.28) in 1D domain can be rewritten as

$$\frac{\partial e}{\partial t}+v\sin\theta\cos\varphi\frac{\partial e}{\partial x}=-\frac{e-e^0}{\tau_R}-\tau_c v\sin\theta\cos\varphi\frac{\partial^2 e}{\partial t\partial x}+Q(\mathrm{x})\delta(\mathrm{t}) \tag{2.30}$$

Taking a Fourier transform in time and space leads to

$$i\eta\tilde{e}+i\xi_x v\sin\theta\cos\varphi\tilde{e}=-\frac{\tilde{e}-\tilde{e}^0}{\tau_R}+\eta\tau_c\xi_x v\sin\theta\cos\varphi\tilde{e}+\tilde{Q}(\xi_x) \tag{2.31}$$

where $e=\iint e(t,x)e^{-i\eta t-i\xi_x x}dtdx$, η and ξ_x are the Fourier variables in temporal and spatial domains.

Rearranging Eq. (2.31) gives

$$\tilde{e}=\frac{\tilde{e}^0+\tau_R\tilde{Q}}{1+i\eta\tau_R+(i-\eta\tau_c)\xi_x\Lambda_D\sin\theta\cos\varphi} \tag{2.32}$$

where $\Lambda_D=v\tau_R$. Integrating over all solid angle to satisfy energy conservation as shown in Eq. (2.29), gives

$$\tilde{e}^0=\frac{1}{4\pi}\int_0^{2\pi}\int_0^{\pi}\frac{\tilde{e}^0+\tau_R\tilde{Q}}{1+i\eta\tau_R+(i-\eta\tau_c)\xi_x\Lambda_D\sin\theta\cos\varphi}\sin\theta d\theta d\varphi \tag{2.33}$$

From Eq. (2.33), we get the explicit expression for $\tilde{e}^0$

$$\tilde{e}^0=\frac{\tau_R\tilde{Q}\mathcal{A}(\eta,\xi_x)}{1-\mathcal{A}(\eta,\xi_x)} \tag{2.34}$$

$$\mathcal{A}(\eta,\xi_x)=\frac{1}{(1+i\eta\tau_c)Kn}\tan^{-1}\left(\frac{1+i\eta\tau_c}{1+i\eta\tau_R}Kn\right) \tag{2.35}$$

where $Kn=\xi_x\Lambda_D$. In the weakly ballistic regime where $\eta\tau_R\ll 1$ and $\eta\tau_c Kn\ll 1$, the Taylor expansion of $\mathcal{A}(\eta,\xi_x)$ around $\eta\tau_R=0$ and $\eta\tau_c Kn=0$ in first order is

$$\mathcal{A}(\eta,\xi_x)=\frac{1}{1+i2\eta\tau_c Kn^2}\left[\frac{\tan^{-1}(Kn)}{Kn}-i\eta\tau_R+i\eta\tau_c\left(1+(Kn^2-1)\frac{\tan^{-1}(Kn)}{Kn}\right)\right] \tag{2.36}$$

Recalling the equilibrium energy density $e^0 = \int_0^{\omega_D} \frac{1}{4\pi} \hbar\omega f^0(T) D(\omega) d\omega \approx \frac{1}{4\pi} C_v T$, the temperature response in the Fourier transform formula is given by

$$\tilde{T} = \frac{4\pi\tau_R \tilde{Q} \mathcal{A}(\eta, \xi_x)}{C_v (1 - \mathcal{A}(\eta, \xi_x))} \tag{2.37}$$

The result can be simplified by using Eq. (2.36), and neglecting the terms which may not affect the decay rate after an inverse Fourier transform. The result is as follows:

$$\tilde{T}(\eta, \xi_x) = \frac{\tilde{Q}(\eta, \xi_x)}{i\eta C_v + \kappa(\xi_x)\xi_x^2} \tag{2.38}$$

$$\kappa(\xi_x) = \frac{3\kappa}{Kn^2} \frac{1 - \frac{\tan^{-1}(Kn)}{Kn}}{1 - \frac{\tau_c}{\tau_R}(1 - 2Kn^2 + (Kn^2 - 1)\frac{\tan^{-1}(Kn)}{Kn})} \tag{2.39}$$

where $\kappa(\xi_x)$ is the effective thermal conductivity, and the Knudsen number is $Kn = \xi_x \Lambda_D$. The analytic solution of temperature response is obtained by performing an inverse Fourier transform over space and time in Eq. (2.38)

$$T(t, \mathrm{x}) = \mathcal{F}^{-1}(\tilde{T}) = A \int \tilde{\mathrm{Q}}(\xi_x) \exp[-\xi_x^2 \frac{\kappa(\xi_x)}{C_v} t + i\xi_x x] d\xi_x \tag{2.40}$$

where *A* is an arbitrary constant.

We now specialize this result for the 1D TTG experiment. Along the in-plane, or x-direction, the heating profile is a sinusoid with spatial frequency $\frac{2\pi}{L}$ for grating period *L*, i.e.,

$$\tilde{Q} = Q_0 \iint e^{i\frac{2\pi}{L}x - i\eta t - i\xi_x x} \delta(t) d\eta d\xi_x = 2\pi Q_0 \delta(\xi_x - \frac{2\pi}{L}) \tag{2.41}$$

Substituting the above equation into Eq. (2.40), the temperature response of 1D TTG can be obtained

$$T(t,\mathrm{x}) = A\exp[-\xi_x^2\alpha(\xi_x)t + i\xi_x x] \tag{2.42}$$

where A is an arbitrary constant, the apparent thermal diffusivity is $\alpha(\xi_x) = \kappa(\xi_x)/C_v$, $\xi_x = \frac{2\pi}{L}$, and L is the grating period.

For the general three dimensional (3D) case, following the same procedure described in 1D section, we get the solution of equilibrium energy density in the Fourier transform formula as follows:

$$\tilde{e}^0 = \frac{\tau_R \tilde{Q}\mathcal{A}(\eta,\xi)}{1-\mathcal{A}(\eta,\xi)} \tag{2.43}$$

$$\mathcal{A}(\eta,\xi) = \frac{1}{(1+i\eta\tau_c)Kn}\tan^{-1}\left(\frac{1+i\eta\tau_c}{1+i\eta\tau_R}Kn\right) \tag{2.44}$$

where the magnitude of spatial frequency is $\xi = \sqrt{\xi_x^2+\xi_y^2+\xi_z^2}$, the Knudsen number is $Kn = \xi\Lambda_D$, ξ_x, ξ_y, ξ_z are the Fourier variables in the spatial domain. The temperature response in the Fourier transform formula is given by

$$\tilde{T}(\eta,\xi) = \frac{\tilde{Q}(\eta,\xi)}{i\eta C_v + \kappa(\xi)\xi^2} \tag{2.45}$$

$$\kappa(\xi) = \frac{3\kappa}{Kn^2}\frac{1-\frac{\tan^{-1}(Kn)}{Kn}}{1-\frac{\tau_c}{\tau_R}\left(1-2Kn^2+(Kn^2-1)\frac{\tan^{-1}(Kn)}{Kn}\right)} \tag{2.46}$$

Again, the Eq. (2.45) is obtained by neglecting the terms which may not affect the decay rate after an inverse Fourier transform.

We now specialize the results for the 2D TTG experiment. Along the in-plane, or x-direction, the heating profile is a sinusoid with spatial frequency $\frac{2\pi}{L}$ for grating period *L*. Along the cross-plane, or y-direction, the heating profile is a decaying exponential with the absorption coefficient β_1 for the pump beam. The heating along the z-direction is uniform, and hence $\xi_z = 0$. The Fourier transform of the heating source is

$$\tilde{Q} = Q_0 \iiint e^{i\frac{2\pi}{L}x - \beta_1 y - i\eta t - i\xi_x x - i\xi_y y} \delta(t) d\eta d\xi_x d\xi_y = 4\pi Q_0 \delta(\xi_x - \frac{2\pi}{L}) \frac{\beta_1}{\beta_1^2 + \xi_y^2} \tag{2.47}$$

The probe signal $\tilde{H}$ in frequency domain is obtained by weighing the temperature response by the probe intensity distribution

$$\tilde{H}(\eta, \xi_x) = \int_0^\infty \tilde{T}(\eta, \xi_x, \xi_y) \frac{2\beta_2}{\beta_2^2 + \xi_y^2} d\xi_y \tag{2.48}$$

where β_2 is the absorption coefficient for the pump beam. This equation can be converted to the time domain as

$$H(\mathrm{t}, x) = Ae^{i\frac{2\pi}{L}x} \int_0^\infty \frac{\exp[-\alpha(\xi)\xi^2 t]}{(\beta_1^2 + \xi_y^2)(\beta_2^2 + \xi_y^2)} d\xi_y \tag{2.49}$$

where *A* is an arbitrary constant, $\alpha(\xi) = \kappa(\xi)/C_v$ is the apparent thermal diffusivity, and the total spatial frequency is $\xi = \sqrt{(2\pi / L)^2 + \xi_y^2}$. If the in-plane spatial frequency $\xi_x = 2\pi/L$ is much larger than the cross-plane spatial frequency ξ_y, the transport can be treated as 1D. The probe signal profile *H*(t,x) is a multiexponential decay with the relative contribution weighted by the Fourier transform of the cross-plane heating profile.

Chapter 3

Lattice Boltzmann Method

In this study, we take lattice Boltzmann method (LBM) as our fundamental numerical method. Derived directly from the continuous Boltzmann equation [38], LBM have many distinctive features such as the clear physics picture, the simple structure, the easy implementation of boundary conditions, and the natural parallelism. These features have made it a powerful tool for simulating flow and heat transfer problems involving complex physics. Actually, the past several decades have witnessed the amazing success of the LBM in modelling and simulating complicated transport problems such as multi-phase flows in porous media, diffusion and chemical reactions, combustion, and microscale heat transfer [39-44].

3.1 Theory of Lattice Boltzmann Method

The lattice Boltzmann method (LBM) is a discrete development of the BTE, which can be used to simulate energy transport problems within the applicability range of the BTE; that is, within time scales larger than the collision time and length scales larger than the phonon wavelength. The LBM discretizes the space domain by defining lattice sites where the phonon energy density is calculated. Phonons generated at a particular lattice site will propagate only to a neighboring lattice site by traveling ballistically at a speed of c and collide with phonons generated at that lattice site.

The time domain is also discretized by restricting the phonons to travel from one lattice site to the neighboring lattice in a definite time step, which corresponds to the site-to-site transport restriction.

3.1.1 Lattice Boltzmann kinetic equation

As presented in the previous chapter the Boltzmann transport equation can be written in the following form, assuming the relaxation time approximation for the collision operator

$$\frac{\partial f}{\partial t} + \boldsymbol{v} \cdot \nabla_r f = -\frac{f - f_0}{\tau} \tag{3.1}$$

This equation is formulated to account for transport in any direction $\boldsymbol{v}$. To solve this equation with the LB method, the velocity space must first be discretized [38]. This amounts to projecting the distribution function in discrete directions that describe paths that particles are allowed to travel. The discrete form of the BTE can then be written as

$$\frac{\partial f_i}{\partial t} + \boldsymbol{v}_i \cdot \nabla_r f_i = -\frac{f_i - f_i^0}{\tau} \tag{3.2}$$

where i is a direction subscript and other variables have their usual definitions. With the velocity space now discretized it is possible to deal with the gradient operator as well as the time derivative. By approximating each term with a first order Taylor expansion (assuming a 1D domain) the discrete form is found as

$$\frac{f_i(t+\Delta t, x) - f_i(t,x)}{\Delta t} + v_i \frac{f_i(t+\Delta t, x+\Delta x) - f_i(t+\Delta t, x)}{\Delta x} = -\frac{f_i - f_i^0}{\tau} \tag{3.3}$$

By setting $\Delta x = v\Delta t$, the so called explicit Lattice Boltzmann Kinetic Equation (LBKE) is obtained

$$f_i(t+\Delta t, x+\Delta x) = (1-\frac{\Delta t}{\tau}) f_i(t,x) + \frac{\Delta t}{\tau} f_i^0(t,x) \tag{3.4}$$

By multiplying $\hbar\omega D(\omega)$ on both sides of Eq. (3.4) and integrated over all frequency ranges, we will obtain the energy density form of the LBKE

$$e_i(t+\Delta t, x+\Delta x) = (1-\frac{\Delta t}{\tau})e_i(t,x) + \frac{\Delta t}{\tau}e_i^0(t,x) \tag{3.5}$$

where $e_i = \int \hbar\omega D(\omega) f_i d\omega$ is called the "directional phonon energy". The directional equilibrium energy is referred to as e_i^0. The LBKE has a simple physical analogue that can provide some valuable insight in to the application of LB method. Typically the LB method is described as a "stream and collide" method. When a computational domain is defined particles are assumed to exist in cells at their center node location. These particles are allowed to propagate to the nearest neighboring nodes; this is the "streaming" step of the method. Upon arrival at the next lattice site the incoming particles are allowed to collide with other incoming particles (from other directions). The equilibrium distribution is found by averaging all of the incoming non-equilibrium distribution functions. This process is then repeated for the necessary simulation time.

There are a few properties of the LBKE that must be pointed out before going into the details of the lattice types. In the present form the LBKE is an explicit equation, which makes it subject to convergence criteria. A stability requirement restricts $\frac{\Delta t}{\tau} < 1$; thus the time step Δt must be smaller than the phonon relaxation time.

3.1.2 Lattice types

Lattice types are labelled following the DmQn convention, where m is the dimensionality of the domain and n is the number of discrete velocities per node. While there are several choices for LB lattices, two of the most common, i.e., D2Q4 lattice and D2Q9 lattice are shown in Fig. 3.1.

It is traditional notation to use the "D2Q9" label even though the ninth velocity at the center node is set to zero due to the zero phonon group velocity at that location [45]. It is also possible to generate hexagonal lattices. This particular shape is useful when domains with hexagonal symmetry are used. This particular lattice shape will not be used in this study; instead the focus will be on the D1Q2 and D2Q4 lattices. Whichever lattice is used, there are symmetry conditions that must be met in order to satisfy conservation of energy.

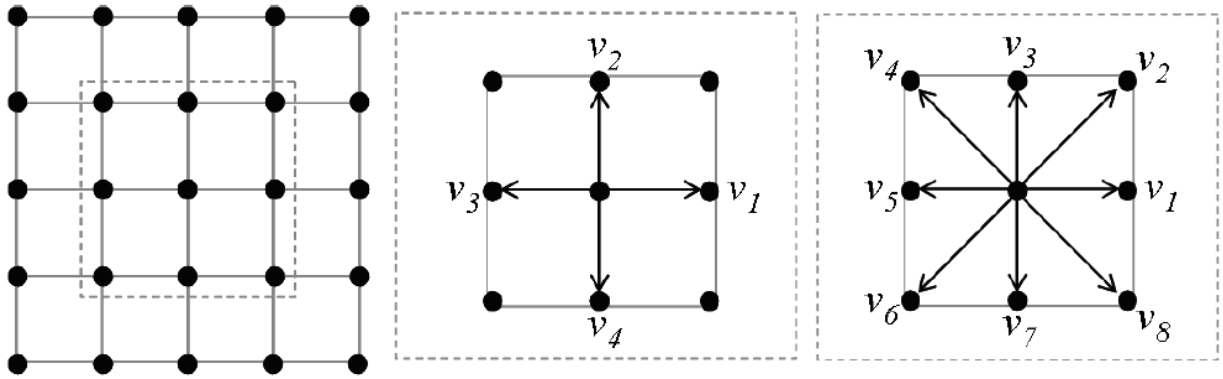

Figure 3.1. A regular LB lattice discretization of a domain is shown on the left with a unit cell outlined. The middle image illustrates a D2Q4 velocity discretization and on the far right the D2Q9 scheme is shown [45].

It is necessary to define both the total energy, as well as the directional equilibrium energy. The total energy that appears in the LBKE is calculated by the sum of all directional non-equilibrium phonon energy propagations in the lattice

$$e(t,x) = \sum_{i=0}^{n} e_i(t,x) \tag{3.6}$$

where n is the number of discrete velocities per node subtracted by one, for instance, in the D2Q9 lattice, n = 8. The directional equilibrium phonon energy is defined as the weighted total equilibrium phonon energy

$$e_i^0(t,x) = w_i e(t,x)$$
$$\sum_{i=0}^{n} w_i = 1 \tag{3.7}$$

where w_i is the weighting coefficients. By introducing different weights it is possible to force phonons to scatter into preferred directions.

The simulation scheme flow chart of LBM is given in Fig. 3.2. We can calculate the phonon energy at any time. Through Debye model, we can get temperature from the phonon energy.

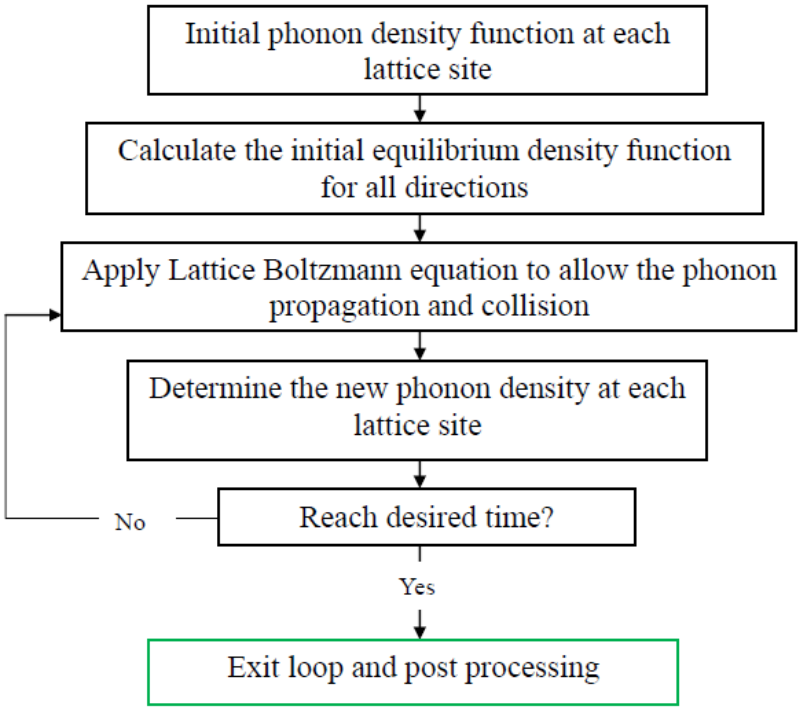

Figure 3.2. LBM simulation procedure flow chart [46].

3.1.3 Boundary condition

The application of accurate boundary conditions concerns most of the success of the lattice Boltzmann modeling. The complexities arise when specifying boundary conditions for the LB

models as the boundary nodes must capture the proper particle distribution functions that are often associated with a macroscopic quantity (i.e. temperature or surface heat flux). Since only one macroscopic quantity is known, several of the directional distribution functions can to be determined that then simulate accurate microscopic phenomena. This problem is illustrated with a D2Q9 lattice in Figure 3.3.

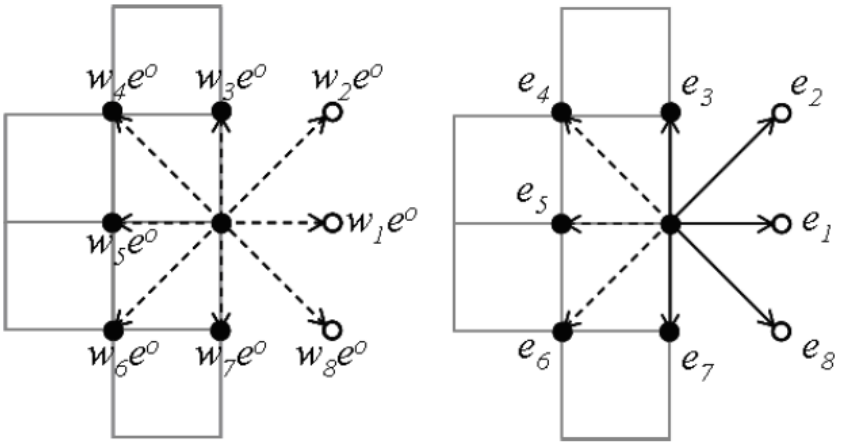

Figure 3.3. Dirichlet boundary (left) and a Neumann boundary (right) for the LB domain. The missing particle distribution functions (dashed arrows) in each case will be found from the application of the boundary condition. The other distribution functions (solid arrows) are found directly from the application of Eq. (3.5) [47].

It is possible for the LB method to properly handle both Dirichlet and Neumann boundary conditions. To specify a temperature at a boundary (Dirichlet type), the Debye model can used to calculate the corresponding phonon energy density [20]. The phonon energy density is then divided into the proper directional non-equilibrium phonon energies and held constant for all time as shown in the left one in Fig. 3.3. All directional distribution functions can be solved for knowing only the temperature at the boundary node, which are equal to equilibrium phonon energies. To apply a Neumann boundary condition, the heat flux vector across a node must first be defined as follows,

$$\boldsymbol{q} = \sum_{i=0}^{n} \boldsymbol{v}_i e_i(t, x) \tag{3.8}$$

where $\boldsymbol{v}_i$ is the phonon group velocity vector in the i lattice direction. To specify a value of the surface heat flux, the missing distribution functions in Figure 3.3 can be solved for through Eq. (3.8) and knowledge of the incoming heat flux vector; for an adiabatic boundary $\boldsymbol{q} \cdot \hat{n} = 0$. By definition, an adiabatic boundary results in the nonequilibrium phonons reflecting off the boundary. This process of reflecting phonons can occur in several ways; the mode of reflection is a function of the phonon wavelength, λ, and the surface roughness, σ. If the phonon wavelength is much smaller than the surface roughness ($\lambda >> \sigma$) then the phonons behave as if the boundary is perfectly smooth and reflection is specular in nature. In the contrary case ($\lambda << \sigma$), the impinging phonons will reflect diffusely. Intermediate cases can arise where $\lambda \approx \sigma$ in which case there is some fraction of phonons that is reflected specularly and another fraction reflected diffusely.

3.2 Implicit Lattice Boltzmann Method

Based on our best knowledge, only explicit LBM has been applied to solve the simplified BTE so far [43, 44, 47-49]. However, the explicit LBM for Eq. (2.13) is unconditionally unstable through stability analysis (which will be discussed later). In this work, we develop an implicit lattice Boltzmann method (ILBM) to solve the EG-BTE. Discretize Eq. (2.13) to obtain the lattice Boltzmann kinetic equation (LBKE),

$$\frac{e_i(t, \boldsymbol{r}) - e_i(t + \Delta t, \boldsymbol{r})}{\Delta t} + \boldsymbol{v}_i \frac{e_i(t + \Delta t, \boldsymbol{r} + \Delta \boldsymbol{r}_i) - e_i(t + \Delta t, \boldsymbol{r})}{\Delta r_i}$$

$$= \frac{e_i^0(t + \Delta t, \boldsymbol{r}) - e_i(t + \Delta t, \boldsymbol{r})}{\tau_R} - \tau_c \boldsymbol{v}_i \frac{e_i(t + \Delta t, \boldsymbol{r} + \Delta \boldsymbol{r}_i) - e_i(t + \Delta t, \boldsymbol{r}) - e_i(t, \boldsymbol{r} + \Delta \boldsymbol{r}_i) + e_i(t, \boldsymbol{r})}{\Delta t \Delta r_i} \tag{3.9}$$

where i is a direction subscript, and $\boldsymbol{v}_i$ is the phonon group velocity vector in the i lattice direction. The magnitude of group velocity in different direction is the same, i.e., $v_i = c$. For a D2Q4 lattice which is used in this study, the above equation can be written as

$$\begin{aligned}
A_1 e^{n+1}_{1,jk} - B e^{0,n+1}_{1,jk} + C_1 e^{n+1}_{1,j+1k} &= (1-D_1) e^{n}_{1,jk} + D_1 e^{n}_{1,j+1k} \\
A_1 e^{n+1}_{2,jk} - B e^{0,n+1}_{2,jk} + C_1 e^{n+1}_{2,j-1k} &= (1-D_1) e^{n}_{2,jk} + D_1 e^{n}_{2,j-1k} \\
A_2 e^{n+1}_{3,jk} - B e^{0,n+1}_{3,jk} + C_2 e^{n+1}_{3,j+1k} &= (1-D_2) e^{n}_{3,jk} + D_2 e^{n}_{3,j+1k} \\
A_2 e^{n+1}_{4,jk} - B e^{0,n+1}_{4,jk} + C_2 e^{n+1}_{4,j-1k} &= (1-D_2) e^{n}_{4,jk} + D_2 e^{n}_{4,j-1k}
\end{aligned} \tag{3.10}$$

where the parameter $A_1 = 1 + \frac{\Delta t}{\tau_R} - \frac{c\Delta t}{\Delta x} - \frac{c\tau_c}{\Delta x}$, $B = \frac{\Delta t}{\tau_R}$, $C_1 = \frac{c\Delta t}{\Delta x} + \frac{c\tau_c}{\Delta x}$, $D_1 = \frac{c\tau_c}{\Delta x}$, $A_2 = 1 + \frac{\Delta t}{\tau_R} - \frac{c\Delta t}{\Delta y} - \frac{c\tau_c}{\Delta y}$, $C_2 = \frac{c\Delta t}{\Delta y} + \frac{c\tau_c}{\Delta y}$, and $D_2 = \frac{c\tau_c}{\Delta y}$; the variable $e^{n}_{i,jk} = e_i(t, x, y)$, $e^{n+1}_{i,jk} = e_i(t+\Delta t, x, y)$, $e^{n}_{i,j+1k} = e_i(t, x+\Delta x, y)$, and $e^{n}_{i,jk+1} = e_i(t, x, y+\Delta y)$ represent discrete phonon energy density propagating along i direction respectively. The total phonon energy density is the sum of discrete phonon energy densities over all lattice directions

$$e^{n}_{jk} = e^{n}_{1,jk} + e^{n}_{2,jk} + e^{n}_{3jk} + e^{n}_{4,jk} \tag{3.11}$$

Under an isotropic assumption, the equilibrium phonon energy density is the same in each direction

$$e^{0,n}_{i,jk} = e^{n}_{jk} / 4, \qquad i = 1,2,3,4. \tag{3.12}$$

Since Eq. (3.10) is composed by a linear system of equations, it is solved iteratively by the Gauss-Seidel method. The ILBM simulation procedure is as follows:

(a). Initialize the phonon energy density at each lattice site.

(b). Determine the discrete equilibrium energy density at each lattice site using Eq. (3.12).

(c). Apply Eq. (3.10) to all lattice sites to allow phonon propagation and collision.

(d). Determine the new phonon energy density at each lattice site based Eq. (3.11).

(e). Repeat steps (b) to (d) until desired time is achieved.

Chapter 4

Validation of EG-BTE by Transient Thermal Grating and Time domain Thermo-reflectance Experiments

4.1 Transient Thermal Grating (TTG)

Measuring non-diffusive thermal transport at microscale in a configuration that can be quantitatively compared to theoretical models is a challenge for experimentalists. One difficulty is that any real interface between two materials involves thermal boundary resistance, which by itself presents a longstanding problem in nanoscale thermal transport. Johnson et. al. [12, 50] were the first one who present transient thermal grating (TTG) measurements of in-plane heat transport in freestanding silicon membranes without any interface.

In TTG method, two laser pulses are interfered in a sample with period L defined by the angle between the beams. Absorption of laser light leads to a spatially periodic temperature profile, and the decay of the temperature response is monitored via diffraction of a probe laser beam. The heat transport from grating peaks to nulls does not involve heat transfer across any interfaces and the distance scale is controlled by the period of the optical interference pattern. An additional advantage of the method is a spatially sinusoidal temperature profile facilitating theoretical analysis.

4.1.1 One-dimensional TTG

Measurements were conducted on 400 nm thick membranes with 400×400 μm^2 freestanding area. The membrane thickness was selected to be less than half of its optical penetration depth ~ 1 μm for pump wavelength 515 nm. Therefore the thermal transport in the cross-plane direction is negligible, and heat transport can be considered as one-dimensional (1D) with temperature and heat flux only in in-plane direction, parallel to the membrane surfaces. Data were collected at about 15 transient grating periods ranging from 2.4 μm to 25 μm in the two silicon membranes. Fig. 4.1 shows traces collected from membrane 1 with transient grating periods from 3.2 μm to 18 μm. As the grating period increases, the thermal decay becomes slower.

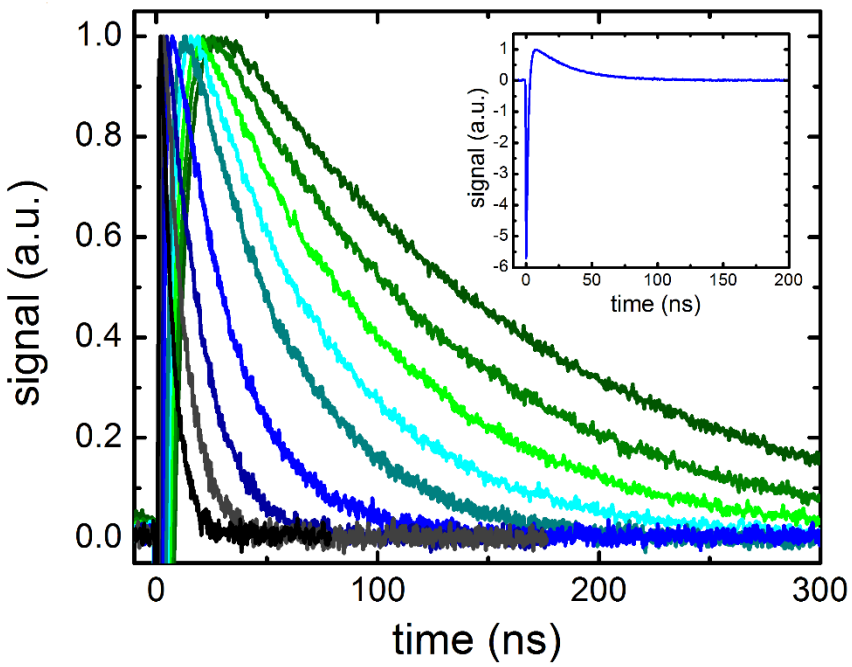

Figure 4.1. Experimentally measured thermal decay traces in a Si membrane from transient grating periods ranging from 3.2 to 18 m. The inset shows the complete trace for the 7.5 m period [50].

Theoretical treatment of thermal transport in TTG sample has been described in section 2.3. The temperature response in 1D TTG thermal transport is obtained in Eq. (2.42). There are only two independent parameters τ_c and τ_R in the temperature response. Before applying EG-BTE to analyse the thermal decay processes, we need to determine these two parameters that is described below.

The parameter τ_R is directly calculated by thermal properties of material, while the parameter τ_c is determined by curve fitting the experimental data. From the measurements, the thermal conductivity of 400nm-thick Si membrane is a constant ($\kappa_0 = 92$ W/mK) for grating period $L > 15$ μm. For $L < 10$ μm, the measured thermal conductivity of 400nm-thick Si membrane decreases with decreasing period L. The diffusive relaxation time can be calculated as $\tau_R = 3\kappa_0 / C_v v^2 = 4.06$ ps ($\kappa_0 = 92$ W/mK for 400nm-thick Si membrane, $C_v = 1.66\times10^6$ J/m^{3}K and sound speed $v = 6400$ m/s [51]). The corresponding diffusive mean free path (MFP) is obtained as $\Lambda_D = \tau_R v = 26$ nm. By fitting the experimental data of grating period $L = 3.2$ μm, we can determine the ballistic mean free time $\tau_c = 0.45$ ns. It is straightforward to obtain the ballistic MFP $\Lambda_B = \tau_c v = 2.88$ μm. The value of Λ_B is not the same as that determined in the two-parameter non-diffusive heat conduction model [31] because the assumption $\nabla f = \frac{df^0}{dT}\nabla T$ to derive Eq. (2.26) is an approximation not rigorous equivalent. The long ballistic MFP is consistent with the observed significant reduction in thermal conductivity as the grating period below about 5 μm.

After determining the two parameters in the enhanced Gray model, we can predicate thermal decay evolutions for any grating periods via Eq. (2.42). From Eq. (2.42), we obtain the thermal decay rate for grating period L as

$$\gamma = (\frac{2\pi}{L})^2 \frac{\kappa(\frac{2\pi}{L})}{C_v} \tag{4.1}$$

where the effective thermal conductivity is given in Eq. (2.39), i.e.,

$$\kappa(\frac{2\pi}{L}) = \frac{3\kappa_0}{Kn^2} \frac{1-\frac{\tan^{-1}(Kn)}{Kn}}{1-\frac{\tau_c}{\tau_R}(1-2Kn^2+(Kn^2-1)\frac{\tan^{-1}(Kn)}{Kn})} \tag{4.2}$$

where κ_0 = 92 W/mK, $Kn = \frac{2\pi}{L}\Lambda_D$, and $\Lambda_D = \tau_R v$ = 26 nm. In order to validate our numerical scheme, the normalized temperature response at the grating peaks is plotted in Fig. 4.2 obtained from the Eq. (2.42) and ILBM simulation. As expected, the ILBM results are exactly the same as the theoretical results for all grating periods (only five periods are plotted in Fig. 4.2).

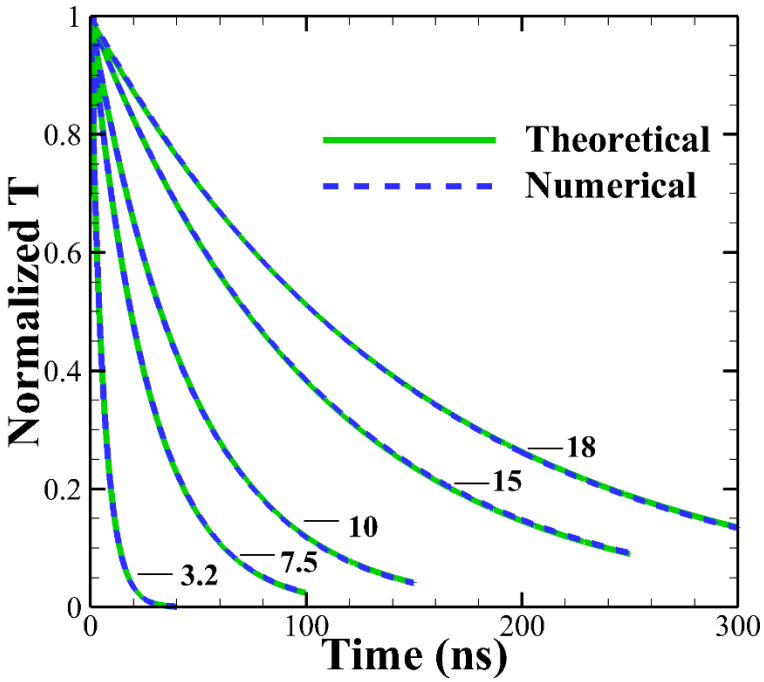

Fig. 4.2. The comparison of temperature responses obtained from theoretical solution Eq. (2.42) and ILBM simulation for grating periods L = 3.2, 7.5, 10, 15, and 18 μm.

Fig. 4.3 shows the comparison of theoretical thermal decay rates (a) and the effective thermal conductivities (b) with experimental data for different grating period. There is good agreement between theoretical predications and experiments. The thermal decay rate should vary linearly as $(2\pi/L)^2$ and the thermal conductivity should be independent of the grating period as long as the Fourier law is valid. However, we observed a remarkable deviation from diffusive thermal transport. The theoretical predications based on Gray BTE ($\tau_c = 0$) is also plotted together in Fig. 4.3(b) for comparison. It shows that the EG-BTE outperforms the Gray BTE results. From the comparison, there is remarkable nonlocal thermal transport over a distance of several microns due to long MFP phonons. The nonlocal effect can be characterized by EG-BTE.

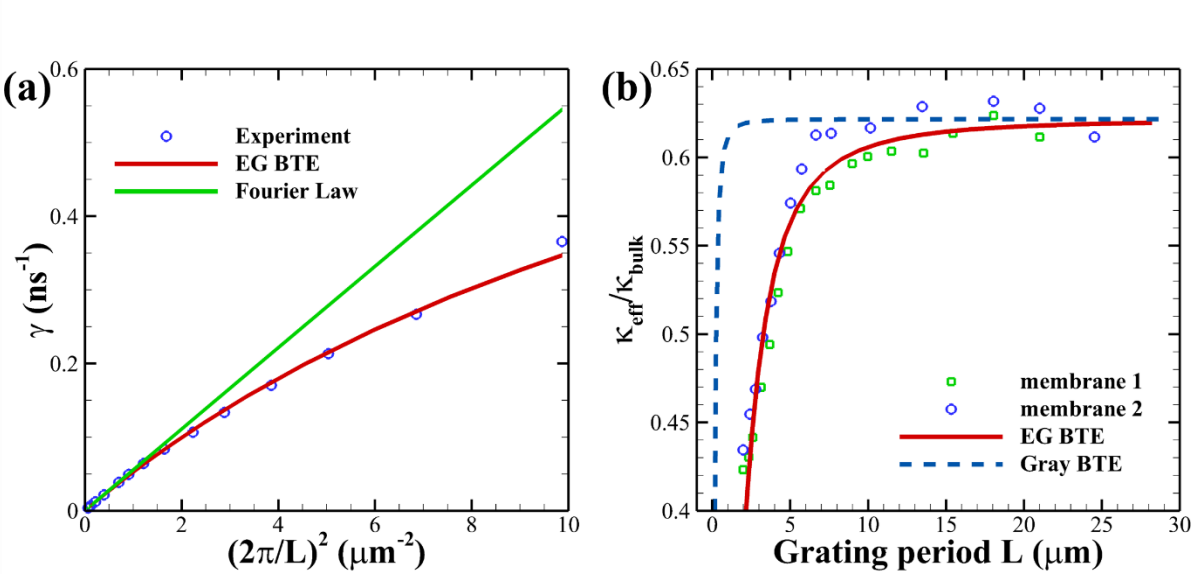

Figure 4.3. (a) Comparison of experimental thermal decay rates with theory. (b) Comparison of experimental effective thermal conductivity with theory.

We can reconstruct the signal decay traces based on thermal decay rates from Eq. (4.1) and electronic decay rates provided by Johnson et al. [50]. Again, good agreement is obtained between theoretical results and the experimental data for three representative grating periods as shown in Fig. 4.4.

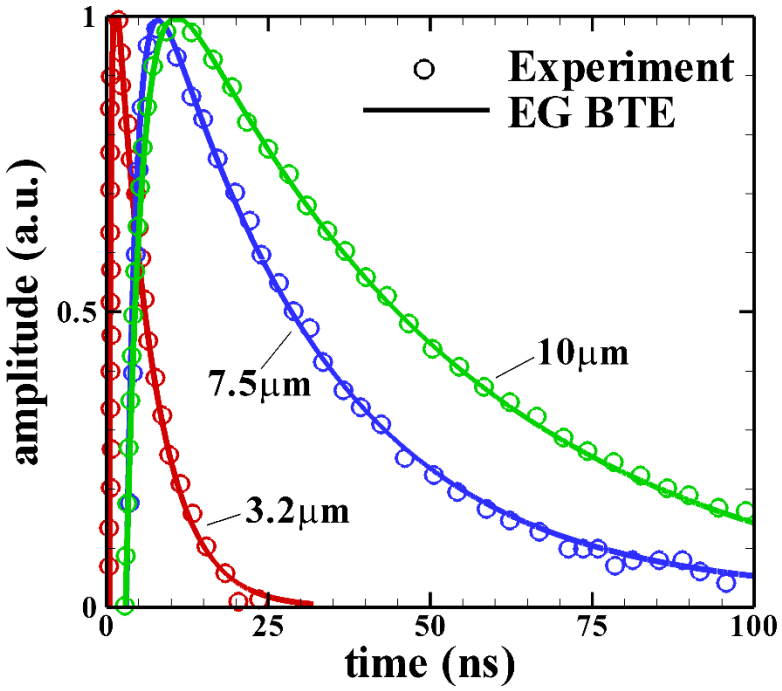

Figure 4.4. Comparison of predicted thermal decay traces by EG-BTE with experimental data for three grating periods [50].

The decrease in the effective thermal conductivity indicates the transition from diffusive to non-diffusive thermal transport due to low-frequency phonons. The good agreement shown in Fig. 4.3 and 4.4 demonstrates that the non-diffusive heat transfer in Si thin film can be described by EG-BTE. The nonlocal effects from low-frequency phonons can be characterized by a single parameter τ_c, the ballistic mean free time. Further experimental studies are necessary to prove τ_c is an inherent material property independent of probing methods.

4.1.2 Two-dimensional TTG

The two-dimensional (2D) TTG thermal transport is much more complicated than 1D situation due to an exponential decay heating in the cross-plane direction. The thermal decay is no longer a pure exponential as in a 1D domain.

Theoretical treatment of thermal transport in TTG sample has been described in section 2.3. The probe signal response at the peaks in 2D TTG thermal transport is obtained from Eq. (2.49),

$$H(\mathrm{t}) = A\int_0^{\infty} \frac{\exp[-\alpha(\xi)\xi^2 t]}{(\beta_1^2+\xi_y^2)(\beta_2^2+\xi_y^2)}\, d\xi_y \tag{4.3}$$

where A is an arbitrary constant, $\alpha(\xi) = \kappa(\xi)/C_v$ is the apparent thermal diffusivity, and the total spatial frequency is $\xi = \sqrt{(2\pi/L)^2 + \xi_y^2}$. The probe signal $H(\mathrm{t})$ is a multiexponential decay with the relative contribution weighted by the Fourier transform of the cross-plane heating profile. To further validate our numerical scheme, the normalized temperature response of 2D TTG obtained from the Eq. (2.45) and ILBM simulation. As expected, the ILBM results are exactly the same as the theoretical predications for grating periods.

Computing the apparent thermal diffusivities versus spatial frequency by Eq. (2.46) and inserting them into Eq. (4.3), the reconstructed transient decay traces are obtained in Fig. 4.5. The thermal properties of bulk GaAs at room temperature are specified as κ_{bulk} = 45 W/mK, C_v = 1.75×10^6 J/m^{3}K, sound speed v = 3700 m/s, and the diffusive mean free time τ_R = 5.6 ps. By fitting the experimental data of grating period L = 2.4 μm, we can determine the ballistic mean free time τ_c = 1.57 ns, the ballistic MFP $\Lambda_B = \tau_c v$ = 5.8 μm, and the absorption coefficients in the cross-plane direction $\beta_1 = \beta_2$ = 1/110 nm^{-1}. As shown in Fig. 4.5, the reconstructed thermal decays of GaAs

and the measured signal traces agree well with each other for grating periods ranging from 2.4 to 4.9 μm. Therefore, the validity of EG-BTE is demonstrated by 1D and 2D TTG experiments.

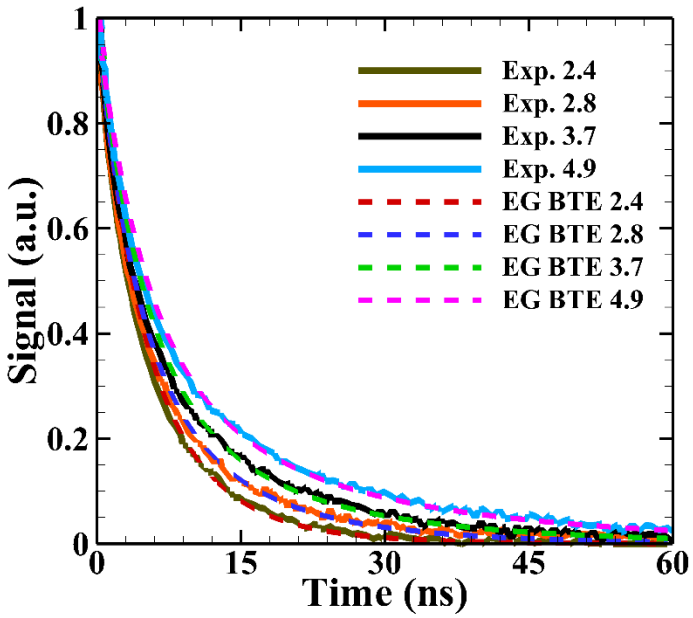

Figure 4.5. Comparison of reconstructed thermal decays by EG-BTE with the original experimental measured data of GaAs for grating periods 2.4, 2.8, 3.7, and 4.9 μm.

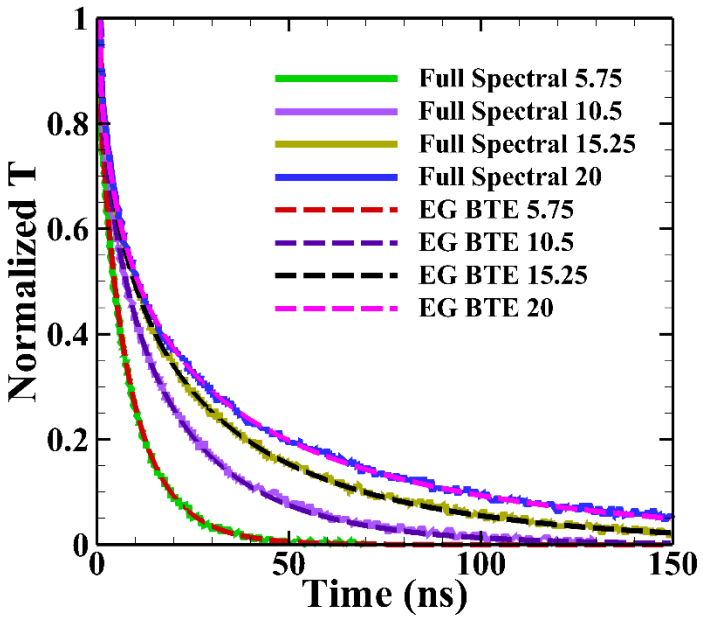

Figure 4.6. Comparison of calculated thermal decays of Si by EG-BTE with those by full spectral BTE for grating periods 5.75, 10.5, 15.25, and 20 μm [52].

We did not find experimental data reported for bulk Si in this case. Here we compare our predictions with those from full spectral BTE with input from first principle calculations by Minnich [52]. The diffusive mean free time is calculated by $\tau_R = 3\kappa_{bulk} / C_v v^2 = 6.53$ ps ($\kappa_{bulk} = 148$ W/mK for bulk Si at room temperature). By fitting the Minnich's result of grating period $L = 5.75$ μm, we can determine the ballistic mean free time $\tau_c = 0.718$ ns, the ballistic MFP $\Lambda_B = \tau_c v$, i.e., 4.6 μm, and the absorption coefficients in the cross-plane direction $\beta_1 = \beta_2 = 1/560$ nm^{-1}. The ballistic MFP Λ_B obtained in 1D TTG is smaller than that in 2D TTG because the phonon ballistic transport is restricted by boundary scatterings.

As shown in Fig. 4.6, the present reconstructed thermal decays and the full spectral BTE results agree well with each other for grating periods ranging from 5 to 20 μm. It should be noted

that Minnich [52] calculated these results by using suppression function in thermal conductivity. The suppression function assumes that phonons with MFPs longer than the thermal length scale do not contribute to the thermal conductivity. However, phonon dispersion is included in their theory which makes the calculations considerably complicated.

4.2. Time domain Thermo-reflectance (TDTR)

Deviations between experimental data and Fourier predications have been reported in many literatures. Except the TTG we discussed in previous section, a pump beam size dependence of thermal conductivity in Si using time domain thermo-reflectance (TDTR) was reported by Minnich et al. [10, 33]. The major difference with TTG is that there is thermal transport across interface in TDTR. To perform the experiment, a high-purity natural Si wafer was coated with 70 nm of Al. A pump beam heats the thin metal transducer film. A time delayed probe beam measures the change in reflectance due to the temperature increase induced by the pump beam.

4.2.1 Theoretical solution

Thermal properties including the Al/Si interface conductance G and the Si thermal conductivity κ are extracted by fitting the experimental data based on a thermal model. If the Fourier law is applied, it can be solved in a 2D cylindrical coordinate. However, it must be solved in the 3D geometry if using the BTE. Solving the transient BTE in this 3D domain is computationally expensive using numerical approach due to its large spatial extent. Here we present a theoretical solution of the heat conduction in the full 3D geometry of a TDTR experiment including an interface using the EG-BTE.

For the metal film, we adopt the Fourier law to describe the heat transport which is

$$C_{vf}\frac{\partial T_f}{\partial t}=\kappa_f\left(\frac{\partial^2 T_f}{\partial x^2}+\frac{\partial^2 T_f}{\partial y^2}+\frac{\partial^2 T_f}{\partial z^2}\right) \tag{4.4}$$

where C_{vf} is the volumetric heat capacity, κ_f the thermal conductivity, T_f the temperature of metal film, x and y the radial coordinates, and z the cross-plane coordinate. Taking a Fourier transform in time and space leads to

$$\frac{\partial^2 \tilde{T}_f}{\partial z^2}=\varepsilon_f^2\tilde{T}_f \tag{4.5}$$

where $\tilde{T}_f=\iiint T(t,x,y,z)e^{-i\eta t-i\xi_x x-i\xi_y y}dtdxdy$, $\varepsilon_f^2=\xi^2+\frac{i\eta C_{vf}}{\kappa_f}$, $\xi=\sqrt{\xi_x^2+\xi_y^2}$, η, ξ_x and ξ_y are the Fourier variables in temporal and spatial domains. From Eq. (4.5), the temperature $\tilde{T}_{ft}$, and heat flux $\tilde{q}_{ft}$ on the top side of the metal film are related to the temperature $\tilde{T}_{fb}$, and heat flux $\tilde{q}_{fb}$ on the bottom side through [53]

$$\begin{bmatrix}\tilde{T}_{fb}\\ \tilde{q}_{fb}\end{bmatrix}=\begin{bmatrix}\cosh(\varepsilon_f d) & \frac{-1}{\kappa_f\varepsilon_f}\sinh(\varepsilon_f d)\\ -\kappa_f\varepsilon_f\sinh(\varepsilon_f d) & \cosh(\varepsilon_f d)\end{bmatrix}\begin{bmatrix}\tilde{T}_{ft}\\ \tilde{q}_{ft}\end{bmatrix} \tag{4.6}$$

where d is the metal film thickness. Multiple layers are treated by multiplying the matrices for individual layers together,

$$\begin{bmatrix}\tilde{T}_{nb}\\ \tilde{q}_{nb}\end{bmatrix}=M_n M_{n-1}\cdots M_1=\begin{bmatrix}A & B\\ C & D\end{bmatrix}\begin{bmatrix}\tilde{T}_{1t}\\ \tilde{q}_{1t}\end{bmatrix} \tag{4.7}$$

where M_n is the matrix for the n-th layer. An interface can be handled by taking the limit as the d approaches zero,

$$\begin{bmatrix}\tilde{T}_{st}\\ \tilde{q}_{st}\end{bmatrix}=\begin{bmatrix}1 & -\frac{1}{G}\\ 0 & 1\end{bmatrix}\begin{bmatrix}\tilde{T}_{fb}\\ \tilde{q}_{fb}\end{bmatrix} \tag{4.8}$$

where G is the interface conductance, $\tilde{T}_{st}$ the temperature, and $\tilde{q}_{st}$ heat flux on the top side of the Si substrate. The thermal transport in Si substrate is governed by the EG-BTE, Eq. (2.13). Taking a Fourier transform of it gives

$$\tilde{e} = \frac{\tilde{e}_0 - (1+i\eta\tau_c)\Lambda_D \cos\theta \frac{\partial \tilde{e}}{\partial z}}{1+i\eta\tau_R + (i-\eta\tau_c)\Lambda_D(\xi_x \sin\theta\cos\varphi + \xi_y \sin\theta\sin\varphi)} \tag{4.9}$$

where $\tilde{e} = \iiint e(t,x,y,z,\theta,\varphi)e^{-i\eta t - i\xi_x x - i\xi_y y}dtdxdy$, $\Lambda_D = v\tau_R$, η, ξ_x and ξ_y are the Fourier variables in temporal and spatial domains, (θ, φ) is the direction of the group velocity vector within a unit solid angle. Taking the approximation $\frac{\partial \tilde{e}}{\partial z} = \frac{\partial}{\partial z}(\tilde{e}_0 - v\tau_R \cos\theta \frac{\partial \tilde{e}_0}{\partial z})$ [20], and substituting Eq. (4.9) into Eq. (2.29) gives,

$$\frac{\partial^2 \tilde{e}_0}{\partial z^2} = \frac{1-\mathcal{A}(\eta,\xi)}{\mathcal{B}(\eta,\xi)\Lambda_D^2}\tilde{e}_0 \tag{4.10}$$

$$\mathcal{B}(\eta,\xi) = [1+(\frac{1+i\eta\tau_R}{(1+i\eta\tau_c)Kn})^2]\mathcal{A}(\eta,\xi) - \frac{1+i\eta\tau_R}{(1+i\eta\tau_c)^2 Kn^2} \tag{4.11}$$

where $\mathcal{A}(\eta,\xi)$ is given in Eq. (2.44), and $\xi = \sqrt{\xi_x^2 + \xi_y^2}$. Since e and e_0 are defined as deviations from the background reference energy corresponding to thermal equilibrium at the temperature T_0, the equilibrium energy e_0 is proportional to the temperature change in the small perturbation limit as $e_0 = \frac{1}{4\pi}C_v(T-T_0)$. The temperature T_s of the Si substrate is then obtained from Eq. (4.10),

$$\frac{\partial^2 \tilde{T}_s}{\partial z^2} = \frac{1-\mathcal{A}(\eta,\xi)}{\mathcal{B}(\eta,\xi)\Lambda_D^2}\tilde{T}_s \tag{4.12}$$

From the above equation, the temperature $\tilde{T}_s(z)$, and heat flux $\tilde{q}_s(z)$ at a location *z* of the Si substrate are related to the temperature $\tilde{T}_{st}$, and heat flux $\tilde{q}_{st}$ on the top side through

$$\begin{bmatrix} \tilde{T}_s(z) \\ \tilde{q}_s(z) \end{bmatrix} = \begin{bmatrix} \cosh(\varepsilon_s z) & \frac{-1}{\kappa_s \varepsilon_s}\sinh(\varepsilon_s z) \\ -\kappa_s \varepsilon_s \sinh(\varepsilon_s z) & \cosh(\varepsilon_s z) \end{bmatrix} \begin{bmatrix} \tilde{T}_{st} \\ \tilde{q}_{st} \end{bmatrix} \tag{4.13}$$

where κ_s is the thermal conductivity of the Si substrate, and $\varepsilon_s^2 = \frac{1-\mathcal{A}(\eta,\xi)}{\mathcal{B}(\eta,\xi)\Lambda_D^2}$. Since the Si substrate is treated as semi-infinite, the heat flux is zero when *z* approaches infinity. Eq. (4.7) reduces to $C\tilde{T}_{ft} + D\tilde{q}_{ft} = 0$ and the surface temperature of metal film is given by

$$\tilde{T}_{ft} = -\frac{D}{C}\tilde{q}_{ft} \tag{4.14}$$

$$-\frac{D}{C} = \frac{1+\kappa_s\varepsilon_s\left(\frac{\tanh(\varepsilon_f d)}{\kappa_f\varepsilon_f}+\frac{1}{G}\right)}{\kappa_f\varepsilon_f\tanh(\varepsilon_f d)+\kappa_s\varepsilon_s\left(\frac{\tanh(\varepsilon_f d)}{G}+1\right)} \tag{4.15}$$

where $\tilde{q}_{ft} = \frac{A_0}{2\pi}\exp\left(\frac{-\xi^2 r_0^2}{8}\right)$ is the heat flux of pump beam with power A_0 and $1/e^2$ radius r_0 applied to the top surface of metal film. The $1/e^2$ radius is defined as the radius at which the intensity of the pump beam falls to $1/e^2$ of its peak value. The frequency response of probe signal *H* in real space is obtained by taking the inverse Hankel transform and then weighing the result by the probe intensity distribution,

$$H(\eta) = \frac{A_0}{2\pi}\int_0^\infty \frac{-D}{C}\exp\left(\frac{-\xi^2(r_0^2+r_1^2)}{8}\right)\xi d\xi \tag{4.16}$$

where r_1 is probe $1/e^2$ radius. The output of the lock-in amplifier will be a complex number Z(η) of the probe signal with respect to the reference wave at every delay time τ given by

$$Z(\eta_0) = A\sum_{k=-\infty}^{\infty} H(\eta_0 + k\eta_s)e^{ik\eta_s\tau} \tag{4.17}$$

where η_0 is the reference frequency, η_s is the sampling frequency, and *A* is an arbitrary constant. The experimental amplitude and phase signals are

$$R = \sqrt{X^2 + Y^2} \tag{4.18}$$

$$\Phi = \tan^{-1}(\mathrm{Y}/\mathrm{X}) \tag{4.19}$$

where X and Y are real and imaginary part of $Z(\eta_0)$.

4.2.2 Results

The sample is fabricated by a high-purity Si substrate coated with 70 nm Al transducer film. The pump diameters include D = 3.65, 5.44, 8.9, 12, 15, 30, 45, and 60 μm. The probe diameter is kept constant at 2.7 μm for pump diameters less than 15 μm and 9.5 μm otherwise. Two representative experimental amplitude and phase angle are shown in Fig. 4.7 for pump diameters D = 30 and 3.65 μm. The parameters used in EG-BTE are the same as those used in 2D TTG experiment which are given in section 4.1.2. The thermal conductivity of Si substrate is kept constant as bulk value κ_s = 148 W/mK in EG-BTE, while in Fourier law, the effective thermal conductivities are obtained by fitting the experimental curves. For large pump diameter 30 μm, both EG-BTE (*G* = 210 MW/m^{2}K) and Fourier law (*G* = 240 MW/m^{2}K) are in good match with experimental data shown in Fig. 4.7(a) and (b). The extracted thermal conductivity of Si substrate is 148 W/mK, which confirms that the diffusive thermal transport is dominated in this regime. As the heater region becomes smaller, non-diffusive heat transfer grows remarkable. For pump diameter 3.65 μm as shown in Fig. 4.7(c) and (d), Fourier law (*G* = 205 MW/m^{2}K) cannot fit both amplitude and phase angle simultaneously, and the effective thermal conductivity is 110 W/mK

which is significant less than the bulk value. However, in this nondiffuisve regime, EG-BTE can fit both amplitude and phase angle very well (G = 180 MW/m^{2}K). The extracted thermal interface conductance G between Al and Si decreases a little bit from 210 to 180 MW/m^{2}K in EG-BTE, or from 240 to 205 MW/m^{2}K in Fourier law when the pump diameters change from 60 to 3.65 μm.

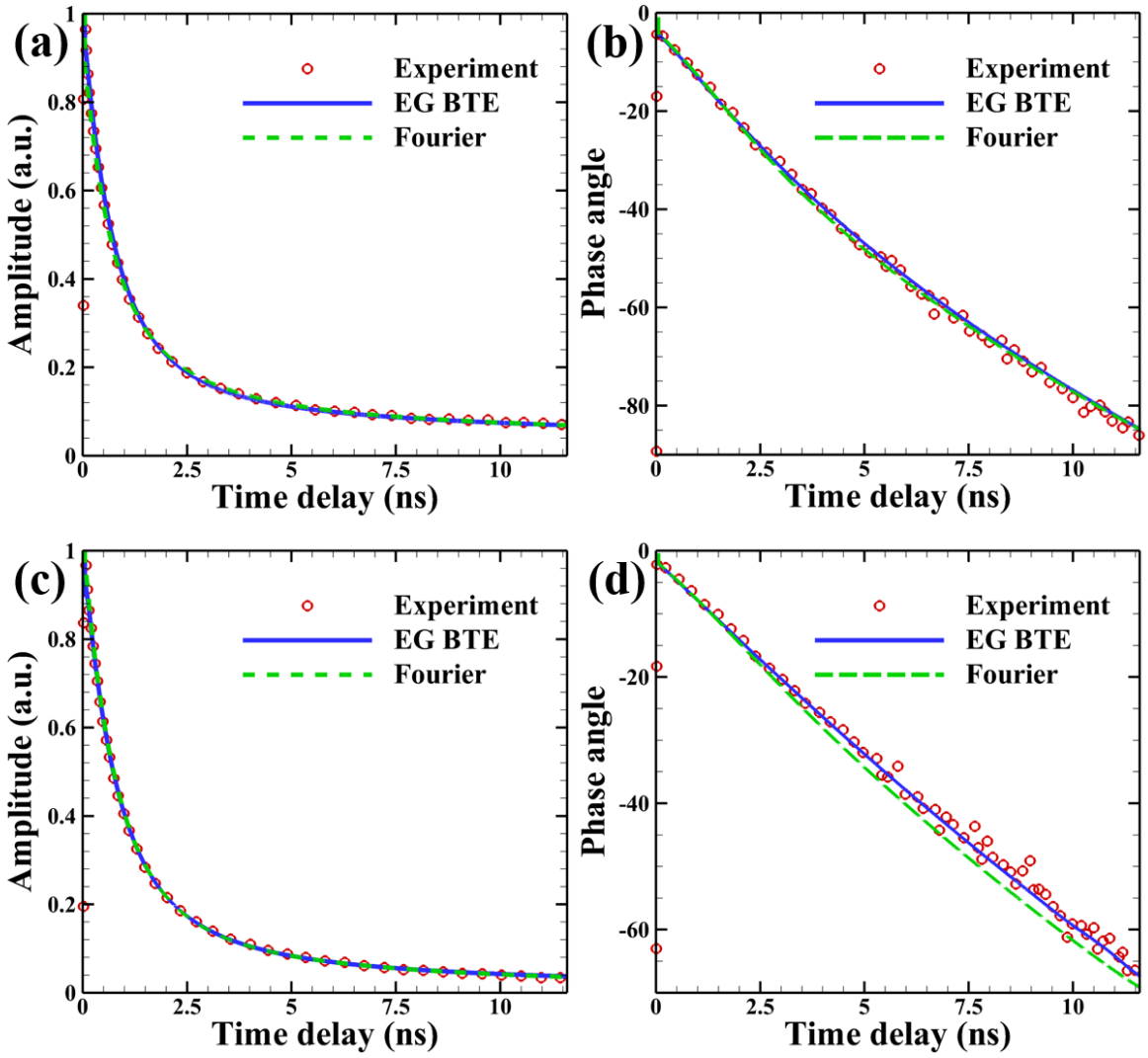

Figure 4.7. Comparison of analytical solutions based on EG-BTE and Fourier law with experimental data. (a) and (b) are amplitude and phase angle for pump diameter 30 μm. (c) and (d) are amplitude and phase angle for pump diameter 3.65 μm.

An important note about numerical errors should be mentioned. There are mainly two types of errors associated with this type of calculations of signal values (e.g. amplitude and phase angle), namely, approximation errors and round-off errors. Despite these unavoidable errors, the results obtained in the analysis studied here and on other cases studied in Ch. 5 and Ch. 6 are consistently showing similar behavior with experimental data.

Chapter 5

Non-diffusive Thermal Transport in Thin Film and Cryogenic Crystal

5.1 Non-diffusive Heat Conduction in Thin Film

Thermal transport in micro/nano structures is significantly different than in bulk materials due to phonon boundary scatterings. The reduced thermal conductivity of thin films limits their ability to remove waste heat effectively which may cause low efficiency and affect the reliability. One of the classic size effect problems is the thickness dependence of thermal conductivity of thin films, which has been extensively studied. Traditional theory estimates the phonon mean free path (MFP) for Si around 41.8 nm at room temperature (RT), one would not expect remarkable size effect on the micron length scale. However, recent first-principles calculations indicated that phonons with MFP exceeding 1 μm contribute almost 40% to the Si thermal conductivity at RT. In fact, the transient grating experiments on Si and GaAs observed a significant reduction of thermal conductivity over several microns size.

Approaches at different levels have been proposed to predict the thermal conductivity in thin films. Holland [54], Flik [55], and McGauhey [56-58] developed models based on BTE which required accurate phonon properties as input. Lattice dynamics calculation [59], Monte Carlo method [60] and molecular dynamics (MD) simulation [61] have also been used to elucidate the

phonon transport physics. The latter two methods are daunting computationally expensive and challenging to implement. A general satisfactory theory to give a predication agreed with existing experiments is not available yet.

5.1.1 In-plane thermal transport in thin films

In this thesis, we present strict analysis for predicting the in-plane phonon transport of thin films based on Boltzmann transport equation.

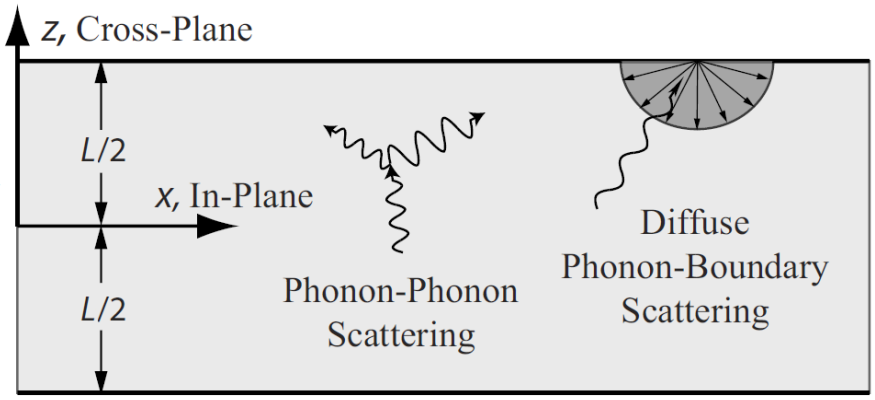

Figure 5.1. Schematic diagram of the thin film [57]. The film is infinite in x direction.

Consider a film of thickness L and suppose that the z-axis is perpendicular to the plane of the film as shown in Fig. 5.1. We begin with the BTE under steady-state condition and assume isotropic phonon properties,

$$\boldsymbol{v}\cdot\nabla e=-\frac{e-e^{0}}{\tau_t} \tag{5.1}$$

where the relaxation time τ_t is the harmonic average of phonon-phonon scattering τ_R and phonon-boundary scattering τ_b using Matthiessen rule

$$\tau_t^{-1}=\tau_R^{-1}+\tau_b^{-1} \tag{5.2}$$

The average distance travelled by a phonon before hitting the top or bottom surface is

$$\frac{1}{L}\int_{-L/2}^{L/2}\left|\frac{L/2-z}{\cos\theta}\right|dz=\frac{L}{2\left|\cos\theta\right|} \tag{5.3}$$

The boundary scattering lifetime is obtained as $\tau_b^{-1}=\frac{L}{2v_g\left|\cos\theta\right|}$, therefore the total phonon relaxation time is

$$\tau_t=\frac{\tau_R}{1+2Kn\left|\cos\theta\right|} \tag{5.4}$$

where Knudsen number $Kn=\frac{v_g\tau_R}{L}$. Employ the Fourier transform in x-direction of Eq. (5.1)

$$iv_g\xi_x\sin\theta\cos\varphi\tilde{e}+v_g\cos\theta\frac{\partial\tilde{e}}{\partial z}=-\frac{\tilde{e}-\tilde{e}_0}{\tau_t} \tag{5.5}$$

The general solution of Eq. (5.5) is

$$\tilde{e}=A\exp(-\frac{z\varepsilon}{v_g\tau_t\cos\theta})+\frac{\tilde{e}_0}{\varepsilon} \tag{5.6}$$

where A is an arbitrary constant and $\varepsilon=1+iv_g\tau_t\xi_x\sin\theta\cos\varphi$. Traditionally, one would assume that phonons are either specularly reflected or diffusive reflection. Here we assume the phonon boundary condition is absorption,

$$\tilde{e}(\pm\frac{L}{2},\theta)=0 \tag{5.7}$$

Under steady state, once the phonons reach the boundary they would not reflected back to the media, instead they would travel any direction on the surface. Applying the boundary condition to Eq. (5.6), we obtained

$$\tilde{e} = -\frac{\tilde{e}_0}{\varepsilon}\exp(-\frac{(z+L/2)\varepsilon}{v_g\tau_t\cos\theta}) + \frac{\tilde{e}_0}{\varepsilon}, \qquad \theta \in [0, \frac{\pi}{2}) \tag{5.8}$$

$$\tilde{e} = -\frac{\tilde{e}_0}{\varepsilon}\exp(-\frac{(z-L/2)\varepsilon}{v_g\tau_t\cos\theta}) + \frac{\tilde{e}_0}{\varepsilon}, \qquad \theta \in (\frac{\pi}{2}, \pi] \tag{5.9}$$

The heat flux in x-direction can be calculated as follows:

$$\begin{aligned}\tilde{q}_x(z) = &\frac{1}{4\pi}\int_0^{2\pi}\int_0^{\pi/2}[1-\exp(-\frac{(z+L/2)\varepsilon}{v_g\tau_t\cos\theta})]\frac{\tilde{e}_0}{\varepsilon}v_{g,x}\sin\theta d\theta d\varphi \\ &+\frac{1}{4\pi}\int_0^{2\pi}\int_{\pi/2}^{\pi}[1-\exp(-\frac{(z-L/2)\varepsilon}{v_g\tau_t\cos\theta})]\frac{\tilde{e}_0}{\varepsilon}v_{g,x}\sin\theta d\theta d\varphi\end{aligned} \tag{5.10}$$

where $v_{g,x} = v_g\sin\theta\cos\varphi$. The above equation gives the heat flux distribution across the thickness of the film. Average the heat flux from –L/2 to L/2,

$$\tilde{q}_x = \frac{1}{L}\int_{-L/2}^{L/2}\tilde{q}_x(z)dz = \frac{\tilde{e}_0}{4\pi}\int_0^{2\pi}\int_0^{\pi/2}[\frac{1}{\varepsilon} - 2\frac{1-\exp(-\delta)}{\varepsilon\delta}]v_{g,x}\sin\theta d\theta d\varphi \tag{5.11}$$

where $\delta = \dfrac{L\varepsilon}{v_g\tau_t\cos\theta}$. The apparent overall thermal conductivity of the film is obtained by averaging the heat flux and then over the temperature gradient. Since $q_x = -\kappa_{eff}\,\partial T/\partial x$, taking the Fourier transform gives,

$$\tilde{q}_x = -\kappa_{eff} i\xi_x\tilde{T} = -\kappa_{eff} i\xi_x\frac{\tilde{e}_0}{C_v} \tag{5.12}$$

As we know the in-plane temperature profile is infinite, we may assume the spatial period is much larger than the MFP $v_g\tau_t$, i.e, $v_g\tau_t\xi_x \ll 1$. The Eq. (5.11) can be simplified by expanding around $v_g\tau_t\xi_x = 0$, and keeping only the first order terms, and the effective thermal conductivity is obtained,

$$\frac{\kappa_{eff}}{\kappa_{bulk}} = \frac{3}{2}\int_0^1 [1 - \frac{2Kn\mu}{1+2Kn\mu}(1-\exp(-\frac{1+2Kn\mu}{Kn\mu})) + \exp(-\frac{1+2Kn\mu}{Kn\mu})]\frac{1-\mu^2}{1+2Kn\mu}d\mu \quad (5.13)$$

where $\mu = \cos\theta$.

It should be noted that Sondheimer [62] derived a similar expression for κ_{eff} using pure diffusive boundary condition $e(\pm\frac{L}{2},\theta) = e_0$,

$$\frac{\kappa_{eff}}{\kappa_{bulk}} = \frac{3}{2}\int_0^1 [1 - Kn\mu(1-\exp(-\frac{1}{Kn\mu}))](1-\mu^2)d\mu \quad (5.14)$$

By considering the boundary scattering, the above equation is altered as

$$\frac{\kappa_{eff}}{\kappa_{bulk}} = \frac{3}{2}\int_0^1 [1 - \frac{Kn\mu}{1+2Kn\mu}(1-\exp(-\frac{1+2Kn\mu}{Kn\mu}))]\frac{1-\mu^2}{1+2Kn\mu}d\mu \quad (5.15)$$

The heat flux profile along z-axis is also obtained as

$$\begin{aligned} q_x(z) = &\frac{1}{4\pi}\int_0^{2\pi}\int_0^{\pi/2}[1-\exp(-\frac{z+L/2}{v_g\tau_t\cos\theta})]\frac{\partial e_0}{\partial x}\tau_t v_{g,x}^2\sin\theta d\theta d\varphi \\ &+\frac{1}{4\pi}\int_0^{2\pi}\int_{\pi/2}^{\pi}[1-\exp(-\frac{z-L/2}{v_g\tau_t\cos\theta})]\frac{\partial e_0}{\partial x}\tau_t v_{g,x}^2\sin\theta d\theta d\varphi \end{aligned} \quad (5.16)$$

The Eq. (5.16) is heat flux profile obtained by Sondheimer. Under the absorption boundary condition in Eq. (5.7), the heat flux is calculated by Eq. (5.10) which is simplified by expanding around $v_g\tau_t\xi_x = 0$, and keeping only the first order terms,

$$\begin{aligned} \tilde{q}_x(z) = &\frac{i\xi_x\tilde{e}_0}{4\pi}[\int_0^{2\pi}\int_0^{\pi/2}\exp(-\sigma^+)[1+\sigma^+-\exp(\sigma^+)]\tau_t v_{g,x}^2\sin\theta d\theta d\varphi \\ &+\int_0^{2\pi}\int_{\pi/2}^{\pi}\exp(-\sigma^-)[1+\sigma^--\exp(\sigma^-)]\tau_t v_{g,x}^2\sin\theta d\theta d\varphi] \end{aligned} \quad (5.17)$$

where $\sigma^{\pm} = \frac{z\pm L/2}{v_g\tau_t\cos\theta}$. After normalization, the local heat flux profiles obtained by Eq. (5.16) and Eq. (5.17) are presented in Fig. 5.2 for Kn from 0.001 to 5.

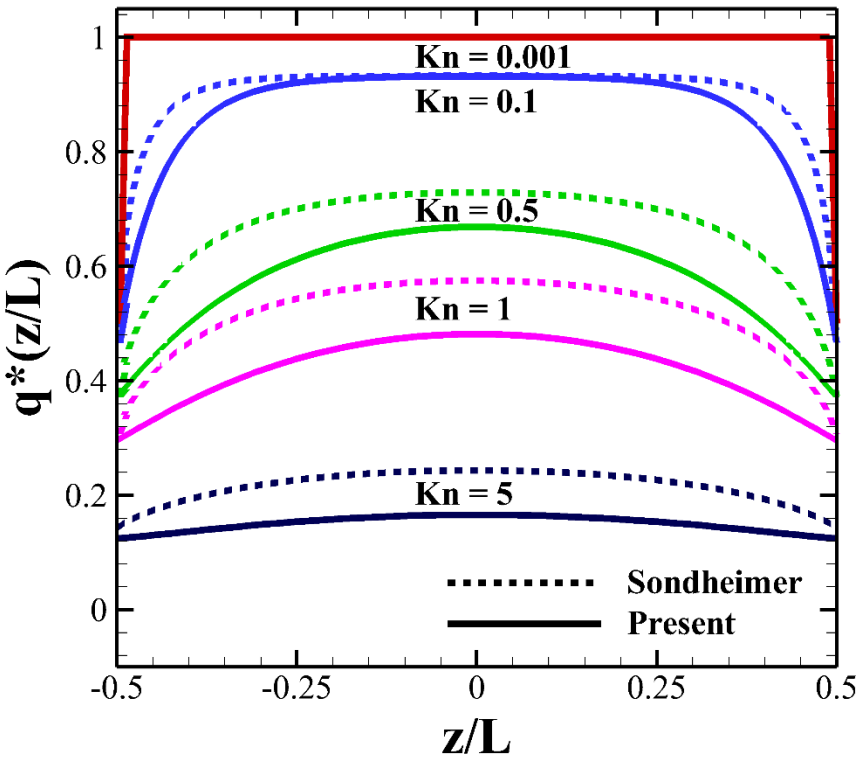

Figure 5.2. Normalized local heat flux profiles for Kn from 0.001 to 5.

The local heat flux at the boundary is only half of the bulk value, and the heat flux profiles are flat in the center when the Knudsen number is small (Kn < ~ 0.1). However, the local heat flux profiles decreases further as the Kn increasing which are leaded by that the boundary scattering effects originating from the two surfaces start to overlap with each other. For the same Kn, the heat flux calculated by present approach is smaller than that by Sondheimer which means the effective thermal conductivity is smaller.

To validate the theoretical predication, the analytical solution in Eq. (5.13) is plotted against available experimental data on in-plane thermal conductivity of silicon thin films as shown in Fig. 5.3. The present model captures the trend of thermal conductivity measured by different

experiments. The analytical predications are generally higher than the experimental data. The results may be due to the gray approximation which tends to underpredict the lifetime of the majority of the phonons. Theoretical predictions from Majumdar [19] and Sondheimer in Eq. (5.15) are also plotted for comparison. Without considering the phonon-boundary scattering, the prediction from Majumdar is much larger than the experimental data and the other predictions. However, the Sondheimer's model also overpredicts the thermal conductivity than present model because the diffusive reflection boundary condition is used while absorption boundary is used in present model. Overall, the present prediction gives a better agreement with experiments than the other two results.

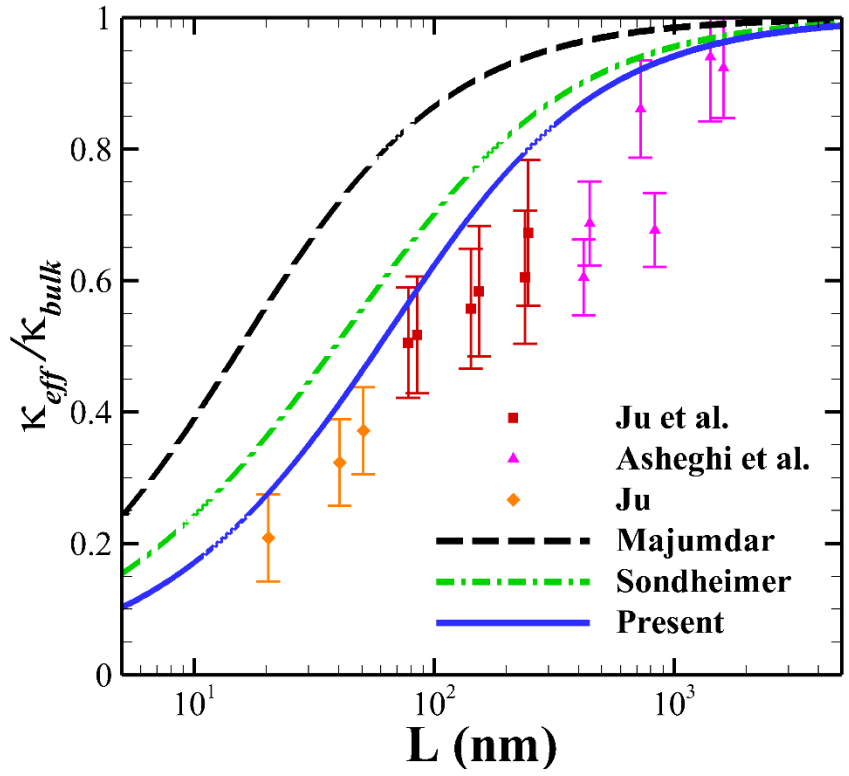

Figure 5.3. Comparison of thermal conductivity obtained by models and experiments for in-plane silicon thin films at 300 K. Experimental data (Ju [63], Asheghi [64], Ju [65]) are shown by

symbols. Reference [65] did not report the error bar, but we added its error bar with comparable uncertainty as other experiments.

5.1.2 Cross-plane thermal transport in thin films

In the previous section, we have presented a strict approach to predict in-plane thermal conductivity in thin films. In this section, the cross-plane thermal conductivity will be studied. Since the insulated boundary conditions are applied on the top and bottom surface, we may extend the computational domain periodically along the cross-plane direction with period L. Employing Fourier transform in the cross-plane direction and following the procedure described in section 4.1.1, we would end up the same effective thermal conductivity in Eq. (2.39) based on transient EG-BTE. The assumptions used to derive Eq. (2.39) are satisfied since the time scale interested can be very large so that $\eta\tau_R \ll 1$ and $\eta\tau_c Kn \ll 1$.

The effective thermal conductivity derived by transient Gray BTE is different from that by transient EG-BTE. However, if we calculate the effective thermal conductivity under steady state condition, it should be the same. Here we apply LBM to calculate the effective thermal conductivity under steady state condition. Consider a thin film with thickness L, and fixed temperature boundary conditions are imposed on two surfaces. The energy density (temperature) profiles under steady-state situation for different Kn are shown in Fig. 5.4. The Gray BTE and EG-BTE predict the same temperature profiles under steady-state condition. For small Knudsen number (~ 0.01), there is no energy jump at the boundaries and the energy decreases linearly as predicted by the Fourier law. For large Kn (~ 0.5), significant energy jumps do occur at the boundaries which cannot be explained by Fourier law. The effective cross-plane thermal conductivity is calculated as follows:

$$\frac{\kappa_{eff}}{\kappa_{bulk}} = \frac{q_{LBM}}{-\kappa_{bulk}\left(\Delta T_{left} + \Delta T_{film} + \Delta T_{right}\right)/L} \tag{5.18}$$

where q_{LBM} is heat flux predicted by LBM, ΔT_{left} is the temperature jump at left boundary, ΔT_{film} is the temperature difference in the film, and ΔT_{right} is the temperature jump at right boundary.

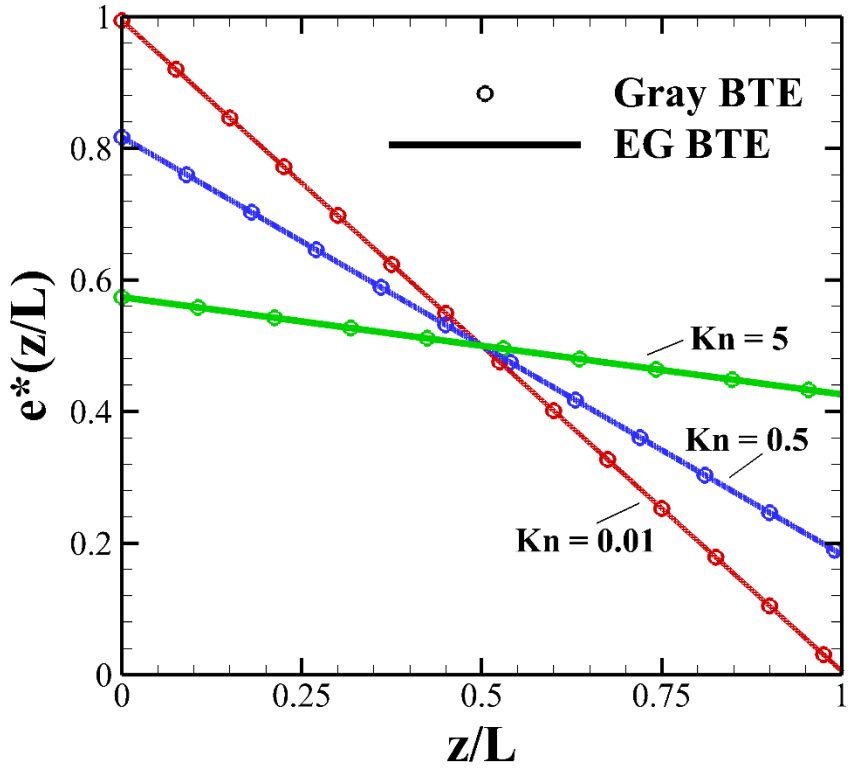

Figure 5.4. Steady-state energy density distribution calculated by LBM for Kn = 0.01, 0.5, 5.

The cross-plane thin film thermal conductivity of silicon predicted using LBM, EPRT (Majumdar [19]), Gray BTE, and EG-BTE are plotted in Fig. 5.5 (normalized by the bulk value). To our best knowledge, experimental cross-plane thermal conductivity measurements for silicon thin films are not available. The LBM predicts almost the same effective thermal conductivity as

that by EPRT because both approach are based on steady-state condition. However, the effective thermal conductivity predicted by Gray BTE and EG BE under transient condition are quite different with their steady-state results (LBM). It should be noted that when we calculate the effective thermal conductivity, the temperature jumps on the boundaries are included. If we don't include temperature jumps in Eq. (5.18), the calculated effective thermal conductivity will always equal the bulk value. Replacing the fixed temperature boundary conditions by constant heat flux boundaries conditions, there are no temperature jumps at the boundaries and the calculated effective thermal conductivity still always equal the bulk value. Therefore, we conclude that applying Eq. (5.18) to calculate the effective thermal conductivity is questionable. But further study is required to explain why the calculated effective thermal conductivities are different under steady-state and transient situations based on the same models.

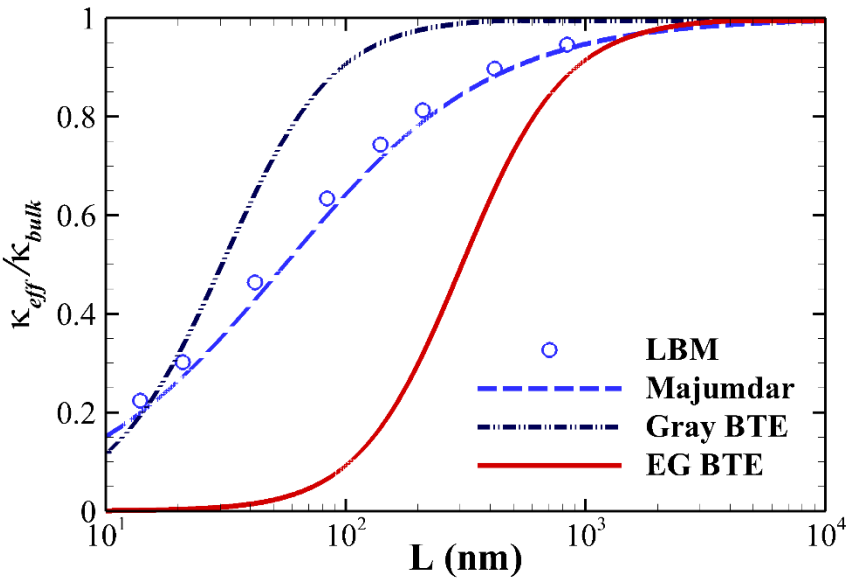

Figure 5.5. Cross-plane thin film thermal conductivity normalized by the bulk value.

5.2 Non-diffusive Heat Conduction in Cryogenic Crystal

Experimental results on nanoscale heat conduction have only presented evidence for breakdown of Fourier's law rather than characterizing ballistic heat conduction. The direct evidence of ballistic heat transport has only been observed in heat-pulse experiments conducted in dielectric crystals at low temperatures [66-73], which provide important benchmark cases for the validation of ballistic heat transfer models. A thorough understanding of these benchmark cases will advance our knowledge in ballistic heat transfer.

Heat conduction in dielectric solid materials is directly determined by phonon generation, propagation and interaction. Phonons may scatter/collide with other phonons, lattice defects, and the lattice boundary. Depending on different length, time and temperature scales characterizing the heat conduction process of the system, there are three competing mechanisms of phonon transport in dielectric crystals, i.e., diffusion, second sound, and ballistic transport. All three heat transport processes can be jointly described on the basis of Boltzmann transport equation (BTE). In the previous studies, Ma has developed a hybrid phonon gas (HPG) model which can completely reconstruct of heat-pulse experiments in NaF at low temperatures in ballistic, intermediate, and diffusive regions [74, 75]. However, the complex viscosity in the HPG model is difficult to interpret its physical meaning. To describe the second sound, Cimmelli and Frischmuth [35] has developed the generalized 4-field model which can reproduce the second sound observed in experiments.

As another test case, we revisit the heat-pulse propagation problem using the EG-BTE and compare the predictions with those of the generalized 4-field model by Cimmelli and Frischmuth. Heat-pulse propagation in a 1cm-thick NaF crystal at T = 15 K is considered. As $t > 0$, a short heat

pulse with 0.2 μs duration is generated on the left-hand side of the crystal and the induced heat-pulse propagation inside the NaF is simulated using the EG-BTE and compare the predictions with those of the generalized 4-field model. The parameters v = 0.47 cm/μs, τ_R = 1.0 μs, $Kn = \tau_R v/L$ = 0.47 are set based on Cimmelli and Frischmuth [35]. In the simulations, we freeze the τ_R and study the time history of non-dimensional energy at a fixed position x = 0.5 cm with the effects from the relaxation time ratio R. The numerical results are compared with that from the generalized 4-field model.

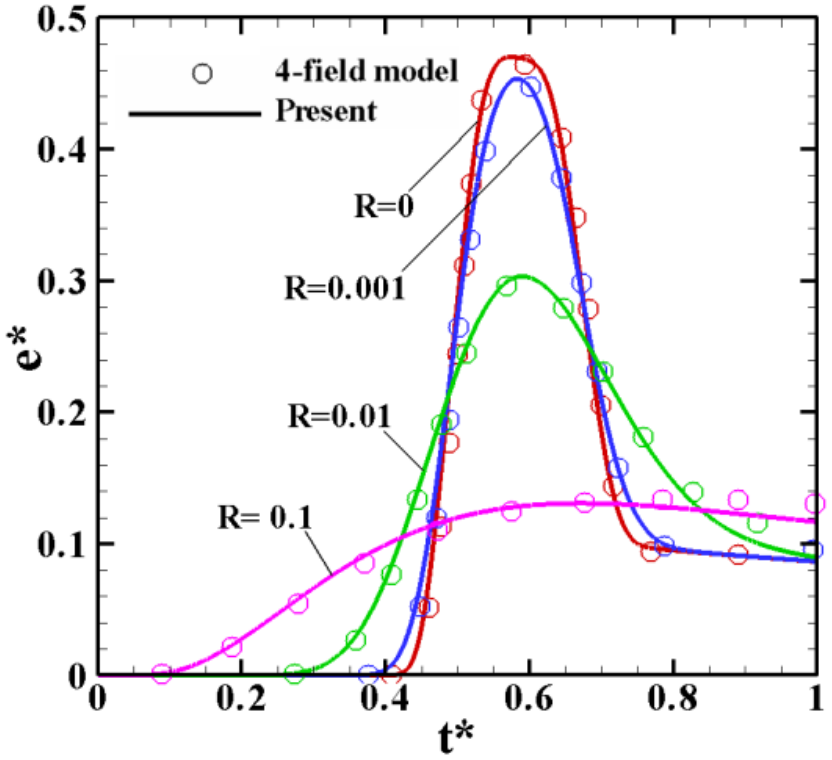

Figure 5.6. Comparison of the evolution of an initial temperature perturbation obtained from the generalized 4-field model and the proposed model for different relaxation time ratios.

Fig. 5.6 shows the comparison of the evolution of an initial temperature perturbation obtained from the generalized 4-field model and the proposed model for different relaxation time

ratios (R = 0, 0.001, 0.01, 0.1). It is found that the amplitude of the thermal waveform becomes smaller and the width of the waveform becomes wider with increasing R. For all different relaxation time rations, the predictions of the EG-BTE model are in good agreement with those by the generalized 4-field model as shown in Fig. 5.6. This demonstrates that the EG-BTE can be applied to study heat-pulse propagation in crystals at low temperatures.

In the previous case, the numerical experiment is studied and compared with other model. Here we will study the real heat-pulse experiments conducted in pure NaF crystals at low temperatures. A Gaussian heat pulse with duration Δt is added to the left side (x = 0) of a crystal, and the temperature change is detected by a thermometer on the right side (x = L). The transient internal energy distribution is calculated based on EG-BTE by the ILBM. Two distinctive modes, i.e., longitudinal and transverse waves are simulated separately and then using superposition to reconstruct the experimental curves. The detected waveforms are very sensitive to the initial crystal temperature at which heat pulses are conducted. For convenience of discussion we divide the results into ballistic, intermediate, and diffusive regions according to temperature. The parameters used in LBM simulations are listed in Table 5.1.

Case #	**T (K)**	**L (mm)**	**Δt (μs)**	$\tau_{R,l}$ **(μs)**	$\tau_{c,l}$ **(μs)**	$\tau_{R,t}$ **(μs)**	$\tau_{c,t}$ **(μs)**
1	9.6	8.3	0.42	1.0	0.51	2.0	1.3
2	13.0	7.9	0.38	1.0	0.48	2.0	0.53
3	25.5	4.3	0.36	0.009	0.045	0.033	0.1

Table 5.1. Parameters used in the LBM simulations.

Case 1. Ballistic Region

In this region, phonons are scattered only at the boundaries of a crystal and most of phonons reach the detector by direct ballistic transport from the heater at their respective mode velocities. As shown in Fig. 5.7, two heat pulses associated with longitudinal and transverse waves were observed at temperature 9.6 K in the [111] direction in NaF [68]. In this direction, the transverse modes are degenerate and thus only two pulses are seen. The velocity of energy propagation can be determined from the oscilloscope trace, i.e., 6051 m/s for longitudinal mode and 3086 m/s for transverse mode. The distinction between these velocities have important effect on the relative amplitudes of the various phonon mode pulses. In an isotropic solid, the ode energy for a given temperature rise is inversely proportional to the cube of the mode velocity. The density of phonon states in the various modes will also influence the relative amplitudes of the thermal pulses. In fig. 5.7, the predicted trace generally agrees with the experimental observations. The observed pulses in experiments are wider than those from LBM simulations, which may result from the wide spectrum of phonons.

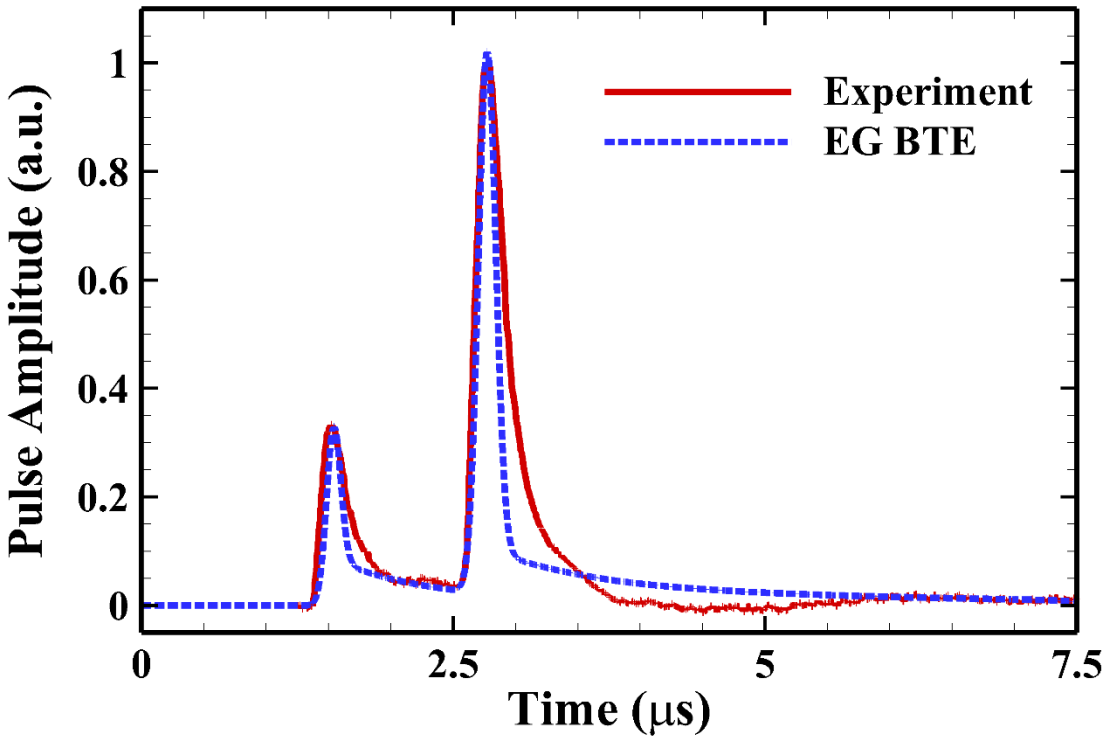

Figure 5.7. Comparison of simulated and detected heat pulses at x = L, T = 9.6 K.

Case 2. Intermediate Region

There is a clearly defined range of temperatures about 10-18 K over which the mode of thermal energy transfer is neither wholly ballistic nor diffusive [76]. In the intermediate region, three distinct heat pulses associated with longitudinal, transverse, and second sound waves were observed at T = 13 K [70] as plotted in fig. 5.8. The second sound velocity is close to $1/\sqrt{3}$ times the transverse velocity. The second sound is followed by a long tail which is thermal diffusion process due to the effect of phonon-phonon scatterings. The individual mode velocities obtained from the experiments are the same as those in ballistic region. The numerical curves fit the observed thermal pulses in the intermediate range well as shown in Fig. 5.8.

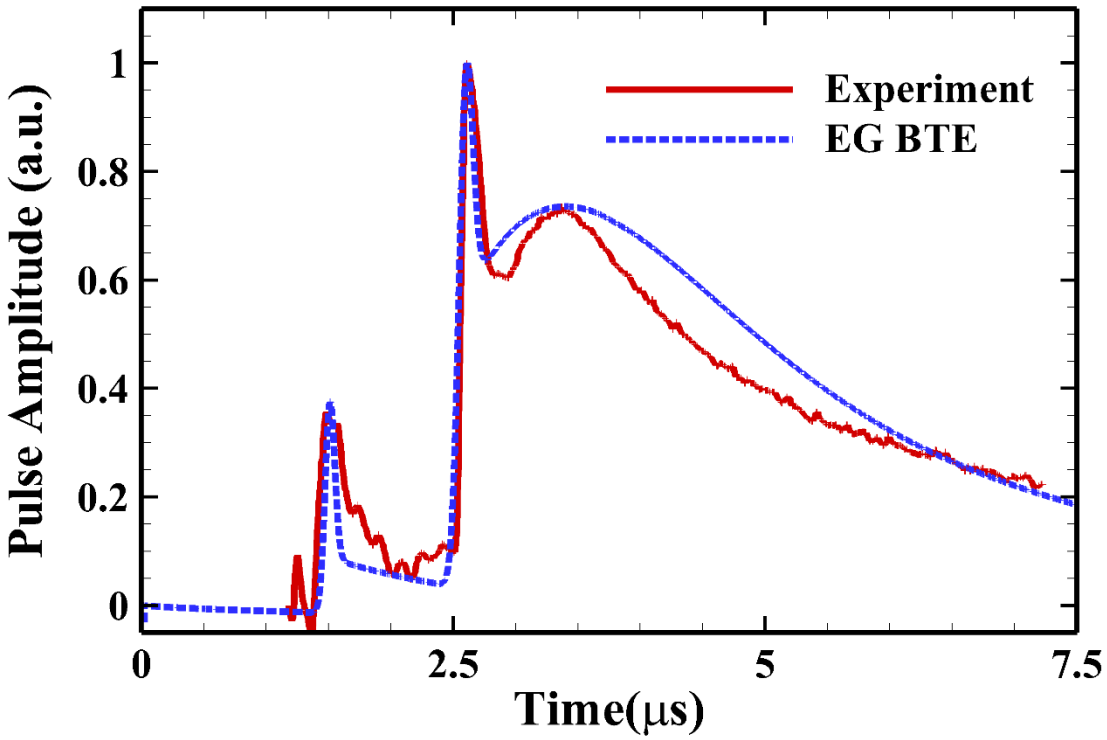

Figure 5.8. Comparison of simulated and detected heat pulses at x = L, T = 13 K.

Case 3. Diffusive Region

Diffusive heat wave propagation satisfies Fourier law. In this region, all the ballistic waves are dissipated into diffusion wave. The heat pulse experiments in NaF at T = 25.5 K was conducted by Rogers [76]. Rogers calculated the pulse trace based on the solution of Fourier law with a point source in an infinite medium. Here we impose EG-BTE to reproduce the transition from ballistic to diffusive processes. There is excellent agreement between present solution and Roger's numerical result which both fit the detected diffusive waveforms very well shown in Fig. 5.9.

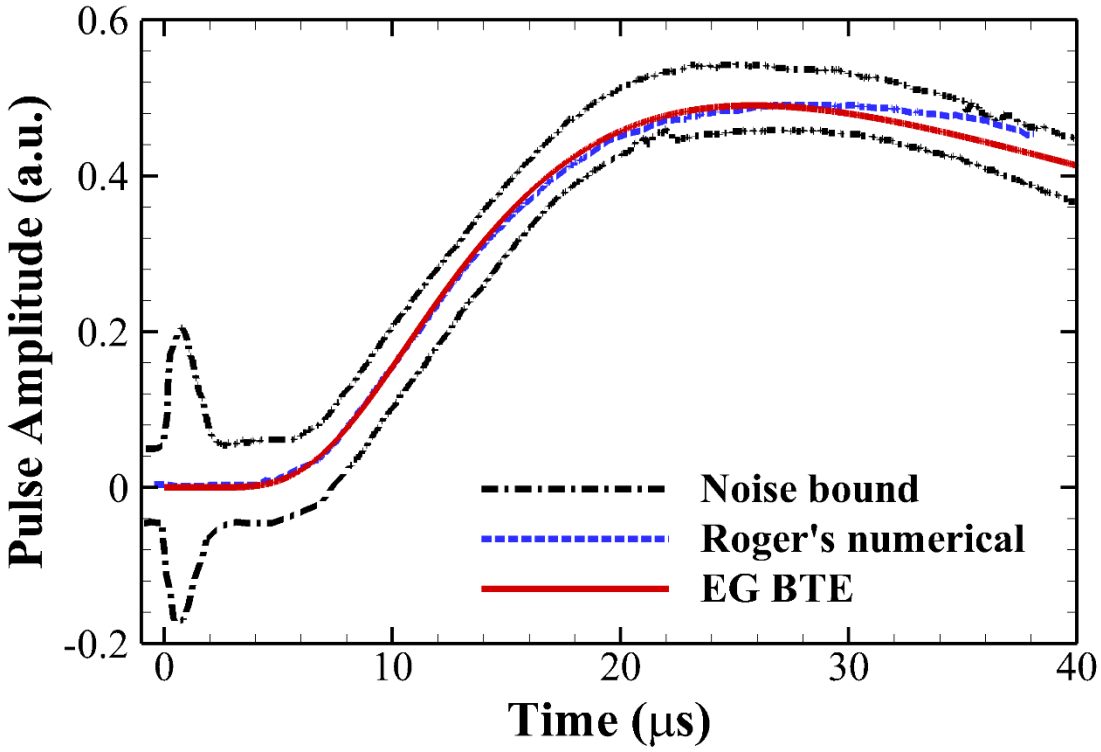

Figure 5.9. Comparison of simulated and detected heat pulses at x = L, T = 25.5 K.

To study the detail how ballistic waves dissipate into diffusive wave, the time evolutions at four different locations are shown in Fig. 5.10. In the early short time range, we do observed the longitudinal wave clearly at location x = 0.1L and x = 0.2L. However, the transverse waves dissipate very fast and eventually are took over by diffusive wave shown in Fig. 5.10 (b), (c) and (d). Compared with ballistic pulse, the width of diffusive wave is much broader due to the delay of strong phonon-phonon scattering processes.

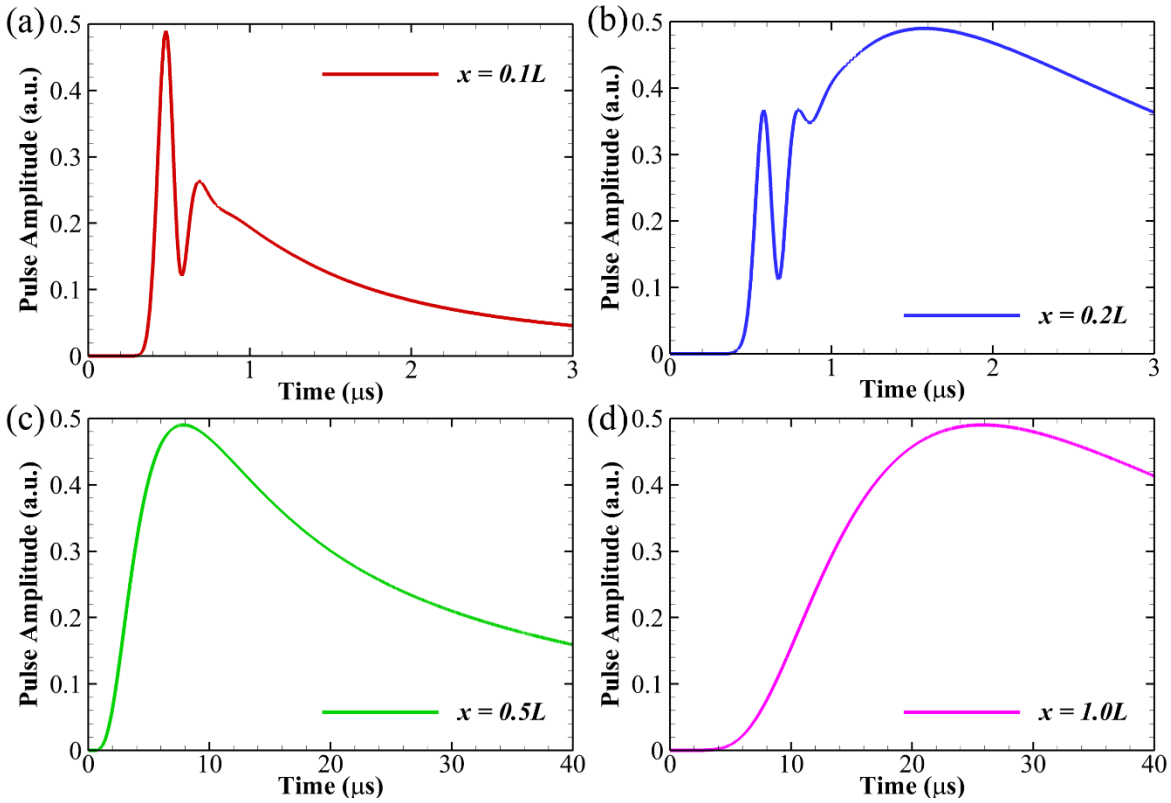

Figure 5.10. The heat pulses evolutions at four different locations in NaF, T = 25.5 K where (a) x = 0.1L; (b) x = 0.2L; (c) x = 0.5L; (d) x = L.

Overall, the propagation of short thermal pulses in pure NaF crystal can be described phenomenologically by EG-BTE. At low temperature, the heat pulses propagate ballistically at the phonon-mode velocities, and at high temperature, the flow of heat is by diffusion. In the intermediate range, the first sound would transit into a second sound, but the phonon-phonon scatterings inhibits the full development of the second sound pulse. The solutions of EG-BTE give a reasonable representation of the observed pulse waveforms, which has convinced us that our interpretation of the heat pulse phenomena is essentially correct.

Chapter 6

Thermo-reflectance Study of Ultrafast Pump-probe Laser Pulse on Metals

6.1 Introduction

Thermal dynamics of nonequilibrium electrons and phonons in metal have been extensively studied by pump-probe transient thermo-reflectance (TTR) techniques [77-82]. The TTR measured signal, i.e., reflectance, changes with variation of dielectric function which is related to temperature change [78-80]. To measure or extract the thermal properties of films, the knowledge of the variation of reflectivity with electron and lattice temperature is critical.

A number of models have been presented to study the correlation between reflectance and temperature. Brorson [77] and Qiu [82] assumed linear relationship between reflectance and temperature. Smith and Norris [80] refined the intraband transitions model (Drude model) by introducing electron-electron and electron-phonon scattering processes. Rustagi [83] derived a thermo-reflectance model through accounting both intraband and interband transitions of electrons. Hohlfeld et al. [79, 84] and Hopkins [81] extended Rustagi's model by taking into account the dependency of temperature in dielectric function.

The main objective in this chapter is to develop a refined model to describe the relationship between reflectance and temperature which is applicable in a wide spectral range from intraband

to interband transition regime. The main contribution of our refinement is to consider the effect of electron Fermi distribution and scattering mechanisms due to temperature change. The model is first used to interpret both intraband and the interband parts of the dielectric response of metals in the wide visible spectral range. Then, it is verified through comparing the predicated reflectance response with the TTR measurements on Au and Cu films in the spectral and temporal domain.

6.2 The Refined Nonlinear Thermo-reflectance model

In the TTR measurement, the laser pulse duration is comparable with electron thermalization time (~ 100 fs). During that short time interval, electrons and phonons are not in thermal equilibrium and have to be considered as two separate systems [82, 85]. The nonequilibrium heating process is described phenomenologically by the two temperature model (TTM) [85],

$$\begin{aligned} C_e(T_e)\frac{\partial T_e}{\partial t} &= \nabla\cdot(k_e\nabla T_e) - G(T_e - T_l) + S \\ C_l\frac{\partial T_l}{\partial t} &= G(T_e - T_l) \end{aligned} \tag{6.1}$$

where T_e is the electron temperature, T_l the lattice temperature, $C_e = \gamma T_e$ the electronic heat capacity, C_l the lattice heat capacity, G the electron-phonon coupling factor, $k = k_{eq}T_e / T_l$ the thermal conductivity [80], and the source term S is expressed in the reference [86].

After temperature evolutions are obtained, the remaining problem is to link them to the reflectance. The reflectance R at air/Au (or Air/Cu) interface is described through the formula [87]

$$R = \frac{(n-1)^2 + k^2}{(n+1)^2 + k^2} \tag{6.2}$$

where refractive index $n+ik=\sqrt{\varepsilon}$ (ε is the dielectric function). The complex dielectric function can be separated into the intraband part (free electrons) and interband part (bound electrons) as [83, 88],

$$\varepsilon = \varepsilon_f + \varepsilon_b \tag{6.3}$$

When the incident photon energy is much less than the interband transition threshold (ITT), the contribution of intraband transitions part from free electrons in the dielectric function is dominated [88]. The intraband part is described by the Drude model (free electron model) given by [87, 89],

$$\varepsilon = 1 - \frac{\omega_p^2}{\omega(\omega + i/\tau)} \tag{6.4}$$

where ω_p is the plasma frequency, ω the frequency of the incident photons, and τ the relaxation time of electron scattering.

For the incident photons in the visible or ultraviolet region, it is essential to take account of the interband contribution to dielectric function [90]. Jha and Warke [88] made the first attempt to theoretically evaluate the relative magnitudes of the intraband and interband contributions. In 1968, Rustagi [83] derived a two-band model to explicitly calculate both intraband and interband contributions. In order to obtain an explicit formula, Rustagi approximated the energy band structure by a flat d-band $E_{dk}=0$, and a parabolic conduction band $E_{ck}=\Delta+\frac{\hbar^2k^2}{2m}$ (Δ is the energy gap between the d-band and conduction band in the center of the Brillouin zone), and assumed the transition matrix element $\langle p \rangle^2$ to be

$$\langle p \rangle^2 = m f_{cd} E_{ck} \tag{6.5}$$

where the oscillator strength f_{cd} is a constant in the Brillouin zone (k-space). He also assumed the Fermi distribution to be

$$f_0(E) = \frac{1}{1+\exp[(E-E_F)/k_B T_e]} = \begin{cases} 1 & (0 < k < k_F) \\ 0 & (k_F < k < k_0) \end{cases} \tag{6.6}$$

Under these assumptions, the dielectric function is expressed as

$$\varepsilon = 1 - \frac{\omega_p^2}{\omega(\omega + i/\tau)} + 3\frac{\omega_p^2}{\omega^2}\frac{f_{cd}}{E_F}\frac{1}{k_F}\int_{k_F}^{k_0}\left(\frac{z_1^2}{k^2 - z_1^2} - \frac{z'^2_1}{k^2 + z'^2_1} - \frac{2z_0^2}{k^2 - z_0^2}\right)E_{ck}\,dk \tag{6.7}$$

However, Eq. (6.6) is valid only if the electron temperature is low $(T_e < 300K)$. This condition is not satisfied for the TTR measurement where the electron temperature can reach as high as several thousand Kelvin as shown in Figure 6.1(a). The electron and lattice temperature is calculated by the TTM. Here we show the Fermi distribution is stretched at a higher electron temperature as plotted in Figure 6.1(b). When the electron temperature reaches 3000 K or higher, the Fermi distribution f_0 cannot be treated as 1 or 0 anymore.

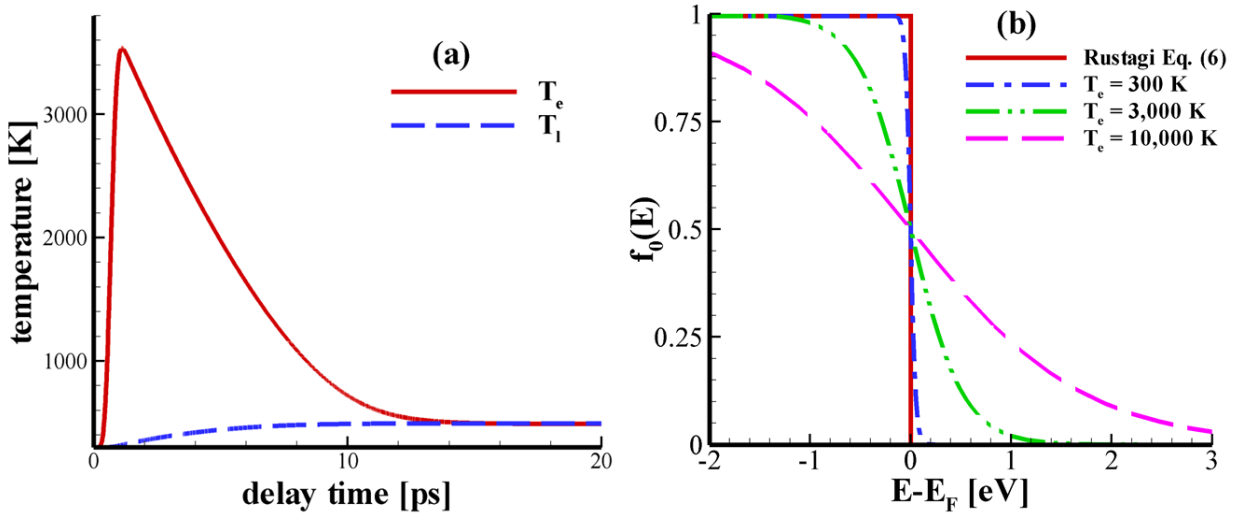

Figure 6.1. (a) Electron and lattice temperature response of gold film in the TTR experiment as predicted by the TTM Eq. (6.1), and (b) the Fermi distribution under different electron temperature.

To consider the temperature effect on the Fermi distribution, we modify the expression of dielectric function in Eq. (6.7) to be

$$\varepsilon = 1 - \frac{\omega_p^2}{\omega(\omega + i/\tau)} + 3\frac{\omega_p^2}{\omega^2}\frac{f_{cd}}{E_F}\frac{1}{k_F}\int_0^{k_0}\left(\frac{z_1^2}{k^2 - z_1^2} - \frac{z'^2_1}{k^2 + z'^2_1} - \frac{2z_0^2}{k^2 - z_0^2}\right)E_{ck}[1 - f_0(k)]dk \qquad (6.8)$$

where E_F is the Fermi energy, $k_F = \sqrt{2m}E_F/\hbar$ the radius of the Fermi Surface, $k_0 = \sqrt[3]{2}k_F$ the radius of the Brillouin zone, and

$$\begin{aligned} z_n^2 &= \frac{2m}{\hbar^2}(n\hbar\omega + in\hbar\omega_c - \Delta), \quad n = 0, 1 \\ z'^2_1 &= \frac{2m}{\hbar^2}(\hbar\omega + i\hbar\omega_c + \Delta) \\ f_0(k) &= \frac{1}{1 + \exp[(\frac{\hbar^2 k^2}{2m} - E_F)/(k_B T_e)]} \end{aligned} \qquad (6.9)$$

Here f_0 is the Fermi distribution[84], k_B the Boltzmann constant, and ω_c the electron collision frequency.

To determine the change of reflectance due to temperature variation, the temperature dependency of electron collision relaxation time τ in dielectric function must be known. In this work, we estimate the relaxation time by combining electron-electron scattering and electron-phonon scattering. According to Fermi liquid theory (FLT) [91, 92], the electron-electron relaxation time is estimated in the form

$$\frac{1}{\tau_{ee}} = \frac{\sqrt{3}\pi^2}{128}\frac{\omega_P}{E_F^2}\frac{(E - E_F)^2 + (\pi k_B T_e)^2}{1 + e^{-(E - E_F)/k_B T_e}} \qquad (6.10)$$

For the temperature above Debye temperature (170 K for gold), the electron-phonon relaxation time is inversely proportional to the lattice temperature [93]. By employing Matthiessen's rule, the total relaxation time is given by

$$\frac{1}{\tau} = \frac{1}{\tau_{ee}} + \frac{1}{\tau_{ep}} = AT_e^2 + BT_l \tag{6.11}$$

where the constant coefficients A and B are determined by experiment measurements [93, 94].

6.3 Calculation of Dielectric Function and Thermo-reflectance

In this section, we implement the models described in Section 6.2 to calculate the dielectric function and thermo-reflectance response of gold and copper.

The dielectric function of gold at room temperature calculated by the Drude, Rustagi, and present models are compared with the experimental data in Fig. 6.2(a) and (b). All the parameters needed are listed in Table 6.1. As shown in Fig. 6.2, the Drude model significantly deviates from the experimental data when probe photon energy larger than 1.5 eV since it only considers intraband transitions. The results obtained by the other two models are in good agreement with the experimental data. The difference in the results of Rustagi and present model is due to (1) the electron temperature effect on the Fermi distribution and (2) a more accurate explanation of electron relaxation time used in present model. The relaxation time used in Rustagi model (1968) is a constant, whereas Eq. (6.10) and (6.11) are used in the present modeling. The present modeling achieves the best match with measurements.

The calculated dielectric function of copper presented in Fig. 6.3(a) is at room temperature, and (b) is at electron temperature of 3000 K. For Drude model or Rustagi model, the calculated

results in (a) and (b) are the same because they neglect the effect of electron temperature on the Fermi distribution. Actually, it is essential to consider the stretching of the Fermi distribution when electron temperature is high. As shown in Fig. 6.3(b), when the electron temperature reaches 3000 K, dielectric function predicted by present model differs markedly from the room temperature result.

Parameter	E_F	$\hbar\omega_p$	$\hbar\omega_c$	Δ	f_{cd}	A	B
Units	eV	eV	eV	eV	1	$10^7 K^{-2}s^{-1}$	$10^{11} K^{-2}s^{-1}$
Value	5.51	8.9	0.15	-2.95	0.26	1.2	1.23

Table 6.1, Parameters used in the calculation of gold.

Parameter	E_F	$\hbar\omega_p$	$\hbar\omega_c$	Δ	f_{cd}	A	B
Units	eV	eV	eV	eV	1	$10^7 K^{-2}s^{-1}$	$10^{11} K^{-2}s^{-1}$
Value	7.0	9.06	0.09	-4.81	0.265	0.8	1.6

Table 6.2, Parameters used in the calculation of copper.

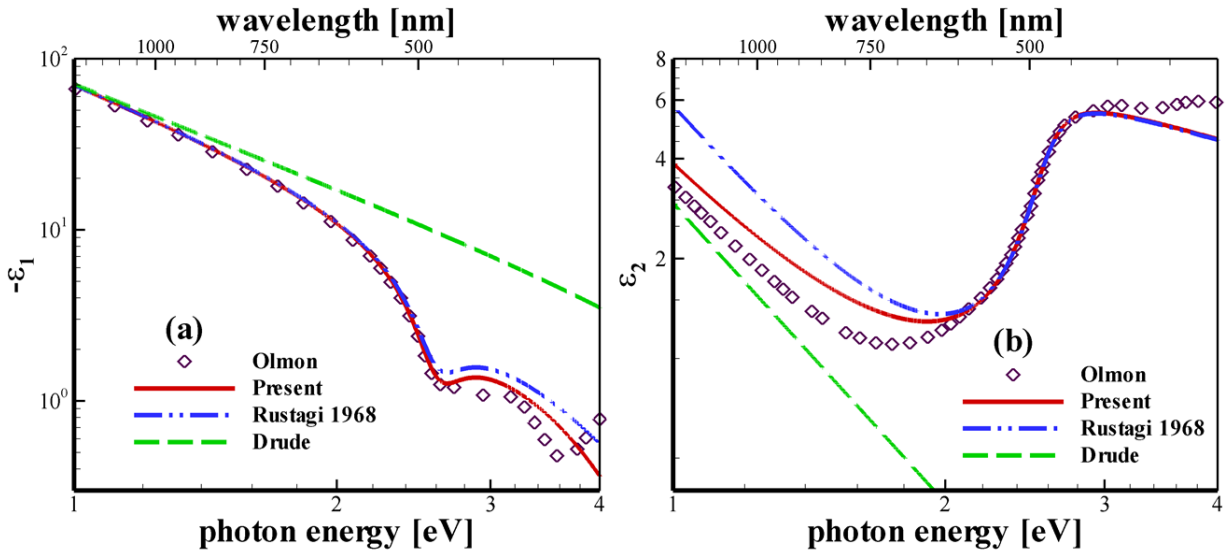

Figure 6.2. (a) Negative real part $-\varepsilon_1$, and (b) imaginary part ε_2 in dielectric function ε of gold at room temperature. The symbol represents the experimental data and the lines represent the calculations by models. The experimental data is from Olmon [89].

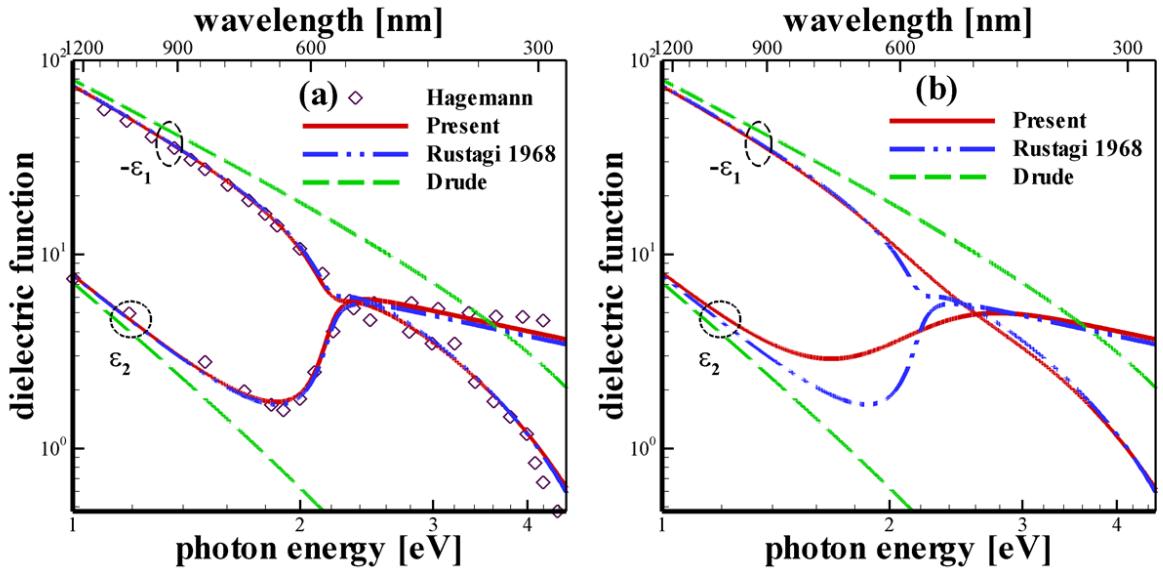

Figure 6.3. (a) Negative real part $-\varepsilon_1$ and imaginary part ε_2 in dielectric function ε of copper at room temperature; (b) dielectric function ε of Cu at $T_e = 3000\ K$. The symbol represents the experimental data and the lines represent the calculations by models. The experimental data is from Hagemann [95].

In the previous two paragraphs, we have shown the comparisons of calculations by different models with measured dielectric function over spectral domain [96, 97]. Based on the obtained dielectric function, it is straightforward to calculate the transient reflectivity. Here we verify the quality of present model by interpreting TTR signal in temporal domain.

Fig. 6.4 compares results obtained by Rustagi model and present model with measured transient reflectivity evolutions of gold film at pump fluence 5.28 mJ/cm^2 and probe wavelengths (a) 570 nm, (b) 530 nm, (c) 490 nm, and (d) 470 nm [98]. Here gold film thicker than 1μm is used

to eliminate the influence of interface heat transfer in the interested time regime (it can be treated as bulk gold). As shown in the figure, the predications of present model show good match with experimental data. The Fermi distribution in present model captures the change of electronic occupancy due to the variation of electron temperature. However, this change is neglected in the Rustagi model. Therefore there is large deviation in the calculations of Rustagi model compared to experiment. When the probe wavelength is far off the ITT (502 nm in Au) in case (a) 570 nm, the change of electronic occupancy is small with the increment of electron temperature in the Fermi distribution. Thus the difference of calculations by the two models is not as significant in Fig. 6.4 (a) as that in (b), (c) and (d).

In the calculations, electron thermalization time and electron-phonon coupling rate G can be determined. After absorption of laser pulse, the electrons are out of equilibrium state. The electron thermalization time is how long the perturbed electrons will take to reach a Fermi distribution. At electron energy 2.17 eV (570 nm), the thermalization time is 140 fs. At electron energies close to the Fermi surface, longer thermalization times 280 fs for 2.34 eV (530 nm) and 350 fs for 2.53 eV (490 nm) are observed. These results are in agreement with Fermi liquid theory that the electron lifetime τ_{th} is related to the energy difference with Fermi level, i.e., $\tau_{th} \propto (E - E_F)^{-2}$. For the electron-phonon coupling rate, no energy dependency is found. The same value of $G = 1.5\times10^{16}$ W/m^{3}K is obtained for all the probe wavelengths. It indicates that electron-phonon scattering processes are independent of electron thermalization processes.

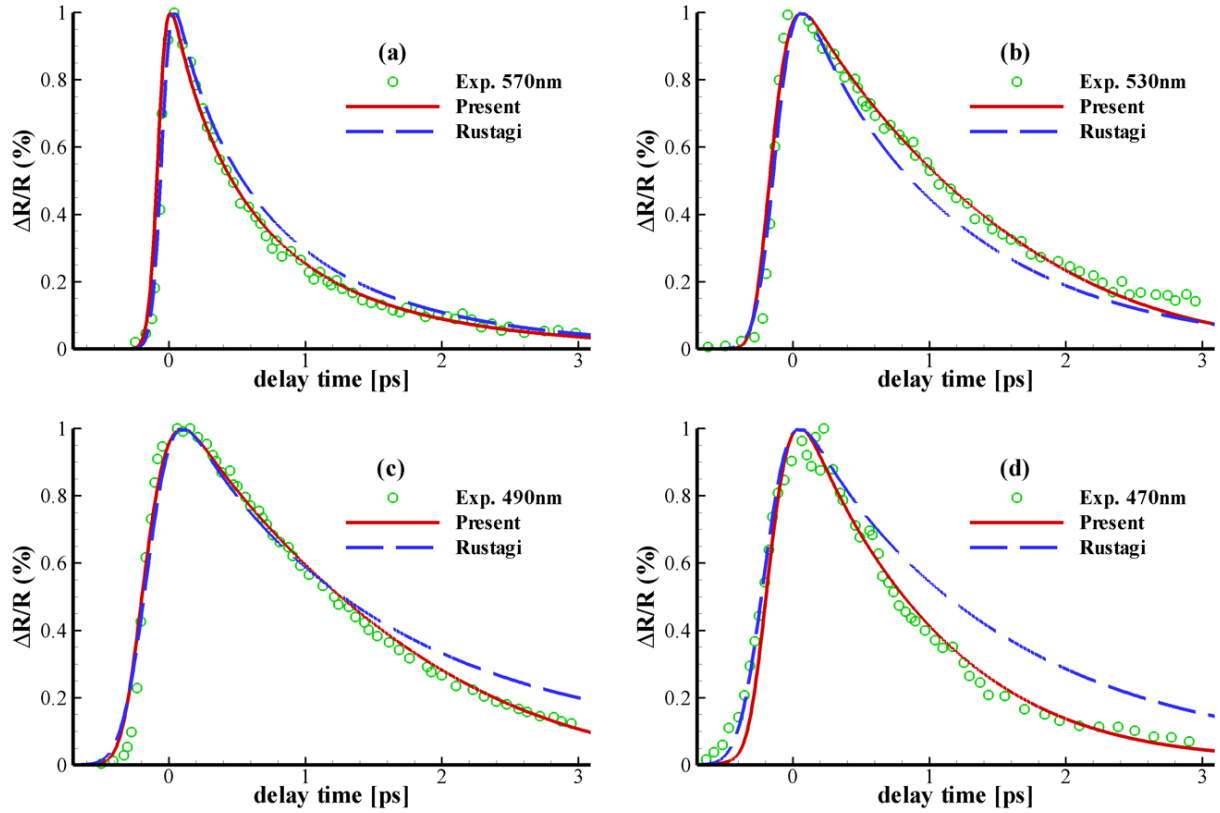

Figure 6.4. Comparison of measured transient reflectivity of bulk gold with predication by two models at probe wavelength (a) 570 nm, (b) 530 nm, (c) 490 nm, and (d) 470 nm. We set the maximum values to be positive for convenience.

To make a thorough understanding of the electron thermal dynamics in metals, we further examine the electron behavior under different pump excitations. Fig. 6.5 shows the comparison between the transient reflectance signals of bulk gold with the calculations obtained by present model at probe wavelength (490 nm) and pump fluence (a) 1.76 mJ/cm^2, (b) 3.52 mJ/cm^2, (c) 5.28 mJ/cm^2, and (d) 7.04 mJ/cm^2. The calculations are well matched with the experimental data for all pump fluences. The electron thermalization time shows no fluence dependency (τ_{th}=350 fs is obtained for all the fluences). This is easy to understand that since the electron thermalization processes are measured at the same probe wavelength, the related electron energy is the same.

According to the Fermi liquid theory, the electron thermalization time should not change for different pump fluence. For the electron-phonon coupling rate G, the best fit is 1.2×10^{16} W/m^{3}K for 1.76 mJ/cm^2, 1.35×10^{16} W/m^{3}K for 3.52 mJ/cm^2, 1.5×10^{16} W/m^{3}K for 5.28 mJ/cm^2, and 1.65×10^{16} W/m^{3}K for 7.04 mJ/cm^2. For higher electron temperature, induced by stronger pump fluence, the electron system relaxes with the phonons more readily resulting in an increased electron-phonon coupling rate, which is consistent with the work of Hopkins et al. [99, 100].

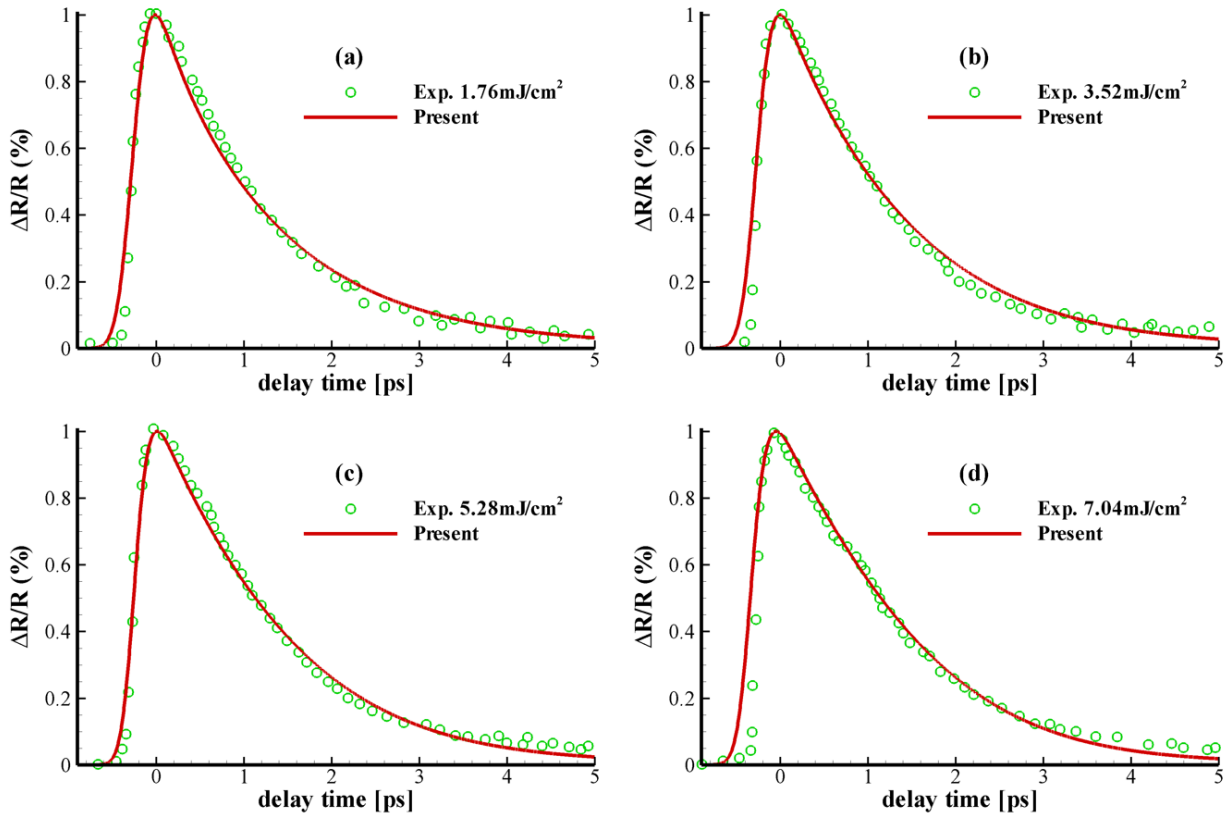

Figure 6.5. Comparison between the transient reflectance signals of bulk gold [98] with the calculations by present model at pump fluence (a) 1.76 mJ/cm^2, (b) 3.52 mJ/cm^2, (c) 5.28 mJ/cm^2, and (d) 7.04 mJ/cm^2.

Fig. 6.6(a), (b), (c), and (d) compare the calculations by the two models with measured transient reflectivity evolutions of Au at different probe wavelength. The Fermi distribution in present model based on Eq. (6.8) captures the change in electronic occupancy due to the variation of electron temperature. The change is neglected in the Rustagi model which is based on Eq. (6.7). Therefore, the predications of the present model shows better match with the experiment compared to Rustagi model (1968) as shown in Fig. 6.6(b), (c), and (d). However in case (a), the probe energy (1.95 eV) is blew interband transition threshold (ITT, 2.47 eV in Au). The interband part in the model is not dominated compared to intraband part. Thus, the difference in results predicated by the two models is not that significant in Fig. 6.6(a) as the difference in (b), (c) and (d). Overall, the present model obtained much better agreement with experiment data over the intraband and interband transition range compared to Rustagi's original model.

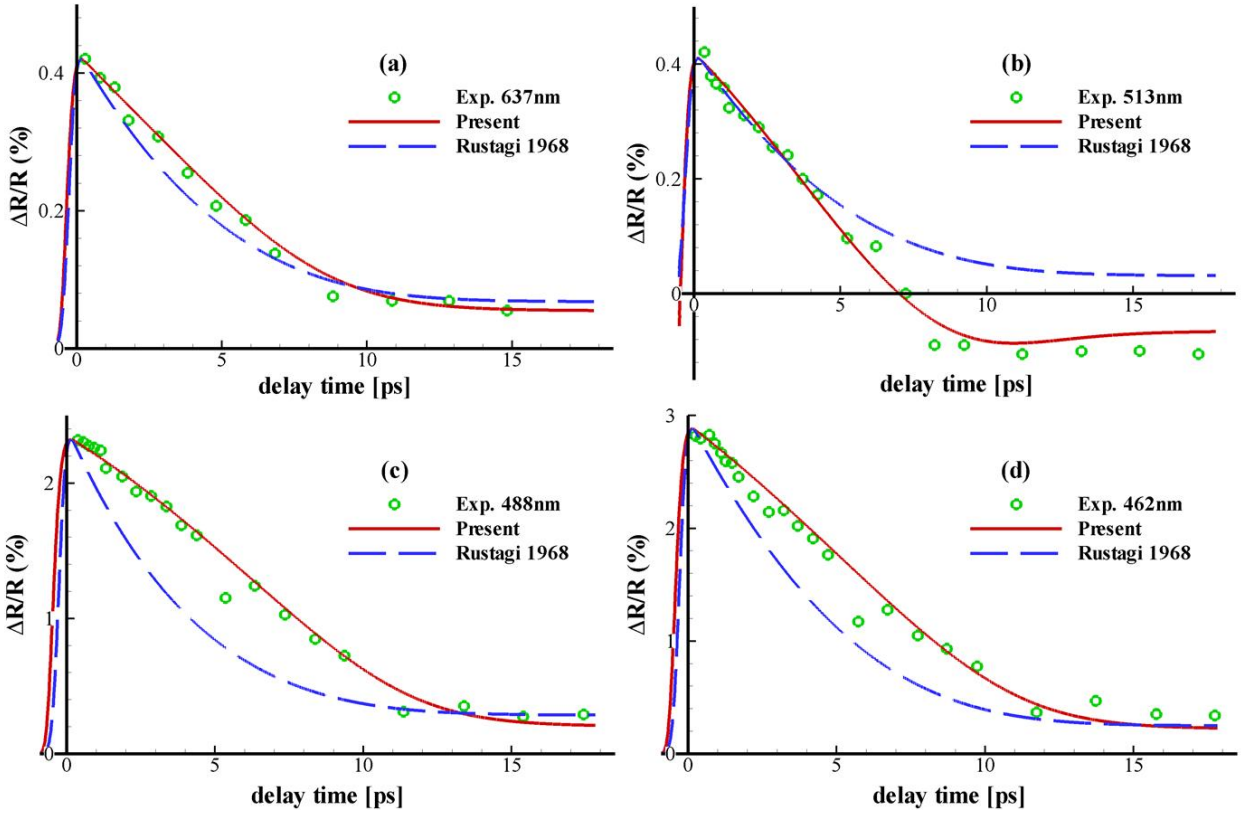

Figure 6.6. Comparison of measured transient reflectivity of Au [96, 97] with predication by two models at different probe wavelength ((a) 637 nm, (b) 513 nm, (c) 488 nm, and (d) 462 nm, here we always set the maximum reflectivity to be positive for convenience).

We have checked the performance of the models in Au. Now we apply the models to study TTR response in Cu. At first, we study the reflectivity evolution in intraband transition range (the ITT for Cu 2.1 eV, related 590 nm) to determine all the parameters needed as plotted in Fig. 6.7(a). The intraband component in dielectric function is dominated in case (a) where the probe wavelength is 787 nm. The difference in interband component predicted by three models is small. Thus, the calculations of three models are all in good agreement with the experiment. For the other wavelengths, we keep the parameters the same as (a). Fig. 6.7(b), (c) and (d) only show the predictions of normalized change in reflectance by three models in interband transition regime due

to lack of experimental data. For all the four wavelengths, Drude model (green dash lines) gives the same predictions, which means it cannot be applied in the interband transition regime. The prediction of Rustagi model clearly decays too quickly in the early portion in case (b), and does not decay rapidly enough in the latter stage in case (b), (c) and (d). This discrepancy increases with decreasing wavelength. From these comparisons, we unambiguously conclude that it is necessary to consider the stretching of the Fermi distribution due to temperature change especially in the interband transitions regime.

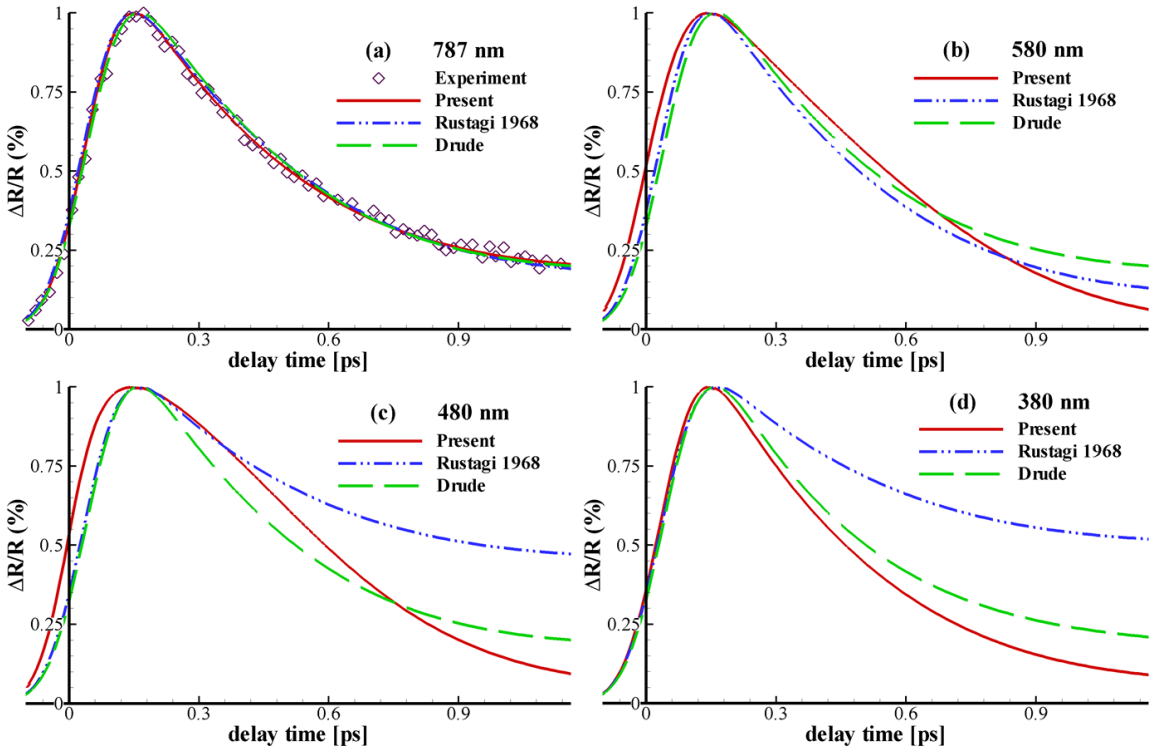

Figure 6.7. (a) comparison of normalized measured TTR of Cu [96] with three models at probe wavelength 787 nm; predication of normalized TTR by three models at different probe wavelength ((b) 580 nm, (c) 480 nm, and (d) 380 nm).

A refined thermo-reflectance model is developed to describe the correlation between reflectance and temperature. The refined model is justified for the incident photon in a wide range

from intraband to interband transitions regime. Its predications of dielectric function and reflectance response are compared with the experimental measurements of gold and copper in the spectral and temporal domain. A significant improvement is achieved by the present model in the comparison with the Drude and Rustagi models. This investigation has shown that the stretching of the Fermi distribution due to temperature increment is responsible for interpreting thermo-reflectance response especially in the interband transitions regime. Another contribution of the current work is that electron-electron scattering and electron-phonon scattering are investigated to obtain the accurate total relaxation time. The electron thermal relaxation processes are exploited in the intra- and interband regime. It is shown that the electron thermalization time becomes longer for electron energy closer to Fermi level but has no fluence dependency. In the opposite, the electron-phonon coupling rate G shows no electron energy dependency but increases with stronger fluence. These results are consistent with the Fermi liquid theory and the work of Hopkins. Overall, the present model is a much better alternative to the Drude and Rustagi models for data analysis in ultrafast pump-probe metrology.

Chapter 7

Summary and Future Work

7.1 Summary

In this thesis, we investigated non-diffusive heat conduction in nano-/micro-structures through both numerical simulation and theoretical analysis. The enhanced gray BTE (EG-BTE) model were developed to characterize the non-diffusive nature of heat conduction by the ballistic mean free time and the diffusive relaxation time. Theoretical solutions of EG-BTE based on Fourier transform where presented for simple geometries in three-dimensional domain. For complex geometries where analytical solutions are not available, we developed the implicit lattice Boltzmann method (LBM) to solve EG-BTE. To the best of our knowledge, the implicit LBM was the first time to be developed for solving BTE. The features of implicit LBM is unconditionally stable and computationally efficient.

The EG-BTE was validated by transient thermal grating (TTG) experiment and time domain thermo-reflectance (TDTR) experiment. A theoretical framework was created based on EG-BTE, which can be applied to replace Fourier's law for experimental data analysis. Using the new model, we were able to explain the nonlocal thermal transport by long mean free path (MFP) phonons. We have also shown that the ballistic phonon transport is dominant where the phonon MFP is comparable to the length scale of the transport domain. The systematical study of the

experimental decay traces yielded the quantitative information of ballistic phonon MFP which can reach as long as several micron in silicon at room temperature.

The EG-BTE was applied to explore two typical non-diffusive heat transfer problems in thin films and cryogenic crystals. For phonon transport in thin films, boundary condition is the crucial factor for predicting effective thermal conductivity correctly. We have developed the absorption boundary condition which gives better interpretation of the thickness dependent thermal conductivity than the traditional diffusive reflection boundary condition. For phonon transport in cryogenic crystals, the direct evidence of ballistic thermal wave transport was observed in heat-pulse experiments. The successful interpretation of this benchmark ballistic wave transport by EG-BTE provided a thorough understanding of the physical nature of non-diffusive heat transfer.

Besides, we also studied the thermal dynamics of nonequilibrium electrons and phonons in metals. A refined model was presented to describe the correlations between reflectance, electron temperature and lattice temperature in a wide spectral range from intraband to interband transition regime. It was shown that the electron thermalization time becomes longer as electron energy getting closer to Fermi level but has no pump fluence dependency. In the opposite, the electron-phonon coupling rate had no electron energy dependence but increased with the increase of pump fluence.

The author's overall contribution of this dissertation consisted in developing a unique (EG-BTE) model to characterize the non-diffusive nature of heat conduction in nano-/micro-scale structures and a new theoretical framework based on EG-BTE that can replace Fourier law for experimental data analysis. Phonon transport in thin films and cryogenic crystal were evaluated using this novel thermal transport model and found in good agreement with experimental data reported independently. The comprehensive understanding of the underlying physics of non-

diffusive heat transfer will greatly benefit us for designing better heat removal strategies for microelectronic devices.

7.2 Future Work

Although the developed theoretical tools show good capability for analyzing nano-/micro-scale heat transfer, further development and closer examination are required in the following aspects.

7.2.1 Theoretical determination of ballistic mean free time

The major limitation of the proposed EG-BTE is that the ballistic mean free time τ_c is determined by curve fitting the experimental data instead of theoretical approach. As described in section 4.1, the diffusive mean free time τ_R is determined directly by material properties ($\tau_R = 3\kappa / C_v v^2$). In theory, it is possible to determine the ballistic mean free time τ_c through lattice dynamics calculation or first-principles calculation. After determining τ_c theoretically, the prediction power of EG-BTE will greatly increase which will help for guiding experiment designs.

7.2.2 Study thermal transport across supperlattices

Superlattice films consist of periodically alternating layers of two different materials stacked upon each other. Thermal transport in semiconductor superlattices is important due to applications in thermoelectric devices. To increase the performance of the thermoelectric devices, these films need to have low thermal conductivity. On the contrary, supperlattice films with high thermal conductivity are desired to dissipate heat in semiconductor lasers. The challenge of studying thermal transport across supperlattices is the interfacial thermal resistance between two

materials, which is a longstanding problem in nanoscale thermal transport. The classical acoustic mismatch (AMM) or diffusive mismatch (DMM) model cannot agree with experimental data. To extend EG-BTE for studying thermal transport across supperlattices, an appropriate interfacial condition is required to be developed.

7.2.3 Investigate heat transport in metallic grating structures

We have studied heat transport in transient thermal grating (TTG) experiment. We may extend this study to metallic grating structures as shown in Fig. 7.1. For thermal grating, the period of grating is limited by the laser wavelength which is several hundred nanometers. For metallic grating, the period of grating can be as short as several nanometers. Besides, there is thermal transport from metal strips (or metal lattice) to substrate in metallic grating. We can simulate the heat dissipation in microelectronics by investigating thermal transport in metallic grating structures at nanoscale.

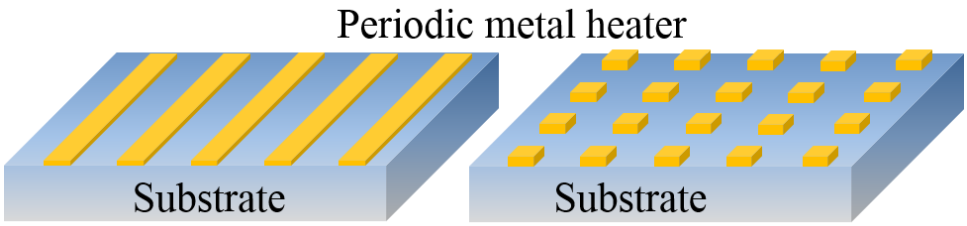

Figure 7.1. Metallic grating structures at nanoscale, (left) metal strips deposited on substrate, (right) metal lattice deposited on substrate.

7.2.4 Discover phonon wave transport at room temperature

In section 5.1, we have discussed the phonon wave transport at low temperatures in crystals. However, so far no observation of phonon wave transport at room temperature has been reported. We can apply EG-BTE to theoretically or numerically study that whether it is possible or not to

observe phonon wave transport at room temperature. One good starting point is to study thermal transport in nanostructures since the phonon mean free path (MFP) is comparable to its length scale.

7.2.5 Systematically studying heat transfer of hot spots

Packing more and more transistors onto a single chip and doing high speed computing can result in intense hot spots. Overheating can drastically reduce the performance and reliability of electronic devices and cause failures in applications. The inability to remove heat efficiently is currently one of the major obstacles toward further miniaturization and advancement of these devices. It is necessary to systematically study heat transfer of hot spots for designing better microelectronic cooling systems. The detailed thermal decay information of hot spots can be obtained through numerical simulations based on EG-BTE. By comparing the simulation results for different designs or systems, it is very helpful to find the new approach to improve the heat removal efficiency.

Bibliography

1. Chowdhury, I., et al., *On-chip cooling by superlattice-based thin-film thermoelectrics.* Nature Nanotechnology, 2009. **4**(4): p. 235-238.

2. Wang, P. and A. Bar-Cohen, *Self-cooling on germanium chip.* Components, Packaging and Manufacturing Technology, IEEE Transactions on, 2011. **1**(5): p. 705-713.

3. Shakouri, A. and Y. Zhang, *On-chip solid-state cooling for integrated circuits using thin-film microrefrigerators.* Components and Packaging Technologies, IEEE Transactions on, 2005. **28**(1): p. 65-69.

4. Mahajan, S., *The role of materials science in the evolution of microelectronics.* MRS Bulletin, 2015. **40**(12): p. 1079-1088.

5. Wang, D., Z. Qu, and Y. Ma, *An enhanced Gray model for nondiffusive heat conduction solved by implicit lattice Bolzmann method.* International Journal of Heat and Mass Transfer, 2016. **94**: p. 411-418.

6. Cahill, D.G., et al., *Nanoscale thermal transport. II. 2003–2012.* Applied Physics Reviews, 2014. **1**(1): p. 011305.

7. Cahill, D.G., et al., *Nanoscale thermal transport.* Journal of Applied Physics, 2003. **93**(2): p. 793-818.

8. Chen, G. and A. Shakouri, *Heat transfer in nanostructures for solid-state energy conversion.* Journal of Heat Transfer, 2002. **124**(2): p. 242-252.

9. Collins, K.C., et al., *Non-diffusive relaxation of a transient thermal grating analyzed with the Boltzmann transport equation.* Journal of Applied Physics, 2013. **114**(10): p. 104302.

10. Ding, D., X. Chen, and A. Minnich, *Radial quasiballistic transport in time domain thermo-reflectance studied using Monte Carlo simulations.* Applied Physics Letters, 2014. **104**(14): p. 143104.

11. Wilson, R. and D.G. Cahill, *Anisotropic failure of Fourier theory in time domain thermo-reflectance experiments.* Nature communications, 2014. **5**.

12. Johnson, J.A., et al., *Direct measurement of room-temperature nondiffusive thermal transport over micron distances in a silicon membrane.* Physical review letters, 2013. **110**(2): p. 025901.

13. Majumdar, A., *Microscale energy transport in solids*. 1998, Taylor and Francis, Washington, DC. p. 1-94.

14. Ziman, J., *Electrons and phonons*. 1961, Oxford University Press, London.
15. Kittel, C., *Introduction to solid state physics*. 2005: Wiley.

16. Larsson, K., *Inelastic scattering of neutrons in solids and liquids: Vol. 1., Proc. Symp. Chalk River, 1962 (IAEA, Vienna)*. 1963, North-Holland.

17. McGaughey, A.J. and M. Kaviany, *Phonon transport in molecular dynamics simulations: Formulation and thermal conductivity prediction.* Advances in Heat Transfer, 2006. **39**: p. 169-255.

18. Rapaport, D.C., *The art of molecular dynamics simulation*. 2004: Cambridge university press.

19. Majumdar, A., *Microscale heat conduction in dielectric thin films.* Journal of Heat Transfer, 1993. **115**(1): p. 7-16.

20. Chen, G., *Nanoscale energy transport and conversion: a parallel treatment of electrons, molecules, phonons, and photons*. 2005: Oxford University Press, USA.

21. Bhatnagar, P.L., E.P. Gross, and M. Krook, *A model for collision processes in gases. I. Small amplitude processes in charged and neutral one-component systems.* Physical review, 1954. **94**(3): p. 511.

22. Chen, G., *Ballistic-diffusive equations for transient heat conduction from nano to macroscales.* Journal of Heat transfer, 2002. **124**(2): p. 320-328.

23. Narumanchi, S.V., J.Y. Murthy, and C.H. Amon, *Submicron heat transport model in silicon accounting for phonon dispersion and polarization.* Journal of Heat Transfer, 2004. **126**(6): p. 946-955.

24. Kremer, G.M., *An introduction to the Boltzmann equation and transport processes in gases*. 2010: Springer Science & Business Media.

25. Cheng, L., M. Xu, and L. Wang, *From Boltzmann transport equation to single-phase-lagging heat conduction.* International Journal of Heat and Mass Transfer, 2008. **51**(25): p. 6018-6023.

26. Shi, L., *Thermal and thermoelectric transport in nanostructures and low-dimensional systems*. Nanoscale and Microscale Thermophysical Engineering, 2012. **16**(2): p. 79-116.

27. Tien, C.L., *Microscale energy transfer*. 1997: CRC Press.

28. Alvarez, F. and D. Jou, *Memory and nonlocal effects in heat transport: from diffusive to ballistic regimes.* Applied physics letters, 2007. **90**(8): p. 083109.

29. Cimmelli, V., A. Sellitto, and D. Jou, *Nonlocal effects and second sound in a nonequilibrium steady state.* Physical Review B, 2009. **79**(1): p. 014303.

30. Tzou, D., *Nonlocal behavior in phonon transport.* International Journal of Heat and Mass Transfer, 2011. **54**(1): p. 475-481.

31. Ma, Y., *A two-parameter nondiffusive heat conduction model for data analysis in pump-probe experiments.* Journal of Applied Physics, 2014. **116**(24): p. 243505.

32. Sverdrup, P.G., Y.S. Ju, and K.E. Goodson, *Sub-continuum simulations of heat conduction in silicon-on-insulator transistors.* Journal of Heat Transfer, 2001. **123**(1): p. 130-137.

33. Minnich, A.J., et al., *Thermal conductivity spectroscopy technique to measure phonon mean free paths.* Physical review letters, 2011. **107**(9): p. 095901.

34. Hua, C. and A.J. Minnich, *Transport regimes in quasiballistic heat conduction.* Physical Review B, 2014. **89**(9): p. 094302.

35. Cimmelli, V. and K. Frischmuth, *Gradient generalization to the extended thermodynamic approach and diffusive-hyperbolic heat conduction.* Physica B: Condensed Matter, 2007. **400**(1): p. 257-265.

36. Tzou, D., *A unified field approach for heat conduction from macro-to micro-scales.* Journal of Heat Transfer, 1995. **117**(1): p. 8-16.

37. Guyer, R.A. and J. Krumhansl, *Solution of the linearized phonon Boltzmann equation.* Physical Review, 1966. **148**(2): p. 766.

38. He, X. and L.-S. Luo, *Theory of the lattice Boltzmann method: From the Boltzmann equation to the lattice Boltzmann equation.* Physical Review E, 1997. **56**(6): p. 6811.

39. Chen, S. and G.D. Doolen, *Lattice Boltzmann method for fluid flows.* Annual review of fluid mechanics, 1998. **30**(1): p. 329-364.

40. Succi, S., *The lattice Boltzmann equation: for fluid dynamics and beyond*. 2001: Oxford university press.

41. Shan, X. and H. Chen, *Lattice Boltzmann model for simulating flows with multiple phases and components.* Physical Review E, 1993. **47**(3): p. 1815.

42. Chiavazzo, E., et al., *Coupling of the model reduction technique with the lattice Boltzmann method for combustion simulations.* Combustion and Flame, 2010. **157**(10): p. 1833-1849.

43. Escobar, R., B. Smith, and C. Amon, *Lattice Boltzmann modeling of subcontinuum energy transport in crystalline and amorphous microelectronic devices.* Journal of electronic packaging, 2006. **128**(2): p. 115-124.

44. Escobar, R.A., et al., *Multi-length and time scale thermal transport using the lattice Boltzmann method with application to electronics cooling.* International Journal of Heat and Mass Transfer, 2006. **49**(1): p. 97-107.

45. Zhang, Z.M., *Nano/microscale heat transfer*. 2007: McGraw-Hill New York.

46. Wang, D. and Y. Ma. *A Novel Approach for Lattice Boltzmann Modeling of Energy Transport*. in *ASME 2012 International Mechanical Engineering Congress and Exposition*. 2012. American Society of Mechanical Engineers.

47. Christensen, A. and S. Graham, *Multiscale lattice Boltzmann modeling of phonon transport in crystalline semiconductor materials.* Numerical Heat Transfer, Part B: Fundamentals, 2010. **57**(2): p. 89-109.

48. Narumanchi, S.V., J.Y. Murthy, and C.H. Amon, *Boltzmann transport equation-based thermal modeling approaches for hotspots in microelectronics.* Heat and mass transfer, 2006. **42**(6): p. 478-491.

49. Pisipati, S., et al., *A novel alternate approach for multiscale thermal transport using diffusion in the Boltzmann Transport Equation.* International Journal of Heat and Mass Transfer, 2011. **54**(15): p. 3406-3419.

50. Johnson, J.A., et al. *Experimental evidence of non-diffusive thermal transport in Si and GaAs*. in *MRS Proceedings*. 2011. Cambridge Univ Press.

51. Chen, G., *Phonon heat conduction in nanostructures.* International journal of thermal sciences, 2000. **39**(4): p. 471-480.

52. Minnich, A.J., *Multidimensional quasiballistic thermal transport in transient grating spectroscopy.* Physical Review B, 2015. **92**(8): p. 085203.

53. Schmidt, A.J., X. Chen, and G. Chen, *Pulse accumulation, radial heat conduction, and anisotropic thermal conductivity in pump-probe transient thermo-reflectance.* Review of Scientific Instruments, 2008. **79**(11): p. 114902.

54. Holland, M., *Analysis of lattice thermal conductivity.* Physical Review, 1963. **132**(6): p. 2461.

55. Flik, M. and C. Tien, *Size effect on the thermal conductivity of high-Tc thin-film superconductors.* Journal of heat transfer, 1990. **112**(4): p. 872-881.

56. McGaughey, A.J., et al., *Size-dependent model for thin film and nanowire thermal conductivity.* Applied Physics Letters, 2011. **99**(13): p. 131904.
57. Turney, J., A. McGaughey, and C. Amon, *In-plane phonon transport in thin films.* Journal of Applied Physics, 2010. **107**(2): p. 024317.

58. Sellan, D., et al., *Cross-plane phonon transport in thin films.* Journal of Applied Physics, 2010. **108**(11): p. 113524.

59. Maradudin, A. and A. Fein, *Scattering of neutrons by an anharmonic crystal.* Physical Review, 1962. **128**(6): p. 2589.

60. Chen, Y., et al., *Monte Carlo simulation of silicon nanowire thermal conductivity.* Journal of Heat Transfer, 2005. **127**(10): p. 1129-1137.

61. Lukes, J.R., et al., *Molecular dynamics study of solid thin-film thermal conductivity.* Journal of Heat Transfer, 2000. **122**(3): p. 536-543.

62. Sondheimer, E.H., *The mean free path of electrons in metals.* Advances in physics, 1952. **1**(1): p. 1-42.

63. Ju, Y. and K. Goodson, *Phonon scattering in silicon films with thickness of order 100 nm.* Applied Physics Letters, 1999. **74**(20): p. 3005-3007.

64. Asheghi, M., et al., *Phonon-boundary scattering in thin silicon layers.* Applied Physics Letters, 1997. **71**(13): p. 1798-1800.

65. Ju, Y.S., *Phonon heat transport in silicon nanostructures.* Applied Physics Letters, 2005. **87**(15): p. 153106.

66. Ward, J. and J. Wilks, *The velocity of second sound in liquid helium near the absolute zero.* The London, Edinburgh, and Dublin Philosophical Magazine and Journal of Science, 1951. **42**(326): p. 314-316.

67. Guyer, R. and J. Krumhansl, *Thermal conductivity, second sound, and phonon hydrodynamic phenomena in nonmetallic crystals.* Physical Review, 1966. **148**(2): p. 778.

68. Jackson, H.E., C.T. Walker, and T.F. McNelly, *Second sound in NaF.* Physical Review Letters, 1970. **25**(1): p. 26.

69. McNelly, T., et al., *Heat pulses in NaF: onset of second sound.* Physical Review Letters, 1970. **24**(3): p. 100.

70. Jackson, H.E. and C.T. Walker, *Thermal conductivity, second sound, and phonon-phonon interactions in NaF.* Physical Review B, 1971. **3**(4): p. 1428.

71. Ranninger, J., *Heat-pulse propagation in ionic lattices.* Physical Review B, 1972. **5**(8): p. 3315.

72. Beck, H. and R. Beck, *Heat-pulse propagation in dielectric solids.* Physical Review B, 1973. **8**(4): p. 1669.

73. Cahill, D.G. and R. Pohl, *Lattice vibrations and heat transport in crystals and glasses.* Annual Review of Physical Chemistry, 1988. **39**(1): p. 93-121.

74. Ma, Y., *A hybrid phonon gas model for transient ballistic-diffusive heat transport.* Journal of Heat Transfer, 2013. **135**(4): p. 044501.

75. Ma, Y., *A transient ballistic–diffusive heat conduction model for heat pulse propagation in nonmetallic crystals.* International Journal of Heat and Mass Transfer, 2013. **66**: p. 592-602.

76. Rogers, S., *Transport of heat and approach to second sound in some isotopically pure Alkali-Halide crystals.* Physical Review B, 1971. **3**(4): p. 1440.

77. Brorson, S., et al., *Femtosecond room-temperature measurement of the electron-phonon coupling constant γ in metallic superconductors.* Physical Review Letters, 1990. **64**(18): p. 2172.

78. Sun, C.-K., et al., *Femtosecond-tunable measurement of electron thermalization in gold.* Physical Review B, 1994. **50**(20): p. 15337.

79. Hohlfeld, J., et al., *Femtosecond time-resolved reflection second-harmonic generation on polycrystalline copper.* Applied Physics A, 1995. **60**(2): p. 137-142.

80. Smith, A.N. and P.M. Norris, *Influence of intraband transitions on the electron thermo-reflectance response of metals.* Applied Physics Letters, 2001. **78**(9): p. 1240-1242.

81. Hopkins, P.E., *Influence of electron-boundary scattering on thermo-reflectance calculations after intra-and interband transitions induced by short-pulsed laser absorption.* Physical Review B, 2010. **81**(3): p. 035413.

82. Qiu, T. and C. Tien, *Short-pulse laser heating on metals.* International Journal of Heat and Mass Transfer, 1992. **35**(3): p. 719-726.

83. Rustagi, K., *Bilinear optical polarizability of silver.* Il Nuovo Cimento B Series 10, 1968. **53**(2): p. 346-362.

84. Bennemann, K.-H., *Non-linear optics in metals*. 1998: Oxford University Press.

85. Anisimov, S., B. Kapeliovich, and T. Perel'Man, *Electron emission from metal surfaces exposed to ultrashort laser pulses.* Zh. Eksp. Teor. Fiz, 1974. **66**(776): p. 375-7.

86. Hohlfeld, J., et al., *Electron and lattice dynamics following optical excitation of metals.* Chemical Physics, 2000. **251**(1): p. 237-258.

87. Bennett, C.A., *Principles of physical optics*. 2008: Wiley.

88. Jha, S.S. and C.S. Warke, *Interband contributions to optical harmonic generation at a metal surface.* Physical Review, 1967. **153**(3): p. 751.

89. Olmon, R.L., et al., *Optical dielectric function of gold.* Physical Review B, 2012. **86**(23): p. 235147.

90. Bloembergen, N., R. Chang, and C. Lee, *Second-harmonic generation of light in reflection from media with inversion symmetry.* Physical Review Letters, 1966. **16**(22): p. 986.

91. Ashcroft, N.W. and N.D. Mermin, *Solid State Physics, Holt, Rinehart and Winston, New York*. 1976.

92. Nozières, P. and D. Pines, *The theory of quantum liquids*. 1999: Perseus.

93. Kittel, C. and P. McEuen, *Introduction to solid state physics*. Vol. 8. 1976: Wiley New York.

94. MacDonald, A., *Electron-phonon enhancement of electron-electron scattering in Al.* Physical Review Letters, 1980. **44**(7): p. 489.

95. Hagemann, H.-J., W. Gudat, and C. Kunz, *Optical constants from the far infrared to the x-ray region: Mg, Al, Cu, Ag, Au, Bi, C, and $A1_2O_3$.* JOSA, 1975. **65**(6): p. 742-744.

96. Kruglyak, V., *Femtosecond optical pump-probe investigations of ultrafast electron and spin dynamics in metals*. 2004, University of Exeter.

97. Kruglyak, V., et al., *Spectroscopic study of optically induced ultrafast electron dynamics in gold.* Physical Review B, 2007. **75**(3): p. 035410.

98. Guo, L. and X. Xu, *Ultrafast spectroscopy of electron-phonon coupling in gold.* Journal of Heat Transfer, 2014. **136**(12): p. 122401.

99. Freedman, J.P., et al., *Universal phonon mean free path spectra in crystalline semiconductors at high temperature.* Sci Rep, 2013. **3**: p. 2963.

100. Hopkins, P.E., et al., *Ultrafast and steady-state laser heating effects on electron relaxation and phonon coupling mechanisms in thin gold films.* Applied Physics Letters, 2013. **103**(21): p. 211910.